University of Trento
Department of Physics

Incoherent diffractive production of jets in photon-nucleus DIS at high energy

Supervisor
Dionysios Triantafyllopoulos

Doctoral Student
Benjamín Rodriguez-Aguilar

Acknowledgments

I would like to start by thanking my supervisor Dionysios for his valuable advice during my PhD. In the same way, thanks to Shu-Yi for sharing his ideas and knowledge in doing research. Thanks to ECT* and its people for giving me the chance to do science in such a particular environment. Special thanks to Tommy, for his company, friendship, hiking trips, advice, motivation, perspective, inspiration, wisdom... thank you Tommy for making my PhD *a nice and exciting experience* and mentoring my life.

Thanks to all my friends in Trento. Certainly I will forget some names, but that only means that the quality of my brain has declined. Particular and outstanding thanks to Laura, Ulysse and David for embracing me with your *real* friendship and poetic souls in the last stage of this adventure. Thanks Antoine for being so cool, I still don't understand how such a gangster got lost in Trento. Thanks for introducing me to *The core band* and its dictator Lucila, I will not name all the members of this group, but certainly we will drink a beer next Tuesday.

Thanks to the *Sanba* friends, Anna, Martina, Enrico, Mattia, Paolo, etc. ... etc., for welcoming me so kindly to the student life in Trento. Thanks to all the nice people in Povo 0, in particular to Megha and Camilla for making lunches and dinners a beautiful experience. Thanks to the *calcetto when?* fellas for organizing every week a way to relieve stress by kicking something. Thanks to all the friends in *ECT scars*, you are all winners for me, but a special thanks to Alessio for being such a good player. To close this section with a flourish, I would like to thank all the people I met just drinking in the streets, special acknowledgment to Lina and Mateo.

Gracias a mi familia por su constante apoyo y no juzgarme tan mal por las decisiones que he tomado desde hace 12 años y que me trajeron a Trento. Gracias Lulú, tus llamadas y mensajes llenan de fuerza todos mis días. Gracias Peludo por ser tan prron. Gracias Dardo por todo el apoyo y hospitalidad cuando vivías entre nosotros. Gracias Paolita por salvarme la vida. Gracias Mabel. Gracias Pamela. Gracias Lucio y Josué. Gracias Andrés por revivir y al resto de los *Preps*. Y gracias a todos los amigos en Trieste.

Напоследок хочу поблагодарить за его поддержку великого Толика. И, конечно же, это было бы неполным, если бы Я не поблагодарил мою дорогую Олесю.

Abstract

This study investigates incoherent diffractive production of two and three jets in photon-nucleus deep inelastic scattering (DIS) at small $x_{\rm Bj}$ within the color dipole picture and the Color Glass Condensate (CGC) effective field theory. By incoherent, we mean that the nuclear target breaks up due to color fluctuations in the CGC weight function, which are the source of the associated momentum transfer $\sqrt{|t|}$.

Our focus is on the regime where the two jets are nearly back-to-back in transverse space, with transverse momenta $P_\perp$ much larger than both the momentum transfer and the saturation scale Q_s. In this framework, we derive analytical expressions for the dijet cross section, which can be decomposed into four factorized terms. Each term is expressed as a product of a hard factor, which includes the virtual photon's decay into a $q\bar{q}$ pair, and a semihard factor, involving the dipole-nucleus scattering amplitude. Additionally, we compute the azimuthal anisotropies $\langle \cos 2\phi \rangle$ and $\langle \cos 4\phi \rangle$. To extend the validity of our results toward the perturbative domain, we also compute the first higher kinematic twist correction.

We demonstrate that the cross section for hard dijet production is parametrically dominated by large-size fluctuations in the projectile wave function that scatter strongly, leading to the consideration of a third, semihard jet in the final state. When this third jet is explicitly accounted for, the 2+1 jet cross section takes a factorized form involving incoherent quark and gluon diffractive transverse momentum distributions (DTMDs). Alternatively, upon integrating over the transverse momentum of the third jet, the 2+1 jet cross section is expressed in terms of incoherent diffractive parton distribution functions (DPDFs).

Our analysis shows that the DPDFs and the corresponding cross section saturate logarithmically when $|t| \ll Q_s^2$, whereas they fall off as $1/|t|^2$ in the regime $Q_s^2 \ll |t| \ll P_\perp^2$. Furthermore, in contrast to exclusive dijet production, the 2+1 jet cross section does not exhibit an angular correlation between the hard jet momentum and the momentum transfer.

Finally, we argue that for typical Electron-Ion Collider kinematics, the cross sections for 2-jet and 2+1-jet production are of the same order.

Contents

Introduction

Within the perturbative regime of Quantum Chromodynamics (QCD), the light-cone wave function (LCWF) of a hadron or nucleus at high energy is predominantly composed of gluons, whose occupation numbers grow rapidly as their longitudinal momentum fraction x decreases [1–4]. To preserve unitarity in physical observables, it is necessary to account for gluon recombination, which regulates the growth of these highly occupied modes and introduces non-linear dynamics [5, 6]. This phenomenon is known as gluon saturation and a dynamical scale, called *saturation momentum* Q_s, emerges to separate the dilute regime (where gluons have transverse momenta $k_\perp \gg Q_s$) from the dense one (where $k_\perp \ll Q_s$). To a good approximation, the scale grows as $Q_s^2(A,x) \propto \Lambda^2 A^{1/3}(1/x)^\lambda$, where Λ is the QCD scale, A represents the atomic number of the nucleus and $\lambda \simeq 0.25$, [7, 8]. This behavior provides a clear justification for employing weak coupling methods in the regime of sufficiently large nuclei and/or small values of x.

The Color Glass Condensate (CGC) [9, 10] is a modern effective field theory within QCD that incorporates the phenomenon of gluon saturation. It is formulated by calculating soft gluon emissions in the presence of a strong background color field, leading to non-linear evolution equations for amplitude correlators at small x [11–19]. These equations encode the determination of cross sections and other relevant physical observables.

The investigation of saturation phenomena typically focuses on high-energy collisions of the system of interest with smaller projectiles. These collisions include proton-nucleus (pA) interactions, Deep Inelastic Scattering (DIS) of electrons off hadrons (such as ep) or nuclei (eA), and ultra-peripheral nucleus-nucleus collisions (UPCs), where a quasi-real photon emitted by one nucleus probes the other. In recent years, there has been considerable interest in events where the kinematics of one or more final-state particles are precisely measured. The simplest example of such processes is single inclusive DIS [20–24]. One of the most extensively studied processes is the inclusive production of two jets in the forward direction of the projectile [25–40]. In ep and eA collisions, these jets originate from the $q\bar{q}$ pair fluctuation of the virtual photon, whereas in pA collisions, they typically result from a quark-gluon pair produced via the splitting of a collinear quark. A common focus is on the kinematic limit (the so-called *correlation limit*) where the two jets are hard and nearly back-to-back in the transverse plane, i.e. the transverse momenta of the jets are much harder than both the saturation momentum and the imbalance between them. In this regime, the dijet momentum imbalance is of the order of the momentum transferred from the target to the projectile, making it sensitive to saturation physics. Similar considerations apply to dihadron production [41–46], as the perturbative part of the process remains the same. These ideas have also been employed to study the nearly back-to-back production of a photon-jet system, generated via the $g \to q\bar{q}\gamma$ fluctuation, in pA collisions [47].

Equally important is the diffractive production of jets or hadrons, since this kind of processes is controlled by the saturation regime [34, 48–60]. A defining characteristic of diffractive processes is the presence of a region in rapidity that is void of particles, known as a *rapidity gap*. Specifically, in QCD one considers the scenario in which the rapidity gap arises because the projectile remains colorless after the interaction, forming the *diffractive system*. In this case, the collision is elastic on the projectile side, and no new particles are produced in the rapidity interval separating the target and the projectile. Regarding the hadronic target, it may remain intact or break apart after the collision and we refer to these processes as coherent diffraction and incoherent diffraction, respectively.

In the CGC framework, a coherent process implies that, when calculating the respective cross section, the average over the target field can be performed at the amplitude level. Then, an incoherent diffractive process can be defined as the complementary part of the coherent one with respect to the total diffraction. The subtraction of the coherent correlator from the total one suggests that incoherent diffraction is driven by fluctuations in the target weight function. This work is focused on the case of color fluctuations arising from the color exchange between substructures within a nucleus [34, 61–64]. In other words, in an incoherent process, we assume that the nucleus fragments due to internal color fluctuations, which are responsible for the associated momentum transfer.

The primary goal of this work is to rely on the expertise gained in the coherent diffractive production of two and three jets in high-energy photon-nucleus collisions [52, 55, 56, 60], with the aim of exploring the effects of color fluctuations in the corresponding incoherent process. The production of dijets was first studied in [34] for generic transverse momenta of the jets, requiring the approach to be mainly numerical. Therefore, our first scope was to provide an analytical insight in the correlation limit [63]. Then, we proceeded to consider the case in which the hard dijet is accompanied by a third semi-hard jet [64].

To present the results of our study, we have structured this thesis as follows. In Chapter 1 we give a general introduction to perturbative QCD, with a special focus on the high energy limit in DIS. In Chapter 2 we provide the general overview of small-x physics relevant to our purposes. We start with a brief review of the eikonal approximation and Wilson lines in QCD, which is followed by a discussion of the CGC effective field theory. This finally lead us to the scattering matrix model and evolution equations that allow us to perform analytical and numerical analysis in our study. In Chapter 3 we give a discussion on coherent and incoherent diffraction in the dipole picture, providing a diagramatic argumentation on the incoherent diffractive correlator in the Gaussian approximation.

Having the introductory part at hand, in Chapter 4 we provide the derivation and analysis of the $q\bar{q}$ contribution to the incoherent diffractive dijet cross section. In particular, we start by reviewing the calculation of the cross sections and in Sec. 4.3, within the correlation limit, we provide them in a factorized way, i.e. separating the hard momentum dependence from the semi-hard one. In Sec. 4.4 we extensively analyze the semi-hard momentum dependence of the cross sections, to then perform a complete analysis of the averaged-over-angle cross sections in Sec. 4.5. We conclude this chapter by analyzing the azimuthal anisotropies in Sec. 4.6.

In Chapter 5 we continue our study by considering the $q\bar{q}g$ contribution to the cross section of interest. We take into account the cases when either a (anti)quark or a gluon are the source of the semi-hard jet. Then, in Chapter 6 we show how the incoherent diffractive transverse momentum distributions (DTMDs) emerge. We rewrite the cross sections of interest in a TMD factorized form and further analyze the properties of the quark and gluon DTMDs, together with the diffractive parton distribution functions (DPDFs) that, in the case of the $2+1$ jets, arise when the semi-hard jet transverse momentum is integrated over. In Chapter 7 we make a direct comparison of the 2 jets and $2+1$ jets contributions by introducing an appropriate observable, namely dijet production with a minimum rapidity gap. Then, we present the conclusions of the study.

We also provide some technical calculations and helpful reviews in the appendices. In particular, in Appendix A we show some particularly useful integrals. In Appendix B we show the tensor decompositions and contractions employed to get the dijet cross section. In Appendix C we show a review of the inclusive dijet cross section with the proper notation in order to be compared to the incoherent diffractive one. Appendix D gives some details of the tensorial structures at next to leading "kinematic" twist in the $q\bar{q}$ contribution. In Appendix E it is shown that, in the $q\bar{q}g$ contribution, the gluon semi-hard factor is diagonal. Finally, in Appendix F it is given in full detail the study of the gluon DPDF in the limiting regimes.

Chapter 1

Quantum Chromodynamics

Quantum Chromodynamics (QCD) is a non-Abelian gauge theory designed to describe strong interactions. It specifically refers to the fundamental interactions between quarks and gluons, as well as the bound states they form, such as hadrons and nuclei [65–68]. The QCD Lagrangian is invariant under local $SU(N_\mathrm{c})$ gauge transformations, and its density in natural units is given by

$$\mathcal{L}_\mathrm{QCD} = \sum_f \bar{\psi}^f_\alpha \left(i\gamma^\mu D_\mu - m_f\right)_{\alpha\beta} \psi^f_\beta - \frac{1}{4} F^a_{\mu\nu} F^{\mu\nu}_a, \tag{1.1}$$

where ψ^f_β and $\bar{\psi}^f_\alpha$ represent the quark and antiquark Dirac fields with spin 1/2, flavor f, and mass m_f, for the six quark flavors in the Standard Model. The color indices α, β on the fields in the fundamental representation of the $SU(N_\mathrm{c})$ gauge group take the values $\alpha, \beta = 1 \dots N_\mathrm{c}$, and γ^μ are the gamma matrices. The covariant derivative can be defined as

$$D_\mu = \partial_\mu - ig\, t^a A^a_\mu, \tag{1.2}$$

where A^a_μ represent the gluon field, belonging to the adjoint representation of $SU(N_\mathrm{c})$, with spin 1 and color $a = 1 \dots N_\mathrm{c}^2 - 1$. The matrices t^a are the generators of $SU(N_\mathrm{c})$ in the fundamental representation and g is the coupling of the theory. The gauge field strength tensor $F^a_{\mu\nu}$ can be defined in terms of the covariant derivative,

$$g\, t^a F^a_{\mu\nu} = i[D_\mu, D_\nu], \tag{1.3}$$

or explicitly in terms of the gluon field,

$$F^a_{\mu\nu} = \partial_\mu A^a_\nu - \partial_\nu A^a_\mu + g\, f^{abc} A^b_\mu A^c_\nu. \tag{1.4}$$

The coefficients f^{abc}, known as the *structure constants* of the group $SU(N_\mathrm{c})$, appear in the commutation relations of the generators of the Lie algebra. In fact, the commutation relations of the generators t^a follow the relation

$$[t^a, t^b] = i f^{abc} t^c \tag{1.5}$$

and by convention, the basis of the matrices t^a are chosen such that f^{abc} is always antisymmetric. In QCD, the number of colors is $N_\mathrm{c} = 3$, and the generators in the fundamental representation can be expressed in terms of the Gell-Mann matrices, which form a basis for the $SU(3)$ Lie algebra.

The third term in the r.h.s. of Eq. (1.4) implies the self interaction of the gluon field, a property of non-Abelian gauge theories. Another important feature of the QCD Lagrangian Eq. (1.1) is that it is renormalizable. As a consequence, the coupling g depends on the arbitrary (renormalization) scale of the theory. Physical observables should not depend explicitly on the renormalization scale. This is ensured by renormalization group invariance, which requires that the scale dependence of parameters, i.e. of the coupling and the masses, cancels out in physical quantities. In particular, the scale dependence of the coupling is encoded in the QCD beta function, which at one loop in perturbation theory reads

$$\beta_{\mathrm{QCD}}(\alpha_s) = -b\ \alpha_s^2 + \mathcal{O}(\alpha_s^3), \tag{1.6}$$

where the *strong coupling* is defined as $\alpha_s = g^2/4\pi$ and

$$b = \frac{1}{4\pi}\left(\frac{11}{3}N_{\mathrm{c}} - \frac{2}{3}n_f\right). \tag{1.7}$$

Then, for a physical scale k, the strong coupling can be written as

$$\alpha_s(k^2) = \frac{1}{b\ \ln\left(k^2/\Lambda^2\right)}, \tag{1.8}$$

where Λ is known as the QCD scale or Λ_{QCD}, its value depends on the renormalization scale scheme used, however generally is taken as $\Lambda \simeq 0.1 - 0.3$ GeV.

In this work, our attention relies on the physical processes governed by large momentum scales, $k \gg \Lambda$, which imply small values of α_s. This means that, at short distances inside hadrons and/or nuclei, the elementary constituent quarks and gluons — commonly referred to as *partons* — interact weakly and can be treated as free particles, a property known as *asymptotic freedom*. Moreover, small values of the strong coupling justify the use of perturbative techniques in QCD, i.e. of perturbative QCD (pQCD).

1.1 Deep Inelastic Scattering

We are interested in the high-energy behavior of QCD. In this framework, one of the simplest and most powerful processes for studying the structure of hadrons is the so-called *deep inelastic scattering* (DIS). In general, this process involves the reaction

$$e(p) + H(P) \to e'(p') + X, \tag{1.9}$$

in which an incoming lepton, represented by an electron e with momentum p, scatters off a hadronic target H (which can be a hadron or a nucleus) carrying a momentum P. The final state consists of an outgoing electron e' with momentum p' and the produced particles, denoted by X. Considering the *virtuality* variable $Q^2 \equiv -q^2 = -(p-p')$, when $Q \ll M_Z$, with M_Z being the mass of the Z boson, the DIS process can only be mediated by a virtual photon, commonly denoted as γ^*, which carries a momentum q. This condition will hold in the rest of this work, and such a process is shown diagrammatically in Fig. 1.1. We shall work in frames where the virtual photon and the hadronic target are both ultra-relativistic. In this framework, it is convenient to work with the light-cone notation. In this notation, any four-vector v^μ possesses longitudinal *plus* and *minus* components given by

$$v^+ = \frac{v^0 + v^3}{\sqrt{2}}, \quad v^- = \frac{v^0 - v^3}{\sqrt{2}} \tag{1.10}$$

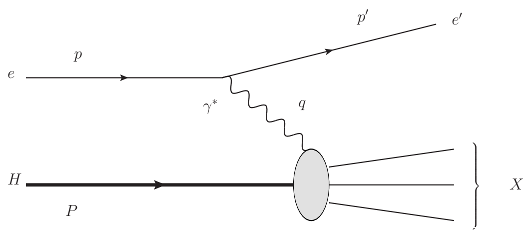

Figure 1.1: Deep inelastic electron-hadron scattering.

and transverse components encoded in the 2-dimensional vector $\boldsymbol{v} \equiv v^i$ where $i = 1, 2$. The non-zero components of the metric are $g_{+-} = g_{-+} = 1$ and $g_{11} = g_{22} = -1$, and any four-vector is usually written in the $(+, -, \perp)$ notation. Considering a particle of mass m, four-momentum k^μ, and coordinate variables x^μ, the x^+ component plays the role of time, while its conjugate variable in momentum space, the light-cone energy k^-, satisfies the on-shell condition

$$k^- = \frac{\boldsymbol{k}^2 + m}{2k^+}. \tag{1.11}$$

During this work we will denote the magnitude of any transverse vector in momentum space as $k_\perp \equiv |\boldsymbol{k}|$. For transverse vectors in coordinate space, their magnitude will be denoted by dropping the bold format, i.e. considering the transverse position $\boldsymbol{x}$, its magnitude is given by $x \equiv |\boldsymbol{x}|$.

1.1.1 Kinematics in photon-nucleus DIS

For definiteness, we will consider the target to be a nucleus with atomic number $A \gg 1$, although most of the following analysis is also valid for smaller nuclei and hadrons. Considering the momentum of the target per nucleon, $P_N \equiv P/A$, and ignoring the electron that emits the virtual photon, we generally work with the invariants to describe the kinematics of photon-nucleus DIS ($\gamma^* A$):

$$\begin{aligned} s &= (P_N + q)^2, \\ Q^2 &\equiv -q^2, \\ x_{\text{Bj}} &\equiv \frac{Q^2}{2P_N \cdot q}, \end{aligned} \tag{1.12}$$

where s denotes the center-of-mass energy squared of the photon-nucleon scattering, Q^2 is the aforementioned virtuality of the photon, and x_{Bj} is the Bjorken-x variable.

The physical interpretation of x_{Bj} is that it represents the fraction of the nucleon momentum in the nucleus carried by the parton involved in the scattering process, implying that $x_{\text{Bj}} \leq 1$.

Setting the virtual photon as a right mover, its momentum in light-cone notation can be chosen to be:

$$q^\mu = \left(q^+, \frac{-Q^2}{2q^+}, \mathbf{0}\right). \tag{1.13}$$

Hence, the light-cone time of the virtual photon, x^+ (also known as its *coherence length*), is of the order of $2q^+/Q^2$. In the rest frame of the nucleus with mass m per nucleon, using the definition of x_{Bj}, we see that

$$x^+ \simeq \frac{1}{m x_{\text{Bj}}}, \tag{1.14}$$

so x_{Bj} sets the time scale for the DIS process. The relation in Eq. (1.14) is known as the *Ioffe time* [69–72]. On the other hand, the typical interpretation of the virtuality Q^2 in DIS is that it controls the "resolution" of the process. In other words, by varying Q^2, the virtual photon is constrained to interact with the partonic content of the nucleus at different transverse scales.

By setting the nucleus to be an ultra-relativistic left mover (neglecting the mass of the nucleons), its momentum is given by

$$P_N^\mu = \left(0, P_N^-, \mathbf{0}\right). \tag{1.15}$$

Considering R_N as the nucleon radius, the longitudinal length of a boosted nucleus is $L = R_A/\gamma$, where $R_A = A^{1/3} R_N$ and $\gamma \simeq P_N^- R_N$ is the Lorentz factor. Hence, the regime of small values of x_{Bj}, i.e. $x_{\text{Bj}} \lesssim 10^{-2}$, immediately implies that the coherence length of the photon, x^+, is much larger than the longitudinal length of the nucleus, L.

This means that when considering a virtual photon at sufficiently high energies, it is convenient to adopt the *dipole picture*, in which the virtual photon γ^* fluctuates into a quark-antiquark pair $q\bar{q}$, and the resulting system[1] interacts via gluon exchanges with the components of the nuclear target [73–76]. On the other hand, when considering ultra-relativistic energies for the nuclear target, we are in the regime of small values of x_{Bj}, in which the nucleus generates a strong color field. As a result, multiple scattering and the high-energy evolution of the process must be taken into account [77].

In fact, the multiple scattering process is given by resumming powers of $\alpha_s^2 A^{1/3}$ for large values of A [78], and the high-energy evolution describes the physics from moderate small values of $x_{\text{Bj}} \sim 10^{-2}$ to even smaller values. This phenomenon can be addressed in the context of *gluon saturation* or *saturation physics*, and its study is the goal of the Color Glass Condensate (CGC) effective field theory, which is discussed in the next chapter. Before introducing the CGC, we briefly discuss the concept of the high-energy limit in QCD.

1.2 The high energy limit

As mentioned previously, we focus on the regime where $x_{\text{Bj}} \ll 1$. To be more precise, in the context of DIS we work for fixed values of the virtuality Q^2, while we take the photon-nucleus center-of-mass energy s to be large. By simple inspection of the relations in Eq. (1.12), we see that

$$x_{\text{Bj}} \simeq \frac{Q^2}{s}, \tag{1.16}$$

from which it is clear that the high energy limit of QCD is equivalent to asymptotically small values of x_{Bj}. This is why the high energy behavior of QCD is commonly referred to as *small-x* physics. In this framework, we will drop the subscript of the Bjorken-x variable and will only use it explicitly to avoid confusion with other similar variables.

To study the high energy evolution of QCD, we are interested in resumming powers of the parameter $\alpha_s \ln 1/x$, which can be of the order of one, since $\ln 1/x \gg 1$ and can overcome the smallness of α_s. This is known as the leading logarithmic approximation (LLA) in $1/x$.

[1] As we will see in the following chapters, we will also consider the contribution of the subsequent gluon emission.

The generalization of this resummation, including the multiple scattering approach in general hadronic processes at high energy, will be discussed in the next chapter. The most dominant corrections beyond the LLA can be effectively resummed by using suitable evolution equations consistent with renormalization group constraints [79–81].

A similar analysis can be done by fixing x and taking the asymptotic high values of Q^2 by resumming the parameter $\alpha_s \ln Q^2/Q_0^2 \sim 1$, with Q_0^2 being an initial momentum scale. Such an evolution is described by the Dokshitzer–Gribov–Lipatov–Altarelli–Parisi (DGLAP) evolution equations [82–84].

It is worth mentioning that, before the emergence of QCD, the study of the analyticity and the asymptotic behavior of the scattering matrix (S-matrix) in hadronic processes was the focus of *Regge theory* [85, 86]. This theory is based on the postulates of Lorentz invariance and the unitarity of the S-matrix, and it is able to describe hadronic cross sections in the high energy regime, also known as the *Regge limit*, where $s \to \infty$ while the transferred momentum is fixed (Q^2 in electron-nucleus DIS). Although the primary focus of the study of strong interactions has shifted to QCD due to its ability to describe a broad range of phenomena, the progress and understanding achieved by Regge theory are still valued (see e.g., [87] for a pedagogical introduction and [88] for details). Similarly, a considerable amount of the terminology used in this *old-fashioned* theory is still embedded in the current studies of QCD.

Chapter 2

Color Glass Condesate

Before considering the ideas of the CGC, it is customary to introduce the concept of the *eikonal* approximation in small-x physics. This will lead us to the idea of Wilson lines as the appropriate degrees of freedom to describe high-energy scattering and the shockwave formalism. It will also help us introduce the notation used in the following chapters. The next section follows the derivations and analysis in [89–91], with the notation adapted to our purposes. The sub-eikonal contributions are beyond the scope of this work.

2.1 Eikonal scattering and Wilson lines

The scattering between a particle system off an external field is encoded in the generic S-matrix element, which describes the transition between arbitrary initial and final states, α and β, and is defined as

$$S_{\alpha\beta} \equiv \langle \beta_{\text{out}} | \alpha_{\text{in}} \rangle = \langle \beta_{\text{in}} | U(+\infty, -\infty) | \alpha_{\text{in}} \rangle. \tag{2.1}$$

In our analysis, the states α and β are, in principle, composed of quarks, antiquarks, and gluons. The evolution operator $U(+\infty, -\infty)$, which evolves the initial (incoming) state at $-\infty$ to the final (outgoing) state at $+\infty$, can be expressed as

$$U(+\infty, -\infty) = T^+ \exp\left\{ i \int \mathrm{d}^4 x \mathcal{L}_I(\psi_{int}) \right\}, \tag{2.2}$$

where T^+ denotes an ordering in the light-cone time x^+, ψ_{int} represents the fields in the interaction picture, and the Lagrangian $\mathcal{L}_I$ contains the self-interactions of the fields as well as their interactions with an external field.

To consider the high-energy limit of the scattering amplitude, we shall apply a boost of *rapidity*[1] Y in the $+z$ direction to the particles in the states α and β, namely,

$$S_{\alpha\beta} = \langle \beta_{\text{in}} | e^{+iYK_3} U(+\infty, -\infty) e^{-iYK_3} | \alpha_{\text{in}} \rangle, \tag{2.3}$$

where K_3 is the generator of longitudinal boosts. The operator between the initial states can also be written as

$$e^{+iYK_3} U(+\infty, -\infty) e^{-iYK_3} = T^+ \exp\left\{ i \int \mathrm{d}^4 x \; e^{+iYK_3} \mathcal{L}_I(\psi_{int}) e^{-iYK_3} \right\} \tag{2.4}$$

[1] Such a quantity will be properly defined in terms of kinematic variables in the following sections. In this context, it suffices to take it as the *boosting* variable in the high-energy limit.

since the boost does not affect the time ordering. We are interested in the high-energy limit, i.e., $Y \to \infty$. In this kinematic region, as the energy of the incoming state increases, the interaction time of the projectile with the external field tends to zero. To ensure a non-zero and non-infinite scattering amplitude, it is necessary to assume that the interaction between the projectile and the external field is mediated by a vector exchange. Specifically, the vector current of the projectile, J^μ, couples to the external vector potential, $\mathcal{A}_\mu$, via a term $gJ^\mu\mathcal{A}_\mu$, where g is the coupling constant of the theory. This is due to the fact that, at high energies, the vector current J^μ has a longitudinal component that increases in proportion to the energy, compensating for the suppression due to the infinitesimal interaction time. This assumption is indeed satisfied by the interactions of color fields in QCD, and it was originally developed in the context of photon exchange in QED [92]. In other words, the integrand in the exponent in Eq. (2.2) can be rewritten as

$$\mathcal{L}_I(\psi_{int}) = gJ^\mu\mathcal{A}_\mu. \tag{2.5}$$

K_3 only affects the vector current, since the external field is not altered by the longitudinal boost of the projectile. Moreover, under longitudinal boosts, the $\pm$ components of a generic vector receive a rescaling factor of $e^{\pm Y}$, while the transverse component remains unchanged. Therefore, at large rapidities, the product $J^\mu\mathcal{A}_\mu$ is dominated by the contribution from $J^+\mathcal{A}^-$. In practice, it is also convenient to assume that the external field is confined to a finite range, $x^+ \in (-L, L)$. This implies that the evolution operator can be decomposed as follows:

$$U(+\infty, -\infty) = U(+\infty, +L)U(+L, -L)U(-L, -\infty). \tag{2.6}$$

The lateral factors $U(+\infty, +L)$ and $U(-L, -\infty)$ do not contain the external field, and under the boost, the change of variables $e^{\mp Y}x^\pm \to x^\pm$ leads to

$$\begin{aligned} e^{+iYK_3}U(+\infty, +L)e^{-iYK_3} &= U_0(+\infty, 0), \\ e^{+iYK_3}U(-L, -\infty)e^{-iYK_3} &= U_0(0, -\infty), \end{aligned} \tag{2.7}$$

where U_0 in the r.h.s. denotes that the evolution operator only contains self-interactions. The central factor in Eq. (2.6) is the one containing the interaction with the external field and under the boost can be written as,

$$e^{+iYK_3}U(+L, -L)e^{-iYK_3} \simeq T^+ \exp\left\{ig \int \mathrm{d}^4x \; e^{+Y} J^+(e^{-Y}x^+, e^{+Y}x^-, \boldsymbol{x})\mathcal{A}^-(x^+, x^-, \boldsymbol{x})\right\}. \tag{2.8}$$

Applying the change of variables $e^{-Y}x^- \to x^-$ and considering the large rapidity limit, we get

$$e^{+iYK_3}U(+L, -L)e^{-iYK_3} = T^+ \exp\left\{ig \int \mathrm{d}^2\boldsymbol{x} \; \chi(\boldsymbol{x})\rho(\boldsymbol{x})\right\}, \tag{2.9}$$

where we have defined the functions dependent on the transverse variables

$$\chi(\boldsymbol{x}) \equiv \int \mathrm{d}x^+ \mathcal{A}^-(x^+, 0, \boldsymbol{x}) \quad \text{and} \quad \rho(\boldsymbol{x}) \equiv \int \mathrm{d}x^- J^+(0, x^-, \boldsymbol{x}). \tag{2.10}$$

Therefore, the S-matrix in the high energy limit can be written as

$$S_{\alpha\beta} = \langle\beta_{\text{in}}|U_0(+\infty, 0) \; T^+ \exp\left\{ig \int \mathrm{d}^2\boldsymbol{x} \; \chi(\boldsymbol{x})\rho(\boldsymbol{x})\right\} \; U_0(0, -\infty)|\alpha_{\text{in}}\rangle. \tag{2.11}$$

This non-perturbative result at high energies is known as the *eikonal limit*. By inserting the identity matrix expanded as a sum of complete sets in each side of the central factor in Eq. (2.11),

$$S_{\alpha\beta} = \sum_{\gamma,\delta} \langle \beta_{\rm in}|U_0(+\infty,0)|\gamma_{\rm in}\rangle\langle\gamma_{\rm in}|T^+ \exp\left\{ig\int {\rm d}^2\boldsymbol{x}\ \chi(\boldsymbol{x})\rho(\boldsymbol{x})\right\}|\delta_{\rm in}\rangle\langle\delta_{\rm in}|\ U_0(0,-\infty)|\alpha_{\rm in}\rangle, \tag{2.12}$$

we see that the Fock expansions, $\sum_\delta |\delta_{\rm in}\rangle\langle\delta_{\rm in}|\ U_0(0,-\infty)|\alpha_{\rm in}\rangle$ and $\sum_\gamma\langle\beta_{\rm in}|U_0(+\infty,0)|\gamma_{\rm in}\rangle\langle\gamma_{\rm in}|$, represent the possibility of fluctuations of the state α and β into states δ and γ before and after the interaction with the external potential respectively.

2.1.1 Wilson lines in QCD

The color current J_a^ν associated to the QCD Lagrangian Eq. (1.1) in a generic frame is given by

$$J_a^\nu = \bar\psi_\alpha\gamma^\mu(t^a)_{\alpha\beta}\psi_\beta + f^{abc}F_b^{\mu\nu}A_\nu^c, \tag{2.13}$$

where we have dropped the flavor index. In the present analysis, we emphasize that the vector field A represents the gluons in the system interacting with the external field $\mathcal{A}$. In light-cone coordinates in the light-cone gauge $A^+=0$, the $+$ component of the current, takes the form

$$J_a^+ = \sqrt{2}\psi^\dagger_{\alpha+}(t^a)_{\alpha\beta}\psi_{\beta+} - f^{abc}\partial^+A^i_{\perp b}A^i_{\perp c}, \tag{2.14}$$

where in the spinors we have used the notation $\psi_+ \equiv \frac{\gamma^0\gamma^+}{\sqrt{2}}\psi$. Then, by performing the mode expansion of the fields in J_a^+ and integrating over the x^- at $x^+=0$, we arrive to the QCD expression of the $\rho(\boldsymbol{x})$ function in Eq. (2.10),

$$\begin{aligned}\rho_a(\boldsymbol{x}) = \frac{1}{2\pi}\int\frac{d^2\boldsymbol{p}}{(2\pi)^2}\frac{d^2\boldsymbol{p}'}{(2\pi)^2}\int_0^{+\infty}\frac{dp^+}{2p^+}e^{-i(\boldsymbol{p}-\boldsymbol{p}')\cdot\boldsymbol{x}}\\ \times\Bigg\{\sum_{\sigma;\alpha\beta}(t^a)_{\alpha\beta}\left[b_\alpha^{(\sigma)\dagger}(p^+,\boldsymbol{p})b_\beta^{(\sigma)}(p^+,\boldsymbol{p}') - d_\beta^{(\sigma)\dagger}(p^+,\boldsymbol{p})d_\alpha^{(\sigma)}(p^+,\boldsymbol{p}')\right]\\ +\sum_{\lambda;bc}(-if^{abc})a_b^{(\lambda)\dagger}(p^+,\boldsymbol{p})a_c^{(\lambda)}(p^+,\boldsymbol{p}')\Bigg\},\end{aligned} \tag{2.15}$$

where $\sigma=\pm1/2$ and $\lambda=\pm1$ represent the helicities of the quark/antiquark and gluon, respectively. From Eq. (2.15), it is clear that when $\rho_a(\boldsymbol{x})$ is applied to a state consisting of quarks, antiquarks, and gluons, the ladder operators annihilate and recreate them with the same longitudinal momentum p^+, helicity, and flavor. Furthermore, the operator can affect the color and transverse momenta. On the other hand, the phase in $\rho_a(\boldsymbol{x})$ shows that the transverse position $\boldsymbol{x}$ of the partonic states is not altered by $\rho_a(\boldsymbol{x})$, indicating that it is convenient to work with states in the *mixed representation* of $+$ momenta and transverse coordinates when considering high-energy processes.

A bare quark state in the mixed representation can be written as the Fourier transform of the quark state in the momentum representation,

$$|q_\sigma^\alpha(k^+,\boldsymbol{x})\rangle = \int\frac{{\rm d}^2\boldsymbol{k}}{2\pi}e^{-i\boldsymbol{k}\cdot\boldsymbol{x}}|q_\sigma^\alpha(k^+,\boldsymbol{k})\rangle \tag{2.16}$$

Similarly, for an antiquark we use the label $\bar{q}$ instead of q in Eq. (2.16), while a bare gluon state is represented with the label $|g\rangle$ and colour index in the adjoint representation, i.e.

$$|g^a_\lambda(k^+, \boldsymbol{x})\rangle = \int \frac{\mathrm{d}^2\boldsymbol{k}}{2\pi} e^{-i\boldsymbol{k}\cdot\boldsymbol{x}} |g^a_\lambda(k^+, \boldsymbol{k})\rangle. \tag{2.17}$$

Applying the $\rho_a(\boldsymbol{y})$ operator to the quark state we get

$$\rho(\boldsymbol{y})|q^\alpha_\sigma(k^+, \boldsymbol{x})\rangle = \delta^{(2)}(\boldsymbol{y}-\boldsymbol{x})|q^\alpha_\sigma(k^+, \boldsymbol{x})\rangle t^a. \tag{2.18}$$

We immediately see that $\rho_a(\boldsymbol{y})$ acts in an antiquark state in an analogous way with $t^a \to (-t^a)$, while applied to a gluon state we have

$$\rho(\boldsymbol{y})|g^a_\lambda(k^+, \boldsymbol{x})\rangle = \delta^{(2)}(\boldsymbol{y}-\boldsymbol{x})|g^a_\lambda(k^+, \boldsymbol{x})\rangle T^a, \tag{2.19}$$

where T^a are the generators in the adjoint representation Hence, the central factor in Eq. (2.12) acts on a quark and gluon state as,

$$T^+ \exp\left\{ig \int \mathrm{d}^2\boldsymbol{x}\ \chi(\boldsymbol{x})\rho(\boldsymbol{x})\right\}|q^\alpha_\sigma(k^+, \boldsymbol{x})\rangle = V(\boldsymbol{x})|q^\alpha_\sigma(k^+, \boldsymbol{x}), \tag{2.20}$$

$$T^+ \exp\left\{ig \int \mathrm{d}^2\boldsymbol{x}\ \chi(\boldsymbol{x})\rho(\boldsymbol{x})\right\}|g^a_\lambda(k^+, \boldsymbol{x})\rangle\rangle = U(\boldsymbol{x})|g^a_\lambda(k^+, \boldsymbol{x})\rangle, \tag{2.21}$$

where $V(\boldsymbol{x})$ and $U(\boldsymbol{x})$ are known as the fundamental and adjoint *Wilson lines* and are defined as

$$V(\boldsymbol{x}) = T^+ \exp\left\{igt^a \int \mathrm{d}x^+ \mathcal{A}^-_a(x^+, 0, \boldsymbol{x})\right\}, \tag{2.22}$$

$$U(\boldsymbol{x}) = T^+ \exp\left\{igT^a \int \mathrm{d}x^+ \mathcal{A}^-_a(x^+, 0, \boldsymbol{x})\right\}. \tag{2.23}$$

In fact, in the eikonal limit, the multiple scattering of an incoming state with an external potential $\mathcal{A}$ is encoded by the respective Wilson lines. In the case of an incoming antiquark state, the scattering is encoded by the complex conjugated fundamental Wilson line, $V^\dagger(\boldsymbol{x})$.

Defining the light-cone wave functions in the mixed representation of the incoming state, the right factor in Eq. (2.12) is given by

$$\Psi_{\delta\alpha}(k^+_i, \boldsymbol{x}_i) \equiv \prod_{i\in\delta} \int \frac{\mathrm{d}^2\boldsymbol{k}_i}{2\pi} e^{-i\boldsymbol{k}_i\cdot\boldsymbol{x}_i} \langle\delta_{\mathrm{in}}|\ U_0(0,-\infty)|\alpha_{\mathrm{in}}\rangle, \tag{2.24}$$

the S-matrix element at high energy limit can be written as

$$S_{\beta\alpha} = \sum_\delta \int \prod_{i\in\delta} \frac{\mathrm{d}k^+_i}{4\pi k^+_i} \mathrm{d}^2\boldsymbol{x}_i \Psi^\dagger_{\delta\beta}(\{k^+_i, \boldsymbol{x}_i\}) \left[\prod_{i\in\delta} W_i(\boldsymbol{x}_i)\right] \Psi_{\delta\alpha}(\{k^+_i, \boldsymbol{x}_i\}), \tag{2.25}$$

where W denotes the Wilson lines describing the scattering. This means that, in practice, the high-energy scattering amplitude in the eikonal limit for a projectile state interacting with an external potential can be represented by the convolution of the projectile wave function and the Wilson lines, which represent the infinitesimal short-time interaction with the target. This is known as the *shockwave* approach.

2.2 Color Glass Condensate

In the previous section, the energy dependence was obtained by applying a boost to the dipole projectile. Here, instead, because the transition amplitudes are Lorentz invariant, we will work in the frame where the boost is applied to the hadronic target. In this frame, the energy dependence of the scattering amplitude is given by the x dependence of the target gluon distribution.

Thus, when considering hadrons and nuclei at high energies, their partonic content is allowed to split into partons with smaller momentum fractions. The parton distributions are dominated by small-x gluons, and their growth is described by linear equations [1–3]. However, an unbounded growth in the high-energy limit is unphysical, since the scattering amplitude should not exceed unity. In fact, the gluon density in phase space favors the recombination of gluons, leading to the fulfillment of unitarity limits [5, 6]. This phenomenon is known as gluon saturation, and the CGC is a modern effective field theory focused on its study [9, 10, 89, 93].

The idea of the CGC effective field theory relies on the separation of degrees of freedom in an ultrarelativistic hadronic target, specifically, a division between large-x (fast) partons and small-x (slow) partons. Since this separation is arbitrary, a renormalization group equation is required to ensure the independence of physical quantities from the cutoff used as the separation scale. The fast partons do not undergo significant time evolution during the short duration of the collision due to time dilation, so they can be treated as classical static sources for the smaller-x partons. On the other hand, the slow partons must be described by the QCD gauge field. Consequently, the classical Yang-Mills equation must be solved,

$$D_\mu F_a^{\mu\nu} = J_a^\nu, \tag{2.26}$$

where J^ν is the current provided by the color sources in the target, so that moving at ultrarelativistic energies in the $-$ direction reads

$$J_a^\nu = \delta^{\nu +}\rho_a(x^-, \boldsymbol{x}). \tag{2.27}$$

The ρ function is the corresponding color charge density, and it is a stochastic quantity that varies with each collision. The CGC description provides a gauge-invariant distribution (weight functional) $W_Y[\rho]$ that encodes the probability of any ρ configuration for a given rapidity Y, which is, in fact, the convenient scale that separates the fast and slow degrees of freedom. In this framework, every observable must be averaged over all possible configurations of ρ; that is, the scattering process must be averaged over all target configurations. The expectation value of a given density-dependent operator $\hat{\mathcal{O}}_\rho$ for a scale Y is given by

$$\langle \hat{\mathcal{O}} \rangle_\rho = \int \mathcal{D}\rho \, \hat{\mathcal{O}}_\rho W_Y[\rho], \tag{2.28}$$

where the normalization of the distribution $W_Y[\rho]$ is such that $\int \mathcal{D}\rho W_Y[\rho] = 1$. As mentioned earlier, the observables must not depend on a particular cutoff in rapidity; thus, the distribution $W_Y[\rho]$ must evolve according to the functional evolution equation, known as the Jalilian-Marian-Iancu-McLerran-Weigert-Leonidov-Kovner (JIMWLK) equation [13–19], which reads

$$\frac{\partial W_Y[\rho]}{\partial Y} = \mathcal{H}[\rho] W_Y[\rho], \tag{2.29}$$

where $\mathcal{H}$ is known as the JIMWLK Hamiltonian. Such an evolution equation requires an initial condition that must be non-perturbative at the starting scale. However, in the perturbative regime, one can choose the evolution to start at a certain cutoff value Y_0 such that the saturation scale is already semi-hard, i.e. of the order of few GeV. For an ultrarelativistic large nucleus,

$A \gg 1$, the color density ρ is taken at $x^- = 0$, and it can be approximated as the sum of the large number of color charges of the partons (proportional to $A^{1/3}$) at approximately the same impact parameter $\boldsymbol{x}$. Hence, $W_{Y_0}[\rho]$ can be approximated by a Gaussian distribution in ρ, known as the McLerran-Venugopalan (MV) model [94, 95]. The MV model effectively resums powers of $\alpha_s^2 A^{1/3}$, and its details are given at the end of the next Section 2.2.1. Before that, we first address the quantum corrections, which involve the resummation of powers of $\alpha_s Y$ and are governed by the JIMWLK evolution equation.

2.2.1 The JIMWLK and BK evolution equations

At LO the JIMWLK Hamiltonian can be written as

$$\mathcal{H}[\rho] = \int \mathrm{d}^2\boldsymbol{x}\, \nu^a(\boldsymbol{x}) \frac{\delta}{\delta\rho^a(\boldsymbol{x})} + \frac{1}{2}\int \mathrm{d}^2\boldsymbol{x}\, \mathrm{d}^2\boldsymbol{y}\, \eta^{ab}(\boldsymbol{x},\boldsymbol{y}) \frac{\delta^2}{\delta\rho^a(\boldsymbol{x})\delta\rho^b(\boldsymbol{y})}, \tag{2.30}$$

where the operators $\nu^a(\boldsymbol{x})$ and $\eta^{ab}(\boldsymbol{x},\boldsymbol{y})$ are defined in function of adjoint Wilson lines,

$$\nu^a(\boldsymbol{x}) \equiv \frac{i}{\pi^2 g}\int \frac{\mathrm{d}^2\boldsymbol{z}}{(\boldsymbol{z}-\boldsymbol{x})^2}\, \mathrm{Tr}\big\{T^a U(\boldsymbol{x}) U^\dagger(\boldsymbol{z})\big\}, \tag{2.31}$$

$$\eta^{ab}(\boldsymbol{x},\boldsymbol{y}) \equiv \frac{i}{\pi^2 g^2}\int \mathrm{d}^2\boldsymbol{z} \frac{(\boldsymbol{z}-\boldsymbol{y})\cdot(\boldsymbol{z}-\boldsymbol{y})}{(\boldsymbol{z}-\boldsymbol{x})^2(\boldsymbol{z}-\boldsymbol{y})^2}\left[1 - U(\boldsymbol{y})U^\dagger(\boldsymbol{z}) - U(\boldsymbol{x})U^\dagger(\boldsymbol{z}) + U(\boldsymbol{y})U^\dagger(\boldsymbol{x})\right]^{ab}. \tag{2.32}$$

The evolution equation of an arbitrary operator $\hat{\mathcal{O}}$ is also encoded in the evolution of the weight functional $W_Y[\rho]$, i.e. differentiating Eq. (2.28) with respect to Y we get

$$\partial_Y \langle \hat{\mathcal{O}} \rangle_\rho = \int \mathcal{D}\rho\, \hat{\mathcal{O}}_\rho \partial_Y W_Y[\rho], \tag{2.33}$$

$$= \int \mathcal{D}\rho\, \hat{\mathcal{O}}_\rho \mathcal{H}[\rho] W_Y[\rho], \tag{2.34}$$

$$= \int \mathcal{D}\rho\, \left[\mathcal{H}[\rho]\hat{\mathcal{O}}_\rho\right] W_Y[\rho], \tag{2.35}$$

where we introduced the simplified notation $\partial_Y \equiv \dfrac{\partial}{\partial Y}$ and in the last equality we have integrated by parts. Therefore, the JIMWLK evolution for the expectation value of an arbitrary operator is given by

$$\partial_Y \langle \hat{\mathcal{O}} \rangle = \int \mathrm{d}^2\boldsymbol{x} \left\langle \nu^a(\boldsymbol{x}) \frac{\delta\hat{\mathcal{O}}}{\delta\rho^a(\boldsymbol{x})} \right\rangle + \frac{1}{2}\int \mathrm{d}^2\boldsymbol{x}\, \mathrm{d}^2\boldsymbol{y} \left\langle \eta^{ab}(\boldsymbol{x},\boldsymbol{y}) \frac{\delta^2\hat{\mathcal{O}}}{\delta\rho^a(\boldsymbol{x})\delta\rho^b(\boldsymbol{y})} \right\rangle, \tag{2.36}$$

where we have dropped the explicit dependence of ρ in the operator. In the case of a $q\bar{q}$ dipole-nucleus scattering, the operator $\langle \hat{\mathcal{O}} \rangle$ is given by the S-matrix for the elastic scattering defined as,

$$S(\boldsymbol{x},\boldsymbol{y}) \equiv \frac{1}{N_c}\, \mathrm{tr}\big\{V(\boldsymbol{x})V^\dagger(\boldsymbol{y})\big\}, \tag{2.37}$$

where $V(\boldsymbol{x})$ denotes the fundamental Wilson line discussed in the previous section, the trace denotes that we are considering a colorless dipole and the factor $1/N_c$ stands for the average in color charge. Hence, the evolution of the dipole S-matrix can be found by substituting Eq. (2.37) in Eq. (2.36), by using the definitions in Eqs. (2.31) and (2.32). This calculation involves a considerable amount of algebra which can be simplified with the help of the relations

$$U_{ab}t^b = V^\dagger t^a V, \tag{2.38}$$
$$U^\dagger_{ab}t^b = V t^a V^\dagger \tag{2.39}$$

together with the Fierz identities

$$(t^a)_{ij}(t^a)_{kl} = \frac{1}{2}\left(\delta_{il}\delta_{jk} - \frac{1}{N_c}\delta_{ij}\delta_{kl}\right), \tag{2.40}$$

which for arbitrary $N_c \times N_c$ matrices M_1 and M_2 imply that

$$\mathrm{tr}\{t^a M_1 t^a M_2\} = \frac{1}{2}\,\mathrm{tr}\{M_1\}\,\mathrm{tr}\{M_2\} - \frac{1}{2N_c}\,\mathrm{tr}\{M_1 M_2\} \tag{2.41}$$
$$\mathrm{tr}\{t^a M_1\}\,\mathrm{tr}\{t^a M_2\} = \frac{1}{2}\,\mathrm{tr}\{M_1 M_2\} - \frac{1}{2N_c}\,\mathrm{tr}\{M_1\}\,\mathrm{tr}\{M_2\}. \tag{2.42}$$

After performing the substitution, one arrives to

$$\partial_Y \langle S(\boldsymbol{x},\boldsymbol{y})\rangle = \frac{\bar{\alpha}_s}{2\pi}\int \mathrm{d}^2\boldsymbol{z}\,\frac{(\boldsymbol{y}-\boldsymbol{x})^2}{(\boldsymbol{z}-\boldsymbol{x})^2(\boldsymbol{z}-\boldsymbol{y})^2}\left[\langle S(\boldsymbol{x},\boldsymbol{z})S(\boldsymbol{z},\boldsymbol{y})\rangle - \langle S(\boldsymbol{x},\boldsymbol{y})\rangle\right]. \tag{2.43}$$

It is clear that the evolution equation for the average of an S-matrix is expressed in terms of the average of a product of two S-matrices, which is in fact a four-Wilson-line operator that must evolve again as dictated in Eq. (2.36), and will lead to an operator with six Wilson lines, and so on. This is known as the Balitsky hierarchy, and the related equations are referred to as Balitsky's equations [11]. However, a closed equation can be obtained in the large-N_c limit, where we can make the replacement

$$\langle S(\boldsymbol{y},\boldsymbol{z})S(\boldsymbol{y},\boldsymbol{z})\rangle \to \langle S(\boldsymbol{y},\boldsymbol{z})\rangle\langle S(\boldsymbol{y},\boldsymbol{z})\rangle, \tag{2.44}$$

getting the Balitsky-Kovchegov (BK) evolution equation [11, 12]

$$\partial_Y \langle S(\boldsymbol{x},\boldsymbol{y})\rangle = \frac{\bar{\alpha}_s}{2\pi}\int \mathrm{d}^2\boldsymbol{z}\,\frac{(\boldsymbol{y}-\boldsymbol{x})^2}{(\boldsymbol{z}-\boldsymbol{x})^2(\boldsymbol{z}-\boldsymbol{y})^2}\left[\langle S(\boldsymbol{y},\boldsymbol{z})\rangle\langle S(\boldsymbol{y},\boldsymbol{z})\rangle - \langle S(\boldsymbol{y},\boldsymbol{x})\rangle\right], \tag{2.45}$$

which can be written in terms of the scattering amplitude, $T = 1 - S$, as

$$\begin{aligned}\partial_Y \langle T(\boldsymbol{x},\boldsymbol{y})\rangle =& \frac{\bar{\alpha}_s}{2\pi}\int \mathrm{d}^2\boldsymbol{z}\,\frac{(\boldsymbol{y}-\boldsymbol{x})^2}{(\boldsymbol{z}-\boldsymbol{x})^2(\boldsymbol{z}-\boldsymbol{y})^2}\\ &\times\left[\langle T(\boldsymbol{x},\boldsymbol{z})\rangle + \langle T(\boldsymbol{y},\boldsymbol{z})\rangle - \langle T(\boldsymbol{x},\boldsymbol{y})\rangle - \langle T(\boldsymbol{x},\boldsymbol{z})\rangle\langle T(\boldsymbol{y},\boldsymbol{z})\rangle\right].\end{aligned} \tag{2.46}$$

The linear approximation to the BK equation is known as the Balitsky-Fadin-Kuraev-Lipatov (BFKL) evolution equation [1–3]. It is valid when the scattering amplitude is small, i.e. the regime of weak scattering. When the scattering amplitude approaches the unity, gluon recombination becomes favorable, and the non-linear term drives the evolution, suppressing the growth given by the BFKL equation. The transition between these two regimes is dynamical and occurs at the saturation scale Q_s.

For the case of a gluon (adjoint) dipole, the S-matrix for the dipole-nucleus scattering is given in terms of adjoint Wilson lines, namely

$$S_g(\boldsymbol{x},\boldsymbol{y}) \equiv \frac{1}{N_c^2-1}\,\mathrm{Tr}\big\{U(\boldsymbol{x})U^\dagger(\boldsymbol{y})\big\}, \tag{2.47}$$

where, again, the factor $1/(N_c^2 - 1)$ stands for the average in color charge and the trace is performed to consider colorless dipoles. It is also worth noting that for colorless dipoles, the scattering amplitudes vanish as the dipole size approaches zero, since the color charges of each component cancel each other. This phenomenon is known as *color transparency*.

Initial condition: The MV model

The initial condition of the BK equation can be given by the MV model for a given rapidity Y_0. In this context, we also assume that the nucleus is homogeneous in the transverse plane, i.e., the scattering matrices depend only on differences between pairs of transverse coordinates. Then, the averaged S-matrix for a gluon dipole, $\mathcal{S}_g \equiv \langle S_g \rangle$, can be written as

$$\mathcal{S}_g(\boldsymbol{x}, \boldsymbol{y}) = \exp\left(-\frac{(\boldsymbol{y}-\boldsymbol{x})^2 Q_A^2}{4} \ln \frac{4}{(\boldsymbol{y}-\boldsymbol{x})^2 \Lambda^2}\right), \tag{2.48}$$

where the saturation momentum is given in the scale Q_A^2 via the relation

$$Q_A^2 \ln \frac{Q_s^2}{\Lambda^2} = Q_s^2. \tag{2.49}$$

In the Gaussian approximation, the relation between the averaged adjoint and fundamental S-matrices is given by

$$\mathcal{S}_g(\boldsymbol{x}, \boldsymbol{y}) = [\mathcal{S}(\boldsymbol{x}, \boldsymbol{y})]^{N_c/C_F}, \tag{2.50}$$

with $C_F = (N_c^2 - 1)/2N_c$. We would like to point out here that for numerical purposes, the saturation momentum is defined through the condition $\mathcal{S}_g(r = 2/Q_s) = 1/2$, where $r = |\boldsymbol{y} - \boldsymbol{x}|$. This definition differs slightly from the one used in Eqs. (2.48) and (2.49), which is more suitable for analytical calculations. Additionally, to regularize the infrared behavior of the MV model in Eq. (2.48), we modify the logarithmic term as $\ln(4/r^2\Lambda^2) \to 2\ln[(2/r\Lambda) + e]$.

2.2.2 Collinearly improved BK equation

At next-to-leading order (NLO), the JIMWLK equation includes the resummation of terms which are of order $\alpha_s[\alpha_s \ln 1/x]^n$, and the explicit Hamiltonian was derived in [96, 97]. The NLO BK equation was derived previously and fully presented in [98]. In this work, we will use the simplified form of the NLO BK equation, developed by unambiguously using the rapidity $Y = \ln 1/x$ as the evolution time of the hadronic target: the *collinearly-improved* Balitsky-Kovchegov (collBK) equation [99, 100]. The collBK equation is non-local in rapidity, and the version used in this work reads

$$\partial_Y \mathcal{S}_{\boldsymbol{xy}}(Y) = \int \frac{\mathrm{d}^2\boldsymbol{z}}{2\pi}\, \bar{\alpha}_{\mathrm{BLM}} \frac{(\boldsymbol{x}-\boldsymbol{y})^2}{(\boldsymbol{x}-\boldsymbol{z})^2(\boldsymbol{z}-\boldsymbol{y})^2} \left[\frac{r^2}{\bar{z}^2}\right]^{\pm A_1} \left[\mathcal{S}_{\boldsymbol{xz}}(Y - \delta_{\boldsymbol{xz};r})\mathcal{S}_{\boldsymbol{zy}}(Y - \delta_{\boldsymbol{zy};r}) - \mathcal{S}_{\boldsymbol{xy}}(Y)\right], \tag{2.51}$$

where the coordinate dependence of the averaged S-matrices is now shown in the subscript and the rapidity shifts, explicitly shown in the argument of the daughter dipole scattering matrices, are given by

$$\delta_{\boldsymbol{xz};r} \equiv \max\left\{0, \ln \frac{r^2}{|\boldsymbol{x}-\boldsymbol{z}|^2}\right\}, \tag{2.52}$$

with $r = |\boldsymbol{x} - \boldsymbol{y}|$, and similarly for $\delta_{\boldsymbol{zy};r}$. They resum all-order double logarithms generated by the successive gluon emissions. The resummation of the DGLAP-like single transverse logarithms is given by the factor $\left[r^2/\bar{z}^2\right]^{\pm A_1}$, where $\bar{z} \equiv \min|\boldsymbol{x}-\boldsymbol{z}|, |\boldsymbol{x}-\boldsymbol{y}|$ and $A_1 = 11/12$. The exponent $\pm A_1$ always suppresses the evolution, as it is positive when $r^2 < \bar{z}^2$ and negative when $r^2 > \bar{z}^2$. The running coupling $\bar{\alpha}_{\text{BLM}}$ encodes the corrections given by the one-loop QCD β-function and is given by

$$\bar{\alpha}_{\text{BLM}} = \left[\frac{1}{\bar{\alpha}_s(|\boldsymbol{x}-\boldsymbol{y}|)} + \frac{(\boldsymbol{x}-\boldsymbol{z})^2 - (\boldsymbol{z}-\boldsymbol{y})^2}{(\boldsymbol{x}-\boldsymbol{y})^2} \frac{\bar{\alpha}_s(|\boldsymbol{x}-\boldsymbol{z}|) - \bar{\alpha}_s(|\boldsymbol{z}-\boldsymbol{y}|)}{\bar{\alpha}_s(|\boldsymbol{x}-\boldsymbol{z}|)\bar{\alpha}_s(|\boldsymbol{z}-\boldsymbol{y}|)}\right]^{-1}, \tag{2.53}$$

where

$$\bar{\alpha}_s(r) = \frac{1}{\bar{b}_0 \ln\left[4/(r_*^2\Lambda^2)\right]}, \tag{2.54}$$

with $\bar{b}_0 = 0.75$, $\Lambda = 0.2$ GeV, and $r* = r/\sqrt{1 + r^2/r_{\text{max}}^2}$, where $r_{\text{max}} = 4$ GeV^{-1}. The values of $\bar{\alpha}_{\text{BLM}}$ reduce to $\bar{\alpha}_s(r_{\text{min}})$, where $r_{\text{min}} \equiv \min|\boldsymbol{x}-\boldsymbol{y}|, |\boldsymbol{x}-\boldsymbol{z}|, |\boldsymbol{z}-\boldsymbol{y}|$, when one of the three dipoles has a much smaller size compared to the other two, which is a condition required by pQCD for the applicability of the approximation. When starting the evolution for a given rapidity Y_0, we assume a constant behavior for values of $Y < Y_0$, meaning that

$$S_{\boldsymbol{xy}}(Y < Y_0) = S_{\boldsymbol{xy}}(Y_0), \tag{2.55}$$

and where $S_{\boldsymbol{xy}}(Y_0)$ is given by the MV model.

Chapter 3

Coherent and Incoherent Diffraction

In hadronic scattering, a diffractive process can be defined as a high energy reaction in which no quantum numbers are exchanged between the colliding particles. An equivalent definition is that a diffractive process is characterized by an angular separation in which no particles are produced, a *rapidity gap* ΔY, in the final state. The dominant contribution to diffractive processes is usually referred as *Pomeron*[1] exchange, which in QCD refers to the exchange of an even number of gluons. In fact, the diffractive constraint in high-energy QCD scattering means that the final states arise in a color-singlet state after the interaction.

For a wide discussion of diffractive processes see [87] and [101], here instead, for definiteness we will focus on diffractive photon-nucleus DIS.

3.1 Diffraction in the dipole picture

In particular, we consider *low-mass* diffraction, where the invariant mass of the outgoing projectile state, M_χ, is much smaller than the virtuality, i.e., $M_\chi \ll Q$. In the dipole picture, this outgoing state is described by the jets produced after the scattering of the partonic fluctuation of the virtual photon off the hadronic target. At LO in the strong coupling, and assuming the target remains unchanged after the collision, the total DIS cross section for photon-nucleus scattering can be written as

$$\sigma_{tot}^{\gamma^* A} = \int \frac{\mathrm{d}^2\boldsymbol{r}}{2\pi} \int_0^1 \frac{\mathrm{d}\vartheta}{\vartheta(1-\vartheta)} |\psi^{\gamma^*\to q\bar{q}}|^2 \; S_\perp \mathcal{T}(\boldsymbol{r}). \tag{3.1}$$

where $S_\perp$ is the transverse area of the target, which arises from neglecting the impact parameter dependence[2] in the averaged scattering amplitude $\mathcal{T} = 1 - \mathcal{S}$. Since we are assuming S-matrices that depend only on the difference between pairs of transverse coordinates, the coordinate dependence of $\mathcal{T}$ is determined solely by the dipole size, $\boldsymbol{r}$, while the rapidity dependence is left implicit. The quark longitudinal fraction, ϑ, is defined as the fraction of the longitudinal momentum of the virtual photon, q^+, carried by the quark. The wave function $\psi^{\gamma^*\to q\bar{q}}$ encodes the

[1]Named after the Soviet physicist Isaac Yakovlevich Pomeranchuk for his contributions to hadronic diffractive physics.

[2]This simplification will be assumed throughout this work since we focus in large quasi-homogeneous targets, in which the impact parameter is not expected to play a relevant role. However, to consider a realistic description of the experiments involving proton targets, it is necessary to address the impact parameter dependence in the cross sections. See, e.g. [102] for a recent study of its effects in proton and nuclear targets

fluctuation of the virtual photon into a $q\bar{q}$ pair. The dipole-nucleus total cross section can be written by omitting the expression related to the virtual photon, i.e.,

$$\sigma_{tot}^{q\bar{q}A} = 2\ S_{\perp}\mathcal{T}(\boldsymbol{r}). \tag{3.2}$$

By the unitarity of the S-matrix, we also know that *elastic* $2 \to 2$ scattering — which implies that there is no quantum number exchange in the process and thus describes diffraction — is given by the cross section [3]

$$\sigma_{el}^{q\bar{q}A} = S_{\perp}|\mathcal{T}(\boldsymbol{r}, Y)|^2. \tag{3.3}$$

When the scattering is strong, the $\mathcal{T}$-matrix approaches one. By inspecting the ratio $\sigma_{\rm tot}^{q\bar{q}A}/\sigma_{\rm el}^{q\bar{q}A}$, it is evident that the diffractive cross section represents half of the total DIS cross section. The $\mathcal{T} \to 1$ limit is known as the *black disk* limit, and in terms of saturation physics, this is the regime where the saturation scale controls the non-linear behavior of the scattering. In other words, diffractive processes are controlled by gluon saturation. On the other hand, diffractive processes are generally suppressed in the dilute regime due to color transparency. Hence, diffraction is a significant process for probing saturation.

In the dipole frame, the diffractive process is specified by the elastic scattering of the partons in the photon light-cone wave function of the virtual photon off the nucleus. The final state of the nucleus dictates the type of diffraction. The process is coherent if the nucleus remains intact after the collision, while it is incoherent if the nucleus breaks up.

3.1.1 On coherence and incoherence

To calculate the diffractive cross section, the nucleus is described within the CGC framework. We must then consider the average over all possible configurations. The detailed formulas for all relevant cross sections will be provided in the following chapters. Here, we will focus instead on the general characteristics that distinguish coherent and incoherent diffractive processes. To be precise, considering the T-matrix for the projectile to scatter elastically off the nucleus in the direct amplitude (DA) as T, while $\bar{T}$ represents the corresponding quantity in the complex conjugated amplitude (CCA), we can express the total diffractive cross section as

$$\sigma^{\rm D} \propto \langle T\bar{T}\rangle, \tag{3.4}$$

where all the dependencies and integrations over the various variables are suppressed. The total diffractive cross section includes both the coherent and incoherent contributions. The coherent part corresponds to an intact nucleus in the final state, so the averaging must be performed at the amplitude level, i.e.,

$$\sigma^{\rm D}_{\rm coh} \propto \langle T\rangle\langle\bar{T}\rangle. \tag{3.5}$$

The coherent diffractive production of jets has been extensively studied in the last few years [52, 55, 56, 60]. Here, we shall only mention the main results that arise when comparing it to the incoherent production. The incoherent contribution to the diffractive cross section is defined as the complementary part of the coherent contribution with respect to the total diffractive cross section, namely

$$\sigma^{\rm D}_{\rm inc} = \sigma^{\rm D} - \sigma^{\rm D}_{\rm coh} \propto \langle T\bar{T}\rangle - \langle T\rangle\langle\bar{T}\rangle. \tag{3.6}$$

[3]See, e.g., Appendix B in [10] for details

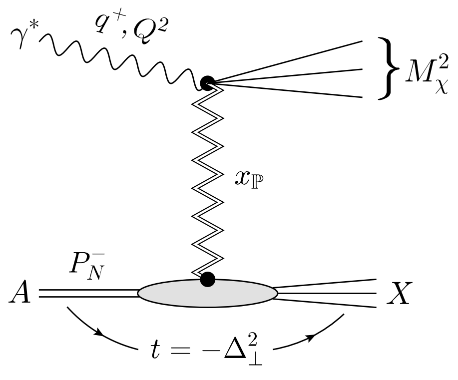

Figure 3.1: Generic diagram for the incoherent reaction $\gamma^* A \to \chi X$.

This expression suggests that incoherent diffraction is determined by fluctuations in the target's weight function. In electron-proton DIS, studies on geometrical fluctuations in the shape of the proton have been conducted with significant success in describing experimental results [62, 103, 104]. Particle number fluctuations via QCD Pomeron loops [105–109] have also been explored in the literature, although due to technical challenges, this approach has not been significantly pursued. Our work, compiled here, relies on the analytical study of color fluctuations [34, 61, 63, 64], which arise from color exchanges between different substructures within the nucleus, specifically due to perturbative gluon exchanges.

Before discussing incoherent processes in detail, we introduce the relevant kinematic variables in diffraction. For instance, an important kinematic variable is the transverse momentum transfer, $\boldsymbol{\Delta}$. This can arise due to geometrical fluctuations as mentioned for *ep* DIS. However, when the target is a large homogeneous nucleus, the associated momentum transfer is non-perturbative and thus negligible for our purposes. This fact is explicitly seen when calculating the coherent cross section, where the contribution of the transferred momentum is given by a δ-function in $\boldsymbol{\Delta}$. In incoherent diffraction, on the other hand, the color fluctuations set the momentum transfer to be of the order of the saturation momentum.

It is also important to define two additional kinematic invariants in diffraction, namely

$$x_{\mathbb{P}} \equiv \frac{Q^2 + M_\chi^2 + |t|}{s} \qquad \text{and} \qquad \beta \equiv \frac{Q^2}{Q^2 + M_\chi^2 + |t|}, \tag{3.7}$$

where $t = -\Delta_\perp^2$ is the invariant momentum transfer and M_χ^2 is the aforementioned invariant mass of the diffractive system. The invariant mass, as well as $x_{\mathbb{P}}$ and β, can be explicitly determined in terms of the kinematics of a given outgoing state. The physical interpretation of $x_{\mathbb{P}}$ is that it represents the fraction of the target's longitudinal momentum, P_N^-, carried by the Pomeron and transferred to the diffractive system after the collision. The two variables in Eq. (3.7) are not independent; they follow the relation

$$x_{\text{Bj}} = \beta x_{\mathbb{P}} \;\; \Rightarrow \;\; Y_{\text{Bj}} = Y_\beta + Y_{\mathbb{P}}, \tag{3.8}$$

which can be inferred from the definition of x_{Bj} in Eq. (1.12). The corresponding rapidities are also defined in Eq. (3.8). In fact, $Y_{\mathbb{P}}$ determines the value of the desired rapidity gap, while $Y_\beta \equiv \ln 1/\beta$ corresponds to the rapidity interval occupied by the diffractive system. Therefore, it is evident that their sum must be equal to $Y_{\text{Bj}} \equiv \ln 1/x_{\text{Bj}}$. The projectile as a whole probes the target at the longitudinal scale $x_{\mathbb{P}}$, meaning that the relevant value of the saturation momentum is given by $Q_s(Y_{\mathbb{P}})$. A general diagram for the incoherent diffractive reaction $\gamma^* A \to \chi X$ is shown in Fig. 3.1, where neither the specific dynamics nor the precise nature of the outgoing states χ and X are specified.

3.1.2 Incoherent diffraction in the CGC

From Eq. (3.6), it is clear that the incoherent cross section is determined by the connected part of the DA and CCA. By isolating the factor that encodes the QCD dynamics, explicitly shown in Eq. (3.6) by the replacement $S = 1 - T$, we can define the *incoherent diffractive correlator* as

$$\mathcal{W}_{\mathrm{D}} = \langle S(\boldsymbol{x}, \boldsymbol{y}) S(\bar{\boldsymbol{y}}, \bar{\boldsymbol{x}}) \rangle - \langle S(\boldsymbol{x}, \boldsymbol{y}) \rangle \langle S(\bar{\boldsymbol{y}}, \bar{\boldsymbol{x}}) \rangle , \tag{3.9}$$

where the dipole coordinate dependence is now explicitly shown in the argument of the S-matrices. The correlator can be in the fundamental or adjoint representation, depending on whether the dipole projectile is given by a $q\bar{q}$ pair or a gluon-gluon pair, respectively. In the lowest order in the number of gluon exchanges, each amplitude of the projectile dipole contributes with two gluons, so at the cross section level there are 4-gluon exchanges.

For our purposes, it is also customary to define the distance between the dipoles in the CA and CCA, $\boldsymbol{B} \equiv \boldsymbol{b} - \bar{\boldsymbol{b}}$, where $\boldsymbol{b}$ is the impact parameter in the DA (similarly $\bar{\boldsymbol{b}}$ in CCA). The impact parameter is given by the relation $\boldsymbol{b} = \vartheta_1 \boldsymbol{x} + \vartheta_2 \boldsymbol{y}$, where ϑ_1 is the longitudinal momentum fraction carried by one component of the dipole, while $\vartheta_2 \equiv 1 - \vartheta_1$ is the same in its complementary component.

Let us consider dipole sizes and the difference of impact parameters to be much smaller than the saturation momentum. Then the elastic scattering S-matrix Eq. (2.37) in the DA can be expanded as

$$S(\boldsymbol{x}, \boldsymbol{y}) \simeq 1 - \frac{g^2}{4N_c} \left(\alpha^a_{\boldsymbol{x}} - \alpha^a_{\boldsymbol{y}}\right)^2 \quad \text{with} \quad \alpha^a_{\boldsymbol{x}} \equiv \int_{-\infty}^{\infty} \mathrm{d}x^+ A^-_a(x^+, \boldsymbol{x}), \tag{3.10}$$

where A_a is the color potential of the CGC. A similar expression is given for $S(\bar{\boldsymbol{y}}, \bar{\boldsymbol{x}})$, where, as in the case of the impact parameter $\bar{\boldsymbol{b}}$, the bars over the coordinates represent that they belong to the CCA. Then the relevant terms are the ones that involve color contraction of one field in the DA with a field in the CCA. For example, one of those terms is given by the contraction of the object $g^4 \langle \alpha^a_{\boldsymbol{x}} \, \alpha^b_{\bar{\boldsymbol{y}}} \rangle \langle \alpha^a_{\boldsymbol{y}} \, \alpha^b_{\bar{\boldsymbol{x}}} \rangle / 4N_c^2$. By considering that the correlator of two fields is diagonal in color we get the relation

$$\frac{g^4}{4N_c^2} \sum_{a,b} \langle \alpha^a_{\boldsymbol{x}} \, \alpha^b_{\bar{\boldsymbol{y}}} \rangle \langle \alpha^a_{\boldsymbol{y}} \, \alpha^b_{\bar{\boldsymbol{x}}} \rangle = \frac{g^4}{4N_c^2} \sum_{a} \langle \alpha^a_{\boldsymbol{x}} \, \alpha^a_{\bar{\boldsymbol{y}}} \rangle \langle \alpha^a_{\boldsymbol{y}} \, \alpha^a_{\bar{\boldsymbol{x}}} \rangle, \tag{3.11}$$

where the summations over the color indices of the exchanged gluons are explicitly shown to avoid any confusion. The single summation over a implies that in the l.h.s. only one gluon color flows. On the other hand, when two independent gluon colors are summed over, and assuming that in the Gaussian approximation every component of the gauge field has equal weight, we must divide the corresponding contributions by the number of colors in order to get an equality with the expressions in Eq. (3.11), i.e.,

$$\frac{g^4}{4N_c^2} \sum_{a,b} \langle \alpha^a_{\boldsymbol{x}} \, \alpha^b_{\bar{\boldsymbol{y}}} \rangle \langle \alpha^a_{\boldsymbol{y}} \, \alpha^b_{\bar{\boldsymbol{x}}} \rangle = \frac{g^4}{4N_c^2} \sum_{a} \langle \alpha^a_{\boldsymbol{x}} \, \alpha^a_{\bar{\boldsymbol{y}}} \rangle \langle \alpha^a_{\boldsymbol{y}} \, \alpha^a_{\bar{\boldsymbol{x}}} \rangle = \sum_{a,b} \frac{g^4}{4N_c^2(N_c^2-1)} \langle \alpha^a_{\boldsymbol{x}} \, \alpha^a_{\bar{\boldsymbol{y}}} \rangle \langle \alpha^b_{\boldsymbol{y}} \, \alpha^b_{\bar{\boldsymbol{x}}} \rangle. \tag{3.12}$$

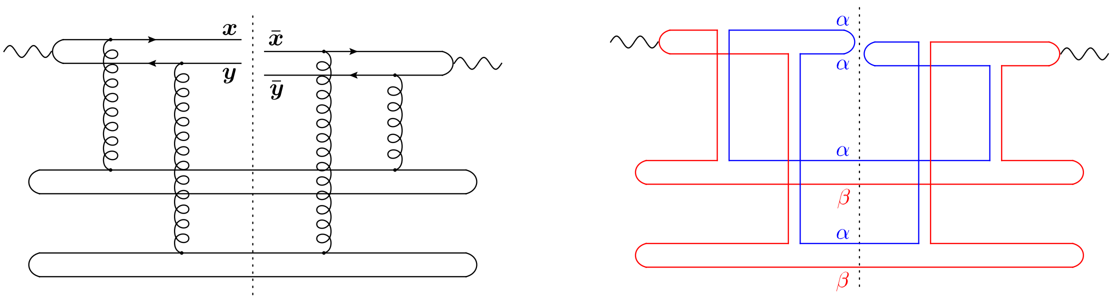

Figure 3.2: Left panel: Diagram of incoherent diffractive dijet production at the level of four-gluon exchange. This corresponds to Eq. (3.11), which is part of the product $\langle T(\boldsymbol{x}, \bar{\boldsymbol{y}})\rangle \langle T(\boldsymbol{y}, \bar{\boldsymbol{x}})\rangle$. Each of the two lower double lines, representing colorless substructures (nucleons) within the nucleus, exchanges a single gluon with the projectile $q\bar{q}$ pair in the DA (and one in the CCA), resulting in inelastic scattering. Right panel: The same process in the large-N_c limit, where gluons are represented by double lines. In this case, the substructures are no longer colorless in the final state, indicating that the nucleus does not remain intact. Two independent color flows, α and β (in the fundamental representation), are present, and the diagram is of order $g^8 N_c^2$.

This expression shows that the connected piece of the total diffractive correlator $\mathcal{W}_{\rm D}$ is suppressed by a factor of $1/N_c^2$ in the large-N_c limit. Combining all the possible terms, the correlator can be written as

$$\mathcal{W}_{\rm D} \simeq \frac{g^4}{8N_c^2(N_c^2-1)} \left[\left\langle \alpha^a_{\boldsymbol{x}}\, \alpha^a_{\bar{\boldsymbol{x}}}\right\rangle + \left\langle \alpha^a_{\boldsymbol{y}}\, \alpha^a_{\bar{\boldsymbol{y}}}\right\rangle - \left\langle \alpha^a_{\boldsymbol{x}}\, \alpha^a_{\bar{\boldsymbol{y}}}\right\rangle - \left\langle \alpha^a_{\boldsymbol{y}}\, \alpha^a_{\bar{\boldsymbol{x}}}\right\rangle\right]^2. \tag{3.13}$$

Then, at two-gluon exchange, we can reconstruct the average values of the scattering amplitudes by adding and subtracting "equal-point correlators" of the form $\left\langle \alpha^a_{\boldsymbol{x}} \alpha^a_{\boldsymbol{x}}\right\rangle$, i.e.,

$$\mathcal{W}_{\rm D} \simeq \frac{1}{2(N_c^2-1)} \left[\langle T(\boldsymbol{x}, \bar{\boldsymbol{y}})\rangle + \langle T(\boldsymbol{y}, \bar{\boldsymbol{x}})\rangle - \langle T(\boldsymbol{x}, \bar{\boldsymbol{x}})\rangle - \langle T(\boldsymbol{y}, \bar{\boldsymbol{y}})\rangle\right]^2. \tag{3.14}$$

A typical diagram for four-gluon exchange corresponding to incoherent diffraction is shown in Fig.3.2, along with the illustration of color flow in the large-N_c limit. For comparison, the corresponding diagram in the coherent sector is shown in Fig.3.3.

An interesting configuration to consider is when the dipole sizes $\boldsymbol{r}, \bar{\boldsymbol{r}}$ are small compared to the distance between the dipoles in each scattering amplitude, $\boldsymbol{B}$. This allows us to expand all the amplitudes in Eq. (3.14) around $\boldsymbol{B}$, since they all involve one leg in the DA and the other in the CCA. This configuration will be analyzed in detail in the $q\bar{q}$ contribution to the total incoherent diffractive DIS cross section.

By performing this expansion, we observe that the lowest-order term in the linear combination inside the squared bracket in Eq. (3.14) is quadratic, since the process is elastic on the projectile side. In other words, we find

$$\mathcal{T}(\boldsymbol{x}, \bar{\boldsymbol{y}}) + \mathcal{T}(\boldsymbol{y}, \bar{\boldsymbol{x}}) - \mathcal{T}(\boldsymbol{x}, \bar{\boldsymbol{x}}) - \mathcal{T}(\boldsymbol{y}, \bar{\boldsymbol{y}}) \simeq r^i \bar{r}^j \partial^i \partial^j \mathcal{T}(\boldsymbol{B}), \tag{3.15}$$

where again we use the calligraphic symbol for the average of a quantity. Thus, Eq. (3.14) can be rewritten as

$$\mathcal{W}_{\rm D}(\boldsymbol{r}, \bar{\boldsymbol{r}}, \boldsymbol{B}) \simeq \frac{1}{2(N_c^2-1)} r^i \bar{r}^j r^k \bar{r}^l \partial^i \partial^j \mathcal{T}(\boldsymbol{B}) \partial^k \partial^l \mathcal{T}(\boldsymbol{B}). \tag{3.16}$$

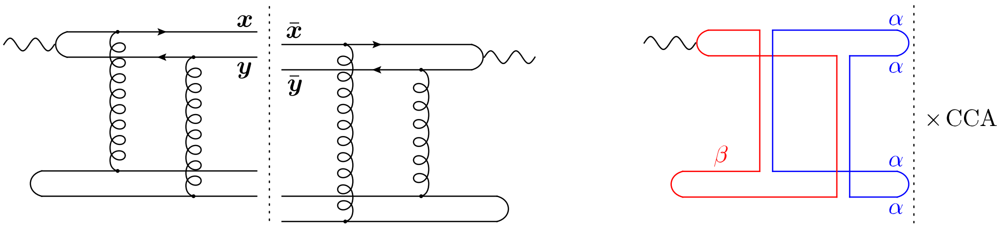

Figure 3.3: Left panel: A diagram for coherent diffractive dijet production, generally proportional to $\langle T(\boldsymbol{x},\boldsymbol{y})\rangle\langle T(\bar{\boldsymbol{y}},\bar{\boldsymbol{x}})\rangle$, at the level of four-gluon exchange. A colorless substructure (nucleon) in the nucleus exchanges two gluons with the projectile $q\bar{q}$ pair in the DA (and similarly with a potentially different nucleon in the CCA), resulting in elastic scattering. Right panel: The same process in the large-N_c limit, where the gluons are represented by double lines. The nucleon remains intact. Two independent colors flow in the DA, and another two in the CCA, leading to a total diagram of order $g^8 N_c^4$.

Again, we emphasize that this expression for the diffractive correlator is valid in the Gaussian approximation at the level of four-gluon exchange when $r, \bar{r} \ll B \ll 1/Q_s$. In the next chapter, we extend this analysis to the regime where $r, \bar{r} \ll B, 1/Q_s$, i.e. without imposing any constraints on the relative magnitudes of the saturation momentum and difference between impact parameters.

Chapter 4

The $q\bar{q}$ Contribution

The goal of this chapter is to provide an analytical understanding of the cross section for incoherent diffractive dijet production in high-energy DIS of a virtual photon γ^* off a large nucleus with atomic number A. To this end, we first review the kinematics in which we work. We consider a frame where both incoming particles are ultrarelativistic. In light-cone notation, the photon is a right mover with virtuality $q^\mu q_\mu = -Q^2$ and 4-momentum $q^\mu = (q^+, -Q^2/2q^+, \mathbf{0})$. The nucleus is a left mover, and we neglect the mass of the nucleons, so its 4-momentum per nucleon is given by $P_N^\mu = (0, P_N^-, \mathbf{0})$. Thus, the virtual photon decays into a $q\bar{q}$ pair, whose lifetime is much larger than the longitudinal extent of the boosted nucleus. This allows the scattering process to be well described by the collision between the $q\bar{q}$ dipole and the nucleus in the regime where $x_{\text{Bj}} A^{1/3} \ll 1$.

In this context, the nucleus can be at saturation, generating a strong color field. Therefore, it becomes necessary to account for multiple scattering. We also work in the kinematics where the scattering occurs in the eikonal limit, and after the collision, the $q\bar{q}$ pair produces a dijet system in the forward direction of the virtual photon. The produced dijet remains colorless and acquire a momentum transfer $\mathbf{\Delta}$ from the nucleus due to the exchange of color between its subnuclear components.

This process was numerically studied in [34] in the regime where all momenta are of the order of the saturation momentum, i.e., $k_{1\perp} \sim k_{2\perp} \sim \Delta_\perp \sim Q_s$, with $\Delta_\perp \equiv |\boldsymbol{k}_1 + \boldsymbol{k}_2|$ and where $\boldsymbol{k}_1$ and $\boldsymbol{k}_2$ are the final transverse momenta of the quark and antiquark, respectively. In our work, we consider the *correlation limit*, in which the transverse momenta of the two jets are much larger than the saturation momentum. In this limit, the transverse momentum hierarchy satisfies $k_{1\perp} \sim k_{2\perp} \gg Q_s, \Delta_\perp$ (with no assumption regarding the relation between $\Delta_\perp$ and Q_s), meaning that the two jets propagate approximately back-to-back in the transverse plane. It is important to note that in the process under consideration, the dijet imbalance $\boldsymbol{k}_1 + \boldsymbol{k}_2$ and the momentum transfer from the target $\mathbf{\Delta}$ are the same, since there are no other particles between the dijet and the nucleus in the final state.

This limit allows us to perform analytical calculations, which, as we will show below, accurately describe the phenomenon under study. It is also important to emphasize that the most interesting case occurs when the momentum transfer is of the order of or smaller than the saturation momentum, as this is when unitarity corrections and gluon saturation become relevant, even though two hard jets are being produced.

We begin by briefly reviewing the $q\bar{q}$ component of the light-cone wave function (LCWF) of the virtual photon in the framework of light-cone perturbation theory (LCPT). Our analysis focuses explicitly on the case of a transverse virtual photon to avoid unnecessary proliferation of

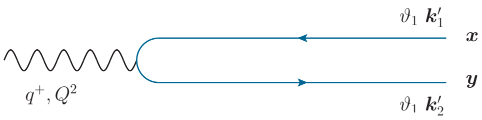

Figure 4.1: Feynman diagram in light-cone perturbation theory describing the quark-antiquark fluctuation.

equations. A brief discussion of the longitudinal polarization case will be presented at the end of Section 4.1, and the corresponding cross section will be provided as a final result after we derive the transverse case.

In Fig. 4.1, we show the Feynman diagram for the virtual photon splitting into a quark-antiquark pair, along with the respective variables in momentum space and transverse coordinates. The DA in momentum space is given by

$$\begin{aligned}\left|\gamma_T^i(q)\right\rangle_{q\bar{q}} = \sum_{\lambda_{1,2}=\pm 1/2} \sum_{\alpha,\beta=1}^{N_c} \int_0^1 \mathrm{d}\vartheta_1 \mathrm{d}\vartheta_2\, \delta(1-\vartheta_1-\vartheta_2) \int \mathrm{d}^2\boldsymbol{k}_1' \mathrm{d}^2\boldsymbol{k}_2'\, \delta^{(2)}(\boldsymbol{k}_1'+\boldsymbol{k}_2') \\ \times \psi^i_{\lambda_1\lambda_2}(\vartheta_1,\boldsymbol{k}_1')\, \delta_{\alpha\beta} \left| q^\alpha_{\lambda_1}(\vartheta_1,\boldsymbol{k}_1')\, \bar{q}^\beta_{\lambda_2}(\vartheta_2,\boldsymbol{k}_2')\right\rangle, \qquad (4.1)\end{aligned}$$

where the index $i = 1, 2$ represents the polarization of the transverse photon, and α and β are color indices in the fundamental representation. For the quark (and similarly for the antiquark), λ_1 and ϑ_1 denote the helicity state and the longitudinal momentum fraction with respect to the virtual photon. The transverse momenta of the quark and antiquark before the scattering are represented by $\boldsymbol{k}_1'$ and $\boldsymbol{k}_2'$, respectively, and are primed to distinguish them from the final momenta $\boldsymbol{k}_1$ and $\boldsymbol{k}_2$. The delta function $\delta(1-\vartheta_1-\vartheta_2)$ represents the conservation of longitudinal momentum, while $\delta^{(2)}(\boldsymbol{k}_1'+\boldsymbol{k}_2')$ ensures the conservation of transverse momentum.

The amplitude $\psi^i_{\lambda_1\lambda_2}$ in Eq. (4.1) encodes the splitting of the virtual photon into the $q\bar{q}$ pair and is given by

$$\psi^i_{\lambda_1\lambda_2}(\vartheta,\boldsymbol{k}) = \sqrt{\frac{q^+}{2}}\, \frac{ee_f}{(2\pi)^3}\, \frac{\varphi^{il}_{\lambda_1\lambda_2}(\vartheta)\, k^l}{\boldsymbol{k}^2+\vartheta(1-\vartheta)Q^2}, \qquad (4.2)$$

where q^+ is the plus longitudinal momentum of the virtual photon, e is the electric charge, and e_f is the fractional electric charge of the quark flavor under consideration. The function $\varphi^{il}_{\lambda_1\lambda_2}(\vartheta)$ represents the helicity structure of the photon splitting vertex and is given by

$$\varphi^{il}_{\lambda_1\lambda_2}(\vartheta) = \delta_{\lambda_1\lambda_2}\left[(2\vartheta-1)\delta^{il} + 2i\varepsilon^{il}\lambda_1\right]. \qquad (4.3)$$

The denominator in Eq. (4.2) comes from the contribution of the energy denominator $E_{q\bar{q}} - E_\gamma$, according to the LCPT rules, which reads

$$E_{q\bar{q}} - E_\gamma = \frac{1}{2q^+}\left(\frac{\boldsymbol{k}_1'^2}{\vartheta_1} + \frac{\boldsymbol{k}_2'^2}{\vartheta_2} + Q^2\right) = \frac{1}{2q^+\vartheta_1\vartheta_2}\left(\boldsymbol{k}_1'^2 + \vartheta_1\vartheta_2 Q^2\right). \qquad (4.4)$$

As discussed in section 2.1.1, in the eikonal limit, it is convenient to work in the mixed representation. Thus, we perform a Fourier transform of the quark states in momentum space according to

$$\left| q^\alpha_{\lambda_1}(\vartheta_1,\boldsymbol{k}_1')\, \bar{q}^\beta_{\lambda_2}(\vartheta_2,\boldsymbol{k}_2')\right\rangle = \int \mathrm{d}^2\boldsymbol{x}\, \mathrm{d}^2\boldsymbol{y}\, e^{-i\boldsymbol{k}_1'\cdot\boldsymbol{x}-i\boldsymbol{k}_2'\cdot\boldsymbol{y}} \left| q^\alpha_{\lambda_1}(\vartheta_1,\boldsymbol{x})\, \bar{q}^\beta_{\lambda_2}(\vartheta_2,\boldsymbol{y})\right\rangle, \qquad (4.5)$$

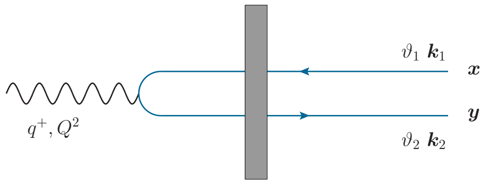

Figure 4.2: Feynman diagram representing the amplitude for the scattering between the $q\bar{q}$ pair and the nuclear target in the shockwave formalism.

where we explicitly show $\boldsymbol{x}$ and $\boldsymbol{y}$ as the corresponding transverse coordinates of the quark and the antiquark. The integration over the initial transverse momenta $\boldsymbol{k}_1'$ and $\boldsymbol{k}_2'$ then leads to

$$\big|\gamma_T^i(q)\big\rangle_{q\bar{q}} = \sum_{\lambda_{1,2}=\pm 1/2}\ \sum_{\alpha,\beta=1}^{N_c} \int_0^1 \mathrm{d}\vartheta_1 \mathrm{d}\vartheta_2\, \delta(1-\vartheta_1-\vartheta_2) \int \mathrm{d}^2\boldsymbol{x}\, \mathrm{d}^2\boldsymbol{y}$$
$$\times\, \widetilde{\psi}^i_{\lambda_1\lambda_2}(\vartheta_1,\boldsymbol{r})\, \delta_{\alpha\beta} \big| q^\alpha_{\lambda_1}(\vartheta_1,\boldsymbol{x})\, \bar{q}^\beta_{\lambda_2}(\vartheta_2,\boldsymbol{y})\big\rangle, \tag{4.6}$$

where we remind that $\boldsymbol{r} = \boldsymbol{x} - \boldsymbol{y}$. Now, in coordinate space, the $q\bar{q}$ amplitude reads

$$\widetilde{\psi}^i_{\lambda_1\lambda_2}(\vartheta,\boldsymbol{r}) = -\sqrt{\frac{q^+}{2}}\, \frac{iee_f}{(2\pi)^2}\, \varphi^{il}_{\lambda_1\lambda_2}(\vartheta)\, \frac{\bar{Q}r^l}{r} K_1(\bar{Q}r). \tag{4.7}$$

where we have defined $\bar{Q}^2 = \vartheta_1\vartheta_2 Q^2$ and $r = |\boldsymbol{r}|$. K_1 is the modified Bessel function of the second kind, which exponentially suppresses the decay of the virtual photon to dipoles with a size much larger than $1/\bar{Q}$.

4.1 Multiple scattering off the target

We shall add the effects of multiple scattering off the nuclear target in the eikonal approximation. In the kinematics of interest, the nuclear target can be treated as a shockwave due to Lorentz contraction (see Fig. 4.2) and the scattering of each parton in the color dipole is given by a Wilson line. The Wilson line for the quark interaction $V(\boldsymbol{x})$ ($V^\dagger(\boldsymbol{x})$ for the antiquark) is defined in Eq. (2.22) and rewritten here in the proper notation of our present pourposes,

$$V(\boldsymbol{x}) = T \exp\left[ig \int \mathrm{d}x^+ t^a A^-_a(x^+, 0, \boldsymbol{x})\right], \tag{4.8}$$

where we have dropped the + index in the T, which indicates time ordering in light-cone time. We remind that g is the QCD coupling, t^a is the SU(N_c) color matrix in the fundamental representation, and A^-_a, with $a = 1, \ldots, N_c^2 - 1$, represents the small-x gluons in the target.

The multiple scattering of a $q\bar{q}$ pair off the nuclear target takes the form $\big[V(\boldsymbol{x})V^\dagger(\boldsymbol{y}) - \mathbb{1}\big]_{\alpha\beta}$, where the identity matrix represents processes with no interaction. Then, the multiple scattering of a color dipole in the fundamental representation can be included in the scattering amplitude in Eq. (4.6) by making the replacement

$$\delta_{\alpha\beta} \to \big[V(\boldsymbol{x})V^\dagger(\boldsymbol{y}) - \mathbb{1}\big]_{\alpha\beta}. \tag{4.9}$$

Such a replacement corresponds to the *inclusive* production of dijets, where there is no restriction on the final state of the projectile. In the particular case of an incoming colorless $q\bar{q}$ dipole, the product of the Wilson lines must be color-averaged, i.e., traced and divided by a factor of N_c. Furthermore, the scattering must be elastic, that is, the color dipole must emerge as a color singlet in the final state, which is a requirement for the process to be diffractive. Thus, in the scattering amplitude Eq. (4.6), we further make the replacement

$$\left[V(\boldsymbol{x})V^\dagger(\boldsymbol{y}) - \mathbb{1}\right]_{\alpha\beta} \to \left\{\frac{1}{N_c}\,\mathrm{tr}\left[V(\boldsymbol{x})V^\dagger(\boldsymbol{y})\right] - 1\right\}\delta_{\alpha\beta} \equiv \left[S(\boldsymbol{x},\boldsymbol{y}) - 1\right]\delta_{\alpha\beta}, \tag{4.10}$$

where we identify the S-matrix for the elastic scattering of a color dipole, $S(\boldsymbol{x},\boldsymbol{y})$. Now we are able to write the complete $q\bar{q}$ component of the diffractive scattering amplitude of the (transverse) virtual photon LCWF off a nuclear target,

$$\begin{aligned}\left|\gamma_T^i(q)\right\rangle^{\mathrm{D}}_{q\bar{q}} = \sum_{\lambda_{1,2}=\pm 1/2}\sum_{\alpha,\beta=1}^{N_c}\delta_{\alpha\beta}\int_0^1 \mathrm{d}\vartheta_1\mathrm{d}\vartheta_2\,\delta(1-\vartheta_1-\vartheta_2)\int \mathrm{d}^2\boldsymbol{x}\,\mathrm{d}^2\boldsymbol{y}\\ \times\,\widetilde{\psi}^i_{\lambda_1\lambda_2}(\vartheta_1,\boldsymbol{r})\left[S(\boldsymbol{x},\boldsymbol{y})-1\right]\left|q^\alpha_{\lambda_1}(\vartheta_1,\boldsymbol{x})\,\bar{q}^\beta_{\lambda_2}(\vartheta_2,\boldsymbol{y})\right\rangle,\end{aligned} \tag{4.11}$$

which in fact allows to determine the diffractive production of dijets by calculating the number of quarks and antiquarks in the final state. Hence, to calculate the corresponding cross section we must average over the quark and antiquark number operators $\hat{N}_q(k_1)$ and $\hat{N}_{\bar{q}}(k_2)$, namely,

$$\frac{\mathrm{d}\sigma^{\gamma_T^* A\to q\bar{q}X}_{\mathrm{D_{tot}}}}{\mathrm{d}k_1^+\mathrm{d}k_2^+\mathrm{d}^2\boldsymbol{k}_1\mathrm{d}^2\boldsymbol{k}_2}\,(2\pi)\,\delta(q^+-k_1^+-k_2^+) = \frac{1}{2}\,{}^{\mathrm{D}}_{q\bar{q}}\!\left\langle\gamma_T^i(q)\right|\hat{N}_q(k_1)\,\hat{N}_{\bar{q}}(k_2)\left|\gamma_T^i(q)\right\rangle^{\mathrm{D}}_{q\bar{q}}, \tag{4.12}$$

where the factor $1/2$ comes from the average over the 2 transverse polarizations. The δ-function factorized in the l.h.s. of Eq. (4.12) enforcing the plus longitudinal momentum conservation is a consequence of the dot product of the partonic states considered in the r.h.s. of the same equation. This arises from the (anti)commutation relations of the ladder operators involved in the quantization of the gauge field, see e.g. Appendix B in [110]. In fact, in constructing the cross section, we follow the conventions in [110] (see also [35]) for the normalization of the number operators, leading to

$$\begin{aligned}\frac{\mathrm{d}\sigma^{\gamma_T^* A\to q\bar{q}X}_{\mathrm{D_{tot}}}}{\mathrm{d}\vartheta_1\mathrm{d}\vartheta_2\,\mathrm{d}^2\boldsymbol{k}_1\mathrm{d}^2\boldsymbol{k}_2} = \frac{\alpha_{\mathrm{em}}\,N_c}{2\pi^2}\left(\sum e_f^2\right)\delta(1-\vartheta_1-\vartheta_2)\left(\vartheta_1^2+\vartheta_2^2\right)\int\frac{\mathrm{d}^2\boldsymbol{x}}{2\pi}\,\frac{\mathrm{d}^2\boldsymbol{y}}{2\pi}\,\frac{\mathrm{d}^2\bar{\boldsymbol{x}}}{2\pi}\,\frac{\mathrm{d}^2\bar{\boldsymbol{y}}}{2\pi}\\ \times\,e^{-i\boldsymbol{k}_1\cdot(\boldsymbol{x}-\bar{\boldsymbol{x}})-i\boldsymbol{k}_2\cdot(\boldsymbol{y}-\bar{\boldsymbol{y}})}\,\frac{\boldsymbol{r}\cdot\bar{\boldsymbol{r}}}{r\bar{r}}\,\bar{Q}^2K_1(\bar{Q}r)K_1(\bar{Q}\bar{r})\left\langle[S(\boldsymbol{x},\boldsymbol{y})-1][S(\bar{\boldsymbol{y}},\bar{\boldsymbol{x}})-1]\right\rangle,\end{aligned} \tag{4.13}$$

where again the barred coordinates belong to the complex conjugate amplitude and $\alpha_{\mathrm{em}} = e^2/4\pi$.

The brackets in the last factor in Eq. (4.13) account for the average over all possible target field configurations, and we shall take it in the framework of the CGC. At moderate rapidities we use the MV model introduced in Chapter 2 (see Eq. (2.48)), while, to evolve to higher rapidities we rely on the solution of the collBK given in Sect. 2.2.2. The rapidity gap is determined by the kinematics and in order to understand its precise allowed values, it is convenient to make a change of variables.

In the DA (and analogously in the CCA) in the coordinate space we replace the transverse positions $\boldsymbol{x}$ and $\boldsymbol{y}$ by the dipole transverse separation $\boldsymbol{r}$ and the center of energy (or impact parameter) $\boldsymbol{b}$ which can be defined as

$$\boldsymbol{b} \equiv \vartheta_1\boldsymbol{x} + \vartheta_2\boldsymbol{y}, \tag{4.14}$$

So, it follows that $\boldsymbol{x} = \boldsymbol{b} + \vartheta_2 \boldsymbol{r}$ and $\boldsymbol{y} = \boldsymbol{b} - \vartheta_1 \boldsymbol{r}$. In momentum space, we replace the transverse momenta $\boldsymbol{k}_1$ and $\boldsymbol{k}_2$ with the relative momentum $\boldsymbol{P}$ and the dijet imbalance $\boldsymbol{\Delta}$,

$$\boldsymbol{P} \equiv \vartheta_2 \boldsymbol{k}_1 - \vartheta_1 \boldsymbol{k}_2, \qquad \boldsymbol{\Delta} = \boldsymbol{k}_1 + \boldsymbol{k}_2, \tag{4.15}$$

which are equivalent to the relations $\boldsymbol{k}_1 = \boldsymbol{P} + \vartheta_1 \boldsymbol{\Delta}$ and $\boldsymbol{k}_2 = -\boldsymbol{P} + \vartheta_2 \boldsymbol{\Delta}$. Then, by a simple inspection, we find that the phase in the Fourier transform in Eq. (4.13) can be rewritten as

$$\boldsymbol{k}_1 \cdot (\boldsymbol{x} - \bar{\boldsymbol{x}}) + \boldsymbol{k}_2 \cdot (\boldsymbol{y} - \bar{\boldsymbol{y}}) = \boldsymbol{P} \cdot (\boldsymbol{r} - \bar{\boldsymbol{r}}) + \boldsymbol{\Delta} \cdot (\boldsymbol{b} - \bar{\boldsymbol{b}}). \tag{4.16}$$

We consider a homogeneous nucleus, so the CGC correlators depend only on the differences between any pair of transverse coordinates. In the present process, the correlator in the last factor of Eq. (4.13) can depend only on three vectors, which we conveniently choose[1] to be $\boldsymbol{r}$, $\bar{\boldsymbol{r}}$, and the difference between the impact parameters in the DA and the CCA, $\boldsymbol{B} \equiv \boldsymbol{b} - \bar{\boldsymbol{b}}$, see the phase Eq. (4.16). We immediately observe that this implies that one of the two center-of-energy vector integrations leads to the total transverse area of the nucleus, $S_\perp$.

It is also important to note that Eq. (4.16) and our choice of independent coordinate vectors imply that the hard scale $P_\perp$ controls the individual sizes r and $\bar{r}$, while the semi-hard momentum $\Delta_\perp$ controls the separation between the dipoles in the DA and the CCA. In the correlation limit, this implies that in coordinate space we have the condition $r, \bar{r} \ll B, 1/Q_s$.

Finally, as we are interested in the incoherent diffractive cross section, we must subtract the piece of the correlator averaged at the amplitude level. Thus, the cross section of interest in the transverse sector can be written as [34].

$$\begin{aligned}\frac{\mathrm{d}\sigma_{\mathrm{D}}^{\gamma_T^* A \to q\bar{q}X}}{\mathrm{d}\vartheta_1 \mathrm{d}\vartheta_2\, \mathrm{d}^2\boldsymbol{P} \mathrm{d}^2\boldsymbol{\Delta}} &= \frac{S_\perp \alpha_{\mathrm{em}} N_c}{4\pi^3} \left(\sum e_f^2\right) \delta(1 - \vartheta_1 - \vartheta_2) \left(\vartheta_1^2 + \vartheta_2^2\right) \int \frac{\mathrm{d}^2\boldsymbol{B}}{2\pi} \frac{\mathrm{d}^2\boldsymbol{r}}{2\pi} \frac{\mathrm{d}^2\bar{\boldsymbol{r}}}{2\pi} \\ &\times e^{-i\boldsymbol{\Delta}\cdot\boldsymbol{B} - i\boldsymbol{P}\cdot(\boldsymbol{r} - \bar{\boldsymbol{r}})} \frac{\boldsymbol{r}\cdot\bar{\boldsymbol{r}}}{r\bar{r}} \bar{Q}^2 K_1(\bar{Q}r) K_1(\bar{Q}\bar{r}) \mathcal{W}_q(\boldsymbol{r}, \bar{\boldsymbol{r}}, \boldsymbol{B}),\end{aligned} \tag{4.17}$$

where

$$\mathcal{W}_q(\boldsymbol{r}, \bar{\boldsymbol{r}}, \boldsymbol{B}) = \langle S(\boldsymbol{x}, \boldsymbol{y}) S(\bar{\boldsymbol{y}}, \bar{\boldsymbol{x}}) \rangle - \langle S(\boldsymbol{x}, \boldsymbol{y}) \rangle \langle S(\bar{\boldsymbol{y}}, \bar{\boldsymbol{x}}) \rangle\,. \tag{4.18}$$

is the diffractive correlator defined in Eq. (3.9) in its fundamental representation, and it contains all the QCD dynamics within the CGC framework. This correlator must be evaluated at the rapidity gap of the diffractive process, which is determined by $Y_{\mathbb{P}} = \ln 1/x_{\mathbb{P}}$, as discussed at the end of section 3.1.1. The conservation of minus longitudinal momentum for the process $\gamma^* \mathbb{P} \to q\bar{q}$ leads to the relation

$$x_{\mathbb{P}} P_N^- = \frac{1}{2q^+} \left(\frac{k_{1\perp}^2}{\vartheta_1} + \frac{k_{2\perp}^2}{\vartheta_2} + Q^2 \right). \tag{4.19}$$

By using the definition of x_{Bj} in Eq. (1.12) and changing the transverse variables from $k_{1\perp}$ and $k_{2\perp}$ to $P_\perp$ and $\Delta_\perp$, we find that

$$x_{\mathbb{P}} = x_{\mathrm{Bj}} \left(1 + \frac{P_\perp^2}{\bar{Q}^2} + \frac{\Delta_\perp^2}{Q^2} \right). \tag{4.20}$$

In the kinematic regime of interest, we have the hierarchy $\bar{Q} \sim k_{1\perp} \sim k_{2\perp} \gg \Delta_\perp$, which, in terms of the relative and transfer momentum, is given by $P_\perp \sim \bar{Q} \gg \Delta_\perp$. This means that the

[1] Although other choices can be considered, the one used here allows us to directly relate the size of the dipoles under consideration (see also Sect. 4.2) with the momentum scales of the correlation limit.

term $\Delta_\perp^2/\bar{Q}^2 \ll 1$ can be neglected, while $P_\perp^2/\bar{Q}^2$ is of order one. Therefore, the rapidity gap can be written as

$$Y_{\mathbb{P}} \simeq \ln \frac{1}{x_{\rm Bj}} - \ln\left(1 + \frac{P_\perp^2}{\bar{Q}^2}\right). \tag{4.21}$$

From the last equation, it can be inferred that the production of the dijet takes up roughly one unit of the available longitudinal phase space. Since $x_{\rm Bj} \ll 1$, the first term dominates at the leading logarithmic level, and the second term can be neglected. This also implies that we can assume that the gap is independent of $P_\perp$, although keeping the second term in the evaluation of the correlators is not a significant issue.

In Eq. (4.21), it is also clear that to maximize the rapidity gap, the most interesting scenario involves longitudinal fractions, ϑ_1 and ϑ_2, that are roughly equal. This leads us to express the cross sections per unit of longitudinal momentum, as given in Eq. (4.17), rather than in terms of rapidities. To convert from the latter to the former, it suffices to multiply by a factor of $\vartheta_1\vartheta_2$. Since the longitudinal fractions are of order one-half, the dependence on this factor can be neglected.

To conclude this section, we briefly describe the corresponding expression for a longitudinally polarized virtual photon. It suffices to make the replacements $\vartheta_1^2 + \vartheta_2^2 \to 4\vartheta_1\vartheta_2$ and $(\boldsymbol{r}/r)K_1(\bar{Q}r) \to K_0(\bar{Q}r)$ in the DA (and similarly in the CCA) in Eq. (4.17).

4.2 The fundamental correlator in the correlation limit

This section focuses on computing the connected part of the average of the product of two dipole S-matrices in the fundamental representation, for an arbitrary number of colors N_c, to the lowest order in the dipole sizes r and $\bar{r}$. As discussed bellow Eq. (4.16), in the correlation limit we assume that $r, \bar{r} \ll B, 1/Q_s$, with no specific constraint between the sizes B and $1/Q_s$. As mentioned earlier, we work within the Gaussian approximation and assume that the averaged dipole S-matrices depend only on the magnitude of the dipole separation, i.e., $\mathcal{S}(\boldsymbol{x},\boldsymbol{y}) = \mathcal{S}(|\boldsymbol{x}-\boldsymbol{y}|)$. Therefore, the exact double dipole correlator in the Gaussian approximation for a homogeneous nucleus can then be written as [111]

$$\begin{aligned}\langle S(\boldsymbol{x},\boldsymbol{y}) S(\bar{\boldsymbol{y}},\bar{\boldsymbol{x}})\rangle =& \,\mathcal{S}(\boldsymbol{x},\boldsymbol{y})\, \mathcal{S}(\bar{\boldsymbol{y}},\bar{\boldsymbol{x}})\, e^{-\frac{F}{2}+\frac{f}{N_c^2}} \\ &\times \left[\left(\frac{\sqrt{D}+F}{2\sqrt{D}} - \frac{f}{N_c^2\sqrt{D}}\right) e^{\frac{\sqrt{D}}{2}} + \left(\frac{\sqrt{D}-F}{2\sqrt{D}} + \frac{f}{N_c^2\sqrt{D}}\right) e^{-\frac{\sqrt{D}}{2}}\right],\end{aligned} \tag{4.22}$$

where we use the definitions

$$D = F^2 - \frac{4}{N_c^2} f(F-f), \quad F = \frac{N_c}{2C_F} \ln \frac{\mathcal{S}(\boldsymbol{x},\boldsymbol{y})\,\mathcal{S}(\bar{\boldsymbol{y}},\bar{\boldsymbol{x}})}{\mathcal{S}(\boldsymbol{x},\bar{\boldsymbol{x}})\,\mathcal{S}(\boldsymbol{y},\bar{\boldsymbol{y}})} \quad \text{and} \quad f = \frac{N_c}{2C_F} \ln \frac{\mathcal{S}(\boldsymbol{x},\bar{\boldsymbol{y}})\,\mathcal{S}(\boldsymbol{y},\bar{\boldsymbol{x}})}{\mathcal{S}(\boldsymbol{x},\bar{\boldsymbol{x}})\,\mathcal{S}(\boldsymbol{y},\bar{\boldsymbol{y}})}. \tag{4.23}$$

We observe in these expressions that the lowest order term in r and $\bar{r}$ is obtained by expanding the logarithms of the S-matrices. To achieve this, we note that from Eq. (4.14) and the relations below that $\boldsymbol{x} - \bar{\boldsymbol{y}} = \boldsymbol{B} + \vartheta_2\boldsymbol{r} + \vartheta_1\bar{\boldsymbol{r}}$. Therefore, we can write

$$\ln \mathcal{S}(\boldsymbol{x},\bar{\boldsymbol{y}}) \simeq \ln \mathcal{S}(B) + (\vartheta_2 r + \vartheta_1 \bar{r})^i \partial^i \ln \mathcal{S}(B) + \frac{1}{2}\,(\vartheta_2 r + \vartheta_1 \bar{r})^i (\vartheta_2 r + \vartheta_1 \bar{r})^j \partial^i\partial^j \ln \mathcal{S}(B), \tag{4.24}$$

and similarly for the other three dipole correlators appearing in the argument of the logarithm in f. The leading terms cancel because they all involve one position in the DA and the other in the CCA. It can also be explicitly checked, as discussed above Eq. (3.15), that the linear terms in dipole size also cancel. Then, the second-order terms can be combined to yield

$$f \simeq \frac{N_c}{2C_F}\, r^i \bar{r}^j\, \partial^i \partial^j \ln \mathcal{S}(B) = \frac{1}{2}\, r^i \bar{r}^j\, \partial^i \partial^j \ln \mathcal{S}_g(B). \tag{4.25}$$

In the second equality, we use the adjoint dipole S-matrix $\mathcal{S}_g(B)$, as defined in Eq. (2.50), within the Gaussian approximation. We also note the similarity between Eq. (4.25) and Eq. (3.15), and we can consider the former as a generalization of the latter. On the other hand, the leading term in F is independent of the dipole sizes r and $\bar{r}$, and can be written as

$$F \simeq -\frac{N_c}{2C_F} \ln \mathcal{S}^2(B) = -\ln \mathcal{S}_g(B). \tag{4.26}$$

The limiting behavior of Eq. (4.25) and Eq. (4.26) allows us to expand $\sqrt{D}$ in orders of f, so at second order it reads

$$\sqrt{D} \simeq F - \frac{2f}{N_c^2} + \frac{4C_F f^2}{N_c^3 F}. \tag{4.27}$$

By the same argument the various factors in Eq. (4.22) can be expanded for small values of f. The linear terms cancel, while the quadratic ones give the relation

$$\langle S(\boldsymbol{x},\boldsymbol{y}) S(\bar{\boldsymbol{y}},\bar{\boldsymbol{x}})\rangle \simeq \mathcal{S}(\boldsymbol{x},\boldsymbol{y})\, \mathcal{S}(\bar{\boldsymbol{y}},\bar{\boldsymbol{x}}) \left[1 + \frac{2C_F}{N_c^3}\, f^2 \frac{e^{-F} - 1 + F}{F^2}\right]. \tag{4.28}$$

We see that the second term, which in fact correspond to the incoherent component, is already quartic in the sizes r and $\bar{r}$, meaning that even when taking higher order values of F in Eq. (4.26), their contribution would be neglected in the double dipole correlator. When $B \ll 1/Q_s$, F is small and the F-dependent fraction in the second term in the square bracket in Eq. (4.28) becomes 1/2. Eventually, Eq. (4.28) reduces to Eq. (3.16) as it should. It is also important to point out that at large-N_c, Eq. (4.22) reduces to Eq. (4.28) [2] (clearly with $2C_F/N_c^3 \to 1/N_c^2$) for generic dipole sizes r and $\bar{r}$.

By subtracting the $\mathcal{S}(\boldsymbol{x},\boldsymbol{y})\, \mathcal{S}(\bar{\boldsymbol{y}},\bar{\boldsymbol{x}})$ component in Eq. (4.28), the incoherent diffractive correlator in terms of dipole sizes in the correlation limit can be then written as

$$\mathcal{W}_q(\boldsymbol{r},\bar{\boldsymbol{r}},\boldsymbol{B}) \simeq \frac{2C_F}{N_c^3}\, f^2 \mathcal{S}(r)\, \mathcal{S}(\bar{r}) \frac{e^{-F} - 1 + F}{F^2}. \tag{4.29}$$

Finally, to the order of accuracy, $\mathcal{S}(\boldsymbol{x},\boldsymbol{y})\, \mathcal{S}(\bar{\boldsymbol{y}},\bar{\boldsymbol{x}})$ can be set equal to unity in Eq. (4.29), and by using Eqs. (4.25) and (4.26), the correlator in terms of $\mathcal{S}_g$ takes the form

$$\mathcal{W}_q(\boldsymbol{r},\bar{\boldsymbol{r}},\boldsymbol{B}) \simeq \frac{C_F}{2N_c^3}\, r^i \bar{r}^j r^k \bar{r}^l\, \Phi(B)\, [\partial^i \partial^j \ln \mathcal{S}_g(B)]\, [\partial^k \partial^l \ln \mathcal{S}_g(B)], \tag{4.30}$$

[2] As argued in Chapter 3, the N_c-suppressed terms are essential in the study of incoherent diffraction. At the same time, it is evident from the squared bracket in Eq. (4.28) that these terms allow to perform the replacement $\langle S(\boldsymbol{y},\boldsymbol{z}) S(\boldsymbol{y},\boldsymbol{z})\rangle \to \langle S(\boldsymbol{y},\boldsymbol{z})\rangle\langle S(\boldsymbol{y},\boldsymbol{z})\rangle$ in the BK evolution equation (cf. Eq. (2.44) and bellow). It can be shown numerically that the evolution of the n-point Wilson-line correlators in the Gaussian approximation at large-N_c closely approximates the exact JIMWLK evolution equation [112]. This justifies neglecting the N_c-suppressed terms in the small-x evolution of dipole scattering amplitudes and allows us to use the collBK evolution equation in the present work.

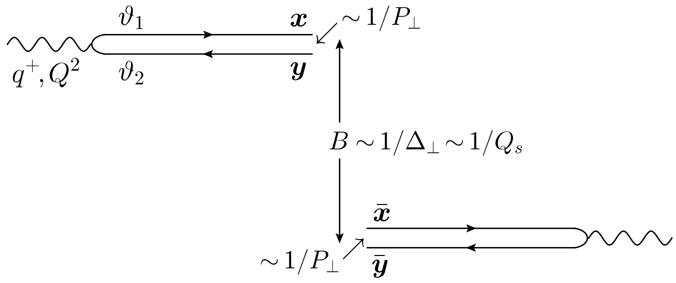

Figure 4.3: The typical dipole configuration that determines the incoherent diffractive dijet cross section in Eq. (4.17) in the most interesting kinematic regime, $P_\perp \gg \Delta_\perp \sim Q_s$, which is a subspace of the regime defined by the correlation limit $P_\perp \gg \Delta_\perp, Q_s$. In this configuration, the $q\bar{q}$ dipole in the DA is separated from the one in the CCA by a large distance, $B \sim 1/\Delta_\perp \sim 1/Q_s$, compared to the dipole sizes themselves, which satisfy $r, \bar{r} \sim 1/P_\perp \ll 1/Q_s$.

where we defined the dimensional scalar

$$\Phi(B) \equiv \frac{\mathcal{S}_g(B) - 1 - \ln \mathcal{S}_g(B)}{\ln^2 \mathcal{S}_g(B)}, \tag{4.31}$$

to compact the expression. Eq. (4.30) generalizes Eq. (3.16) for arbitrary values of B, so that the conjugate momentum $\Delta_\perp$ can be of the order of (or smaller than) Q_s. This implies that the correlator includes unitarity corrections for the associated scattering amplitude.

Notably, in Eq. (4.30), there is an angular correlation between $\boldsymbol{r}$ (and $\bar{\boldsymbol{r}}$) and $\boldsymbol{B}$, which in momentum space corresponds to an angular correlation between $\boldsymbol{P}$ and $\boldsymbol{\Delta}$. The tensorial factorization, dictated by the size scales at the level of the diffractive correlator in the correlation limit, is explicit in Eq. (4.30). In other words, the power-law dependence on the small fundamental dipole sizes $\boldsymbol{r}$ and $\bar{\boldsymbol{r}}$ factorizes from the dependence on the large adjoint dipole $\boldsymbol{B}$.

In the next section, we will present the analogous factorized cross sections, expressed in terms of their related hard and semihard momenta, along with their non-trivial dependence on $\mathcal{S}_g(B)$. The appearance of the adjoint dipole is a consequence of the participation of double dipoles, which can be seen in Fig. 4.3, where the dipole configuration for the incoherent diffractive process in the kinematic regime of interest is shown.

4.3 The factorized cross sections

The form of the fundamental correlator in Eq. (4.30) allows the factorization of the integrals over $\boldsymbol{r}$ and $\bar{\boldsymbol{r}}$ from the one over $\boldsymbol{B}$ in Eq. (4.17), leading to the form

$$\frac{\mathrm{d}\sigma_{\mathrm{D}}^{\gamma_T^* A \to q\bar{q}X}}{\mathrm{d}\vartheta_1 \mathrm{d}\vartheta_2\, \mathrm{d}^2\boldsymbol{P} \mathrm{d}^2\boldsymbol{\Delta}} = \frac{S_\perp \alpha_{\mathrm{em}}\, N_c}{4\pi^3} \left(\sum e_f^2\right) \delta(1 - \vartheta_1 - \vartheta_2) \left(\vartheta_1^2 + \vartheta_2^2\right) \frac{C_F}{2N_c^3} \left|\mathcal{A}_{\mathrm{D}}^T\right|^2, \tag{4.32}$$

where the "reduced" cross section $\left|\mathcal{A}_{\mathrm{D}}^T\right|^2$ is defined as

$$\left|\mathcal{A}_{\mathrm{D}}^T\right|^2 = H_T^{iks}(\boldsymbol{P}, \bar{Q})\, H_T^{jls*}(\boldsymbol{P}, \bar{Q})\, \mathcal{G}_{\mathrm{D}}^{ij,kl}(\boldsymbol{\Delta}), \tag{4.33}$$

and where the hard factor H_T^{iks} is given by the rank-3 tensor

$$H_T^{iks}(\boldsymbol{P}, \bar{Q}) = \int \frac{\mathrm{d}^2\boldsymbol{r}}{2\pi}\, e^{-i\boldsymbol{P}\cdot\boldsymbol{r}}\, \frac{r^i r^k r^s}{r}\, \bar{Q} K_1\big(\bar{Q} r\big), \tag{4.34}$$

while the semihard factor $\mathcal{G}_{\mathrm{D}}^{ij,kl}(\boldsymbol{\Delta})$ reads

$$\mathcal{G}_{\mathrm{D}}^{ij,kl}(\boldsymbol{\Delta}) = \int \frac{\mathrm{d}^2\boldsymbol{B}}{2\pi}\, e^{-i\boldsymbol{\Delta}\cdot\boldsymbol{B}}\, \Phi(B)\, [\partial^i\partial^j \ln \mathcal{S}_g(B)]\, [\partial^k\partial^l \ln \mathcal{S}_g(B)], \tag{4.35}$$

with the scalar function $\Phi(B)$ being defined in Eq. (4.31). This central result of our work shows that at leading twist (in reference to the inverse powers of $P_\perp$), the cross section for incoherent diffractive dijet production can be given in a factorized form at the tensorial level: one factor depends only on the hard momenta $\boldsymbol{P}$ and $\bar{Q}$, while another depends solely on the semi-hard momentum $\boldsymbol{\Delta}$.

It is also clear that this result includes all the inverse powers of the imbalance $\Delta_\perp$. A similar property was found in the case of the inclusive dijet cross section [27, 113].

Notably, in contrast to the coherent case, where the imbalance momentum is generated by the emission of a gluon [52, 53, 55], this factorization does not hold at the level of the amplitude.

The hard factor Eq. (4.34) is symmetric in all indices, and as a result, the integration can be written in terms of $\delta^{ik}P^s$, $P^iP^kP^s$, and their permutations, all with the same weight. Thus, by performing the decomposition in terms of two independent scalars, it can be expressed as

$$H_T^{iks}(\boldsymbol{P},\bar{Q}) = -\frac{2i}{(P_\perp^2+\bar{Q}^2)^2}\left(\delta^{ik}P^s + \delta^{is}P^k + \delta^{ks}P^i\right) + \frac{8iP^iP^kP^s}{(P_\perp^2+\bar{Q}^2)^3}. \tag{4.36}$$

The semi-hard factor $\mathcal{G}_{\mathrm{D}}^{ij,kl}(\boldsymbol{\Delta})$ in Eq. (4.33) incorporates the QCD dynamics through the non-linear scattering of the adjoint dipole off the nuclear target. Its tensorial structure consists of two factors, each of which is a symmetric rank-two tensor of the form $\partial^i\partial^j \ln \mathcal{S}_g(B)$. Since we assume that $\mathcal{S}_g$ depends only on the magnitude of $\boldsymbol{B}$, these factors can be decomposed into diagonal and traceless parts, which read

$$\partial^i\partial^j \ln \mathcal{S}_g(B) = F_+(B)\,\frac{\delta^{ij}}{2} + F_-(B)\,\hat{B}^{ij}, \tag{4.37}$$

where the scalar coefficients $F_+(B)$ and $F_-(B)$ are found to be

$$F_\pm(B) = \frac{\partial^2 \ln \mathcal{S}_g(B)}{\partial B^2} \pm \frac{1}{B}\,\frac{\partial \ln \mathcal{S}_g(B)}{\partial B} \tag{4.38}$$

and where we have defined the traceless tensor

$$\hat{B}^{ij} \equiv \left(\frac{B^iB^j}{B^2} - \frac{\delta^{ij}}{2}\right). \tag{4.39}$$

The two functions in Eq. (4.38) have dimensions of mass squared, and we note that $F_+(B) = \nabla^2 \ln \mathcal{S}_g(B)$. Hence, the rank-4 tensor $\mathcal{G}_{\mathrm{D}}^{ij,kl}(\boldsymbol{\Delta})$ can be decomposed in terms of the structures $\delta^{ij}\delta^{kl}$, $\delta^{ij}\Delta^k\Delta^l$, $\Delta^i\Delta^j\Delta^k\Delta^l$, or permutations of the first two. The precise form of the tensor, along with its corresponding scalar coefficients, is given in Appendix B, see Eqs. (B.1)-(B.7). Here, we rewrite only the coefficients that contribute to the cross section of the process under consideration, which are

$$\mathcal{G}_{\mathrm{D}}^{(+)}(\Delta_\perp) = \int \frac{\mathrm{d}^2\boldsymbol{B}}{2\pi}\, e^{-i\boldsymbol{\Delta}\cdot\boldsymbol{B}}\, \Phi(B)[F_+(B)]^2, \tag{4.40}$$

$$\mathcal{G}_{\mathrm{D}}^{(-)}(\Delta_\perp) = \int \frac{\mathrm{d}^2\boldsymbol{B}}{2\pi}\, e^{-i\boldsymbol{\Delta}\cdot\boldsymbol{B}}\, \Phi(B)[F_-(B)]^2, \tag{4.41}$$

$$\mathcal{G}_{\mathrm{D}}^{(1)}(\Delta_\perp) = \int \frac{\mathrm{d}^2\boldsymbol{B}}{2\pi}\, e^{-i\boldsymbol{\Delta}\cdot\boldsymbol{B}}\, \Phi(B) F_+(B) F_-(B) \cos 2\phi_{\Delta B} \tag{4.42}$$

and

$$\mathcal{G}_{\mathrm{D}}^{(2)}(\Delta_\perp) = \int \frac{\mathrm{d}^2\boldsymbol{B}}{2\pi}\, e^{-i\boldsymbol{\Delta}\cdot\boldsymbol{B}}\, \Phi(B) [F_-(B)]^2 \cos 4\phi_{\Delta B}, \tag{4.43}$$

with $\phi_{\Delta B}$ being the angle between the vectors $\boldsymbol{\Delta}$ and $\boldsymbol{B}$. We will refer to these quantities as semihard coefficients[3] and observe that the integration over the angle $\phi_{\Delta B}$ in these terms can be performed using the relation

$$\int \frac{\mathrm{d}^2\boldsymbol{B}}{2\pi}\, e^{-i\boldsymbol{\Delta}\cdot\boldsymbol{B}}\, \mathcal{F}(B) \cos 2n\phi_{\Delta B} = (-1)^n \int_0^\infty \mathrm{d}B\, B J_n(\Delta_\perp B) \mathcal{F}(B), \tag{4.44}$$

where $\mathcal{F}(B)$ is an arbitrary function of B, representing all possible semihard coefficients in terms of one-dimensional integrals involving the first three even Bessel functions of the first kind, i.e., $J_n(\Delta_\perp B)$ with $n = 0, 2, 4$.

Now that we have suitable expressions for the tensors involving the hard and semihard factors of the cross section, we can perform the corresponding contractions to obtain the transverse reduced cross section, which is given by

$$\begin{aligned} \left|\mathcal{A}_{\mathrm{D}}^T\right|^2 = {} & \frac{4P_\perp^2(3\bar{Q}^4 + P_\perp^4)}{(P_\perp^2 + \bar{Q}^2)^6}\, \mathcal{G}_{\mathrm{D}}^{(+)}(\Delta_\perp) + \frac{8\bar{Q}^4 P_\perp^2}{(P_\perp^2 + \bar{Q}^2)^6}\, \mathcal{G}_{\mathrm{D}}^{(-)}(\Delta_\perp) \\ & + \frac{16\bar{Q}^2 P_\perp^2(\bar{Q}^2 - P_\perp^2)\cos 2\phi}{(P_\perp^2 + \bar{Q}^2)^6}\, \mathcal{G}_{\mathrm{D}}^{(1)}(\Delta_\perp) - \frac{8\bar{Q}^2 P_\perp^4 \cos 4\phi}{(P_\perp^2 + \bar{Q}^2)^6}\, \mathcal{G}_{\mathrm{D}}^{(2)}(\Delta_\perp), \end{aligned} \tag{4.45}$$

where ϕ is the angle between the hard jet momentum $\boldsymbol{P}$ and the momentum transfer $\boldsymbol{\Delta}$.

The longitudinal cross section, as discussed at the end of section 4.1, differs from the transverse one by replacing factors involving the longitudinal fractions and Bessel functions of the second kind. These replacements affect only the hard factor, resulting in the reduced cross section

$$\left|\mathcal{A}_{\mathrm{D}}^L\right|^2 = H_L^{ik}(\boldsymbol{P}, \bar{Q})\, H_L^{jl}(\boldsymbol{P}, \bar{Q})\, \mathcal{G}_{\mathrm{D}}^{ij,kl}(\boldsymbol{\Delta}), \tag{4.46}$$

where now the hard factor is encoded in the rank-2 tensor

$$\begin{aligned} H_L^{ik}(\boldsymbol{P}, \bar{Q}) &= \int \frac{\mathrm{d}^2\boldsymbol{r}}{2\pi}\, e^{-i\boldsymbol{P}\cdot\boldsymbol{r}}\, r^i r^k\, \bar{Q} K_0(\bar{Q}r) \\ &= \frac{4\bar{Q}(\bar{Q}^2 - P_\perp^2)}{(P_\perp^2 + \bar{Q}^2)^3} \frac{\delta^{ik}}{2} - \frac{8\bar{Q}P_\perp^2}{(P_\perp^2 + \bar{Q}^2)^3} \left(\frac{P^i P^k}{P_\perp^2} - \frac{\delta^{ik}}{2} \right). \end{aligned} \tag{4.47}$$

The contractions with the semihard factor lead to

$$\begin{aligned} \left|\mathcal{A}_{\mathrm{D}}^L\right|^2 = {} & \frac{2\bar{Q}^2(\bar{Q}^4 - 2\bar{Q}^2 P_\perp^2 + 5P_\perp^4)}{(P_\perp^2 + \bar{Q}^2)^6}\, \mathcal{G}_{\mathrm{D}}^{(+)}(\Delta_\perp) + \frac{2\bar{Q}^2(\bar{Q}^2 - P_\perp^2)^2}{(P_\perp^2 + \bar{Q}^2)^6}\, \mathcal{G}_{\mathrm{D}}^{(-)}(\Delta_\perp) \\ & - \frac{16\bar{Q}^2 P_\perp^2(\bar{Q}^2 - P_\perp^2)\cos 2\phi}{(P_\perp^2 + \bar{Q}^2)^6}\, \mathcal{G}_{\mathrm{D}}^{(1)}(\Delta_\perp) + \frac{8\bar{Q}^2 P_\perp^4 \cos 4\phi}{(P_\perp^2 + \bar{Q}^2)^6}\, \mathcal{G}_{\mathrm{D}}^{(2)}(\Delta_\perp). \end{aligned} \tag{4.48}$$

[3]This differs from the original paper [63], where they were abusively called semihard *distributions* due to their similarity to the gluon distributions in inclusive dijet production [26, 27, 113]. See the discussion below Eq. (4.11) in [63] and Appendix C in this work. We do not use the same terminology here to avoid confusion with the parton distributions introduced in [64], which will be presented in Chapter 6.

Just as in the case of the transverse cross section, the longitudinal component is expressed as a linear combination of four semihard coefficients, $\mathcal{G}_{\mathrm{D}}^{(n)}(\Delta_\perp)$, with the indices $n = +, -, 1, 2$, which correspond to $0, 0, 2, 4$ in their angular dependence, $\cos n\phi_{\Delta B}$. Each term is given by analytical expressions depending on the hard momenta $P_\perp$ and $\bar{Q}$, as well as on the angle between $\boldsymbol{P}$ and $\boldsymbol{\Delta}$. We note that there is a one-to-one correspondence between the angle $\phi_{\Delta B}$ and the angle ϕ; that is, each $\mathcal{G}_{\mathrm{D}}^{(n)}(\Delta_\perp)$ involves a $\cos n\phi_{\Delta B}$, which in turn leads to a $\cos n\phi$ dependence in the cross section. Additionally, we observe a flip of sign in the terms involving $\cos 2\phi$ and $\cos 4\phi$ between the transverse and longitudinal components. This characteristic is also observed in the inclusive dijet cross section for the coefficients of $\cos 2\phi$ [27].

Before proceeding with the analysis of the momentum dependence of the semihard coefficients $\mathcal{G}_{\mathrm{D}}^{(n)}(\Delta_\perp)$, we note that for the typical magnitude of jet momenta dictated by the photon decay vertex, $P_\perp \sim \bar{Q}$, the hard momentum factors in all terms scale as $1/P_\perp^6$. We also observe that in the limit $\bar{Q} \to 0$, which corresponds either to photo-production ($Q^2 \to 0$) or to the aligned aligned-jet limit ($\vartheta_1\vartheta_2 \to 0$), the longitudinal reduced cross section in Eq. (4.48) vanishes, while for the transverse case in Eq. (4.45), only the first term contributes.

4.4 The semihard momentum dependence

The $\Delta_\perp$-dependence is captured in the semihard factors $\mathcal{G}_{\mathrm{D}}^{(n)}(\Delta_\perp)$ in each term of both the transverse and longitudinal components. We begin by performing simple analytical calculations in different regimes, considering the momentum transfer $\Delta_\perp$ and the saturation momentum Q_s.

For moderate small values of x, we assume that the dipole-nucleus scattering is described by the MV model, which was introduced in Eq. (2.48) and is restated here for convenience in the form

$$\mathcal{S}_g(B) = 1 - \mathcal{T}_g(B) = \exp\left(-\frac{B^2 Q_A^2}{4} \ln \frac{4}{B^2\Lambda^2}\right), \tag{4.49}$$

with the scale Q_A^2 in terms of the saturation momentum given by the relation

$$Q_A^2 \ln \frac{Q_s^2}{\Lambda^2} = Q_s^2. \tag{4.50}$$

Such a relation refers to the gluon saturation momentum which is enhanced by a factor of N_c/C_F w.r.t. the quark one. Hence, the functions $F_+(B)$ and $F_-(B)$ are described by the simple expressions

$$F_+(B) = -Q_A^2 \ln\big(4/B^2\Lambda^2\big) + 2Q_A^2\,, \qquad F_-(B) = Q_A^2. \tag{4.51}$$

The dimensionless $\Phi(B)$, defined in Eq. (4.31), can be expressed in the piecewise form

$$\Phi(B) \simeq \begin{cases} 1/2 & \text{for} \quad B \ll 1/Q_s, \\ \mathcal{O}(1) & \text{for} \quad B \sim 1/Q_s, \\ -\dfrac{1}{\ln \mathcal{S}_g(B)} = \dfrac{4}{B^2 Q_A^2 \ln(4/B^2\Lambda^2)} & \text{for} \quad B \gg 1/Q_s, \end{cases} \tag{4.52}$$

We point out that the normalization is well-controlled when $B \ll 1/Q_s$, distinguishing it from the second case, although they are of the same order. In contrast, the third case, which corresponds to the regime where unitarity corrections are important with $\Delta_\perp \ll Q_s$, exhibits suppression for large values of B.

In the weak interaction regime, where $\Delta_\perp \gg Q_s$, the dominant contribution to the coefficients $\mathcal{G}_{\rm D}^{(n)}(\Delta_\perp)$ comes from small dipoles with $B \ll 1/Q_s$. By performing the integrations with the help of the integrals in Appendix A, we derive the expressions for the semihard coefficients to logarithmic accuracy, namely

$$\mathcal{G}_{\rm D}^{(+)} \simeq \frac{2Q_A^4}{\Delta_\perp^2}\ln\frac{\Delta_\perp^2}{\Lambda^2}, \quad \mathcal{G}_{\rm D}^{(-)} \simeq \frac{Q_A^6}{3\Delta_\perp^4}, \quad \mathcal{G}_{\rm D}^{(1)} \simeq \frac{Q_A^4}{\Delta_\perp^2}\ln\frac{\Delta_\perp^2}{\Lambda^2}, \quad \mathcal{G}_{\rm D}^{(2)} \simeq \frac{2Q_A^4}{\Delta_\perp^2} \quad \text{for} \quad \Delta_\perp \gg Q_s. \tag{4.53}$$

We see that the dominant contributions come from $\mathcal{G}_{\rm D}^{(+)}(\Delta_\perp)$ and $\mathcal{G}_{\rm D}^{(1)}(\Delta_\perp)$, and in this regime, they satisfy the relation $\mathcal{G}_{\rm D}^{(+)}(\Delta_\perp) \simeq 2\mathcal{G}_{\rm D}^{(1)}(\Delta_\perp)$. It is also evident that $\mathcal{G}_{\rm D}^{(-)}(\Delta_\perp)$ is power-suppressed.[4]

In the regime $\Delta_\perp \sim Q_s$, corresponding to dipole sizes $B \sim 1/Q_s$, we find

$$\mathcal{G}_{\rm D}^{(+)} \sim Q_s^2, \qquad \mathcal{G}_{\rm D}^{(-)} \sim \frac{Q_s^2}{\rho_A^2}, \qquad \mathcal{G}_{\rm D}^{(1)} \sim \frac{Q_s^2}{\rho_A}, \qquad \mathcal{G}_{\rm D}^{(2)} \sim \frac{Q_s^2}{\rho_A^2} \qquad \text{for} \quad \Delta_\perp \sim Q_s, \tag{4.54}$$

where we have defined $\rho_A \equiv \ln\big(Q_s^2/\Lambda^2\big)$. In this regime, $\mathcal{G}_{\rm D}^{(+)}(Q_s)$ also dominates with logarithmic accuracy. This same property holds in the regime of small momentum transfer, where $\Lambda \ll \Delta_\perp \ll Q_s$, in which case it behaves as

$$\mathcal{G}_{\rm D}^{(+)}(\Delta_\perp) \simeq Q_A^2\left(\ln^2\frac{Q_s^2}{\Lambda^2} - \ln^2\frac{\Delta_\perp^2}{\Lambda^2}\right) \qquad \text{for} \quad \Delta_\perp \ll Q_s, \tag{4.55}$$

thus, $\mathcal{G}_{\rm D}^{(+)}(\Delta_\perp)$ dominates across the entire kinematic regime and exhibits saturation. We also note that due to the dependence on the angle between $\boldsymbol{\Delta}$ and $\boldsymbol{B}$, the angular integration in $\mathcal{G}_{\rm D}^{(1)}(\Delta_\perp)$ and $\mathcal{G}_{\rm D}^{(2)}(\Delta_\perp)$ results in $J_2(\Delta_\perp B)$ and $J_4(\Delta_\perp B)$ for the corresponding semihard coefficients [cf. Eqs. (4.42), (4.43), and (4.44)]. These Bessel functions vanish quadratically and quartically, respectively, at small arguments, leading to the suppression of the coefficients in the region where $\Delta_\perp$ is smaller than Q_s.

The present work focuses on phenomenological applications, where the rapidity scale, at which the scattering amplitude must be evaluated, is of the order of a few units. In this context, the properties of the semihard $\mathcal{G}_{\rm D}^{(n)}(\Delta_\perp)$ are well described by the MV model. While detailed analytical estimates for high rapidities are possible, they are beyond the scope of this work. Nonetheless, for the sake of completeness, it is worth discussing the modifications that high-energy evolution, particularly the BK evolution, may bring to the estimates presented here. The BK evolution softens the perturbative tail of the scattering amplitude. At asymptotically high energies, the amplitude becomes a function of the single variable $BQ_s(Y)$, a property known as *geometrical scaling*, valid over a wide kinematic regime that extends to momenta well above Q_s [114–116]. Up to logarithmic factors, in the regime where $B \ll 1/Q_s$, the solution behaves as $\mathcal{T}_g(B) \propto (B^2Q_s^2)^\gamma$, where at LO, $\gamma \simeq 0.63$. At NLO, the corresponding corrections [98, 117, 118] and the necessary collinear resummations [99, 119, 120] ensure that this remains a good solution, with γ satisfying $1/2 < \gamma < 1$.

That said, we present the numerical evaluation of the semihard coefficients $\mathcal{G}_{\rm D}^{(n)}(\Delta_\perp)$ from Eqs. (4.40)-(4.43) in Fig. 4.4. In the left panel, we show the initial condition where the scattering

[4] To obtain this expression, it is necessary to retain the first subleading term $-\mathcal{T}_g/6$ in the expansion of Φ, where the amplitude $\mathcal{T}_g$ involves exchanges of only two gluons.

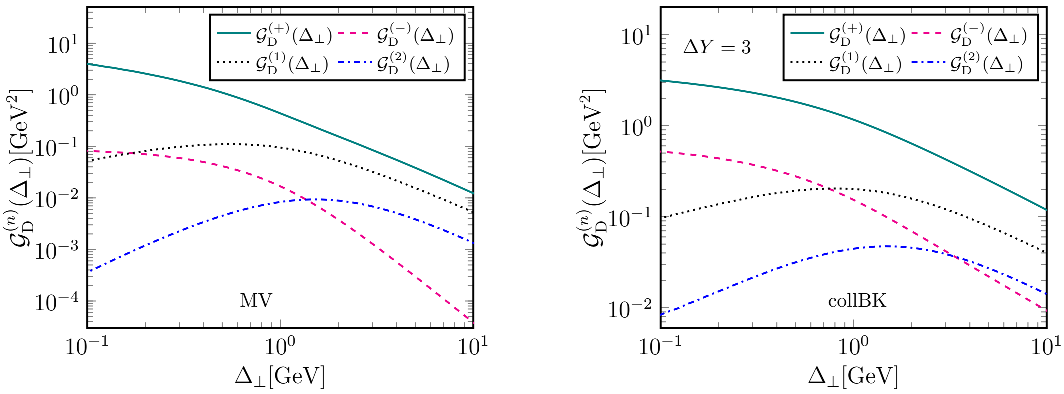

Figure 4.4: The four semihard functions $\mathcal{G}_{\rm D}^{(n)}(\Delta_\perp)$ as a function of the transverse momentum $\Delta_\perp$ are shown. Left panel: The input amplitude $\mathcal{T}_g(B)$ is taken from the MV model with $Q_s^2 = 2$ GeV^2. Right panel: The input amplitude $\mathcal{T}_g(B)$ is obtained by evolving the MV model initial condition to $\Delta Y = 3$ using the collinearly improved BK equation [99].

amplitude is given by the MV model, with $Q_s^2 = 2$ GeV^2. We confirm the hierarchies for $\Delta_\perp \gg Q_s$ and $\Delta_\perp \sim Q_s$ as outlined in Eqs. (4.53) and (4.54). It is also evident that $\mathcal{G}_{\rm D}^{(1)}(\Delta_\perp)$ and $\mathcal{G}_{\rm D}^{(2)}(\Delta_\perp)$ bend downward at small $\Delta_\perp$, as discussed below Eq. (4.55). Furthermore, we observe that $\mathcal{G}_{\rm D}^{(+)}(\Delta_\perp)$ grows logarithmically as $\Delta_\perp$ decreases; specifically, it grows as the square of the logarithm of $\Delta_\perp^2$, as dictated in Eq. (4.55), while $\mathcal{G}_{\rm D}^{(-)}(\Delta_\perp)$ grows more slowly. In the right panel, we show the same semihard coefficients evolved over a short interval, $\Delta Y = 3$, using the collinearly improved BK equation detailed in Sec. 2.2.2. It is clear that such a short evolution does not bring significant changes in the behavior of the semihard coefficients. However, we observe that $\mathcal{G}_{\rm D}^{(-)}(\Delta_\perp)$ for $\Delta_\perp \gg Q_s$ is no longer power suppressed as it was in the MV model. Still, since its contribution to the cross section is of the same form as the one from $\mathcal{G}_{\rm D}^{(+)}(\Delta_\perp)$ (i.e., independent of the angle ϕ) but much smaller, it can be safely neglected for practical purposes.

We further analyze the constraints on the factors $\mathcal{G}_{\rm D}^{(n)}(\Delta_\perp)$ imposed by the positivity of the transverse and longitudinal cross sections, as well as their dependence on terms proportional to $\cos n\phi$. To simplify the notation, we rewrite the reduced cross sections in Eqs. (4.45) and (4.48) in order to highlight their dependence on $\cos n\phi$ and the momenta $\boldsymbol{P}$ and $\boldsymbol{\Delta}$, namely

$$\left|\mathcal{A}_{\rm D}^{\lambda}\right|^2 = \mathcal{N}_0^{\lambda}(P_\perp, \Delta_\perp) + 2\sum_{n=1}^{\infty} \mathcal{N}_n^{\lambda}(P_\perp, \Delta_\perp)\cos n\phi. \tag{4.56}$$

At the leading twist level, where we have been working so far, the only non-vanishing terms are $\mathcal{N}_n^{\lambda}$ with $n = 0, 2, 4$. Therefore, since the averaged reduced cross sections $\mathcal{N}_0^{\lambda}$ are explicitly positive, we can equivalently analyze the ratios $|\mathcal{A}_{\rm D}^{\lambda}|^2/\mathcal{N}_0^{\lambda}$. To do so, we minimize these ratios as a function of $P_\perp^2$ and ϕ and require that the minimum value remains non-negative. Focusing on the longitudinal sector, we begin by keeping only the $\mathcal{G}_{\rm D}^{(+)}(\Delta_\perp)$ and $\mathcal{G}_{\rm D}^{(1)}(\Delta_\perp)$ terms in $|\mathcal{A}_{\rm D}^{\lambda}|^2$ (see Eq. (4.48)), since the contribution from $\mathcal{G}_{\rm D}^{(1)}(\Delta_\perp)$ is the only one comparable to $\mathcal{G}_{\rm D}^{(+)}(\Delta_\perp)$ in the MV model, particularly in the regime where $\Delta_\perp$ is of the order of Q_s or higher. As a result, $|\mathcal{A}_{\rm D}^{L}|^2/\mathcal{N}_0^{L}$ has a global minimum at $\phi = 0$ and $P_\perp = \bar{Q}/\sqrt{3}$, leading to the positivity constraint $\mathcal{G}_{\rm D}^{(+)}(\Delta_\perp) - 2\mathcal{G}_{\rm D}^{(1)}(\Delta_\perp) \geq 0$. We observe that, in the leading logarithmic behavior

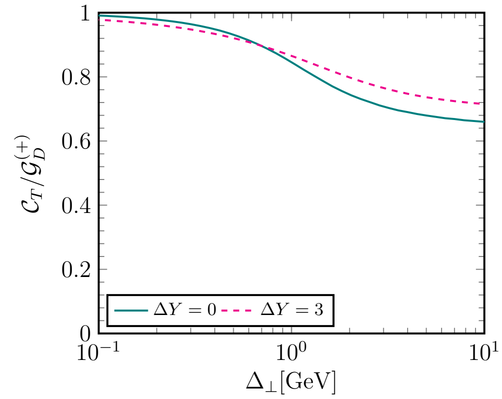

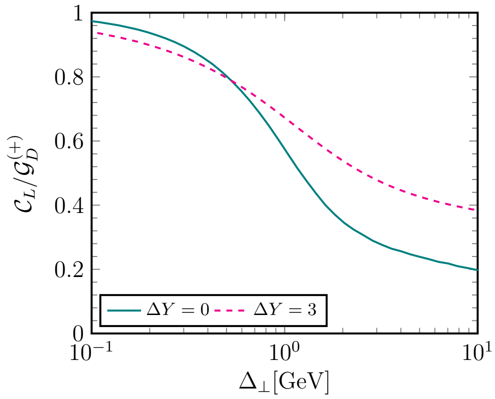

Figure 4.5: The l.h.s. of the two positivity constraints normalized to $\mathcal{G}_{\mathrm{D}}^{(+)}(\Delta_\perp)$. Left panel: transverse sector [cf. Eq. (4.58)]. Right panel: longitudinal sector [cf. Eq. (4.57)].

for $\Delta_\perp \gg Q_s$ in the MV model (shown in Eq. (4.53)), this constraint reaches equality, or "saturates". This property is very similar to that found for the unpolarized and linearly polarized gluon distributions [26]. When including the contribution from $\mathcal{G}_{\mathrm{D}}^{(2)}(\Delta_\perp)$, while still neglecting $\mathcal{G}_{\mathrm{D}}^{(-)}(\Delta_\perp)$, the constraint of interest is given by the relation

$$\mathcal{C}_L(\Delta_\perp) \equiv \mathcal{G}_{\mathrm{D}}^{(+)}(\Delta_\perp) - 2\mathcal{G}_{\mathrm{D}}^{(1)}(\Delta_\perp) + \frac{1}{2}\,\mathcal{G}_{\mathrm{D}}^{(2)}(\Delta_\perp) \geq 0. \tag{4.57}$$

In the regime where $\Delta_\perp \gg Q_s$, it can be shown analytically that, by keeping all the $1/\Delta_\perp^2$ terms (and not only those enhanced by a logarithm) in the MV model, the l.h.s. in Eq. (4.57) is strictly positive. In the transverse sector, the corresponding positivity constraint is given by

$$\mathcal{C}_T(\Delta_\perp) \equiv \mathcal{G}_{\mathrm{D}}^{(+)}(\Delta_\perp) - \frac{2}{3}\,\mathcal{G}_{\mathrm{D}}^{(1)}(\Delta_\perp) - \frac{1}{2}\,\mathcal{G}_{\mathrm{D}}^{(2)}(\Delta_\perp) \geq 0. \tag{4.58}$$

In Fig. 4.5, we present the numerical calculations of the constraints in Eqs. (4.57) and (4.58), demonstrating their validity over a wide range of $\Delta_\perp$. These calculations are performed using the MV model and its evolution, as described by the solution to the collinearly improved BK equation.

4.5 Analytical estimates and numerical results of the average cross sections

In this section we consider the incoherent diffractive cross sections averaged over the angle ϕ between the momenta $\boldsymbol{\Delta}$ and $\boldsymbol{P}$, namely

$$\frac{\mathrm{d}\sigma_{\mathrm{D}}^{\gamma_\lambda^* A\to q\bar{q}X}}{\mathrm{d}\Pi} = \int_0^{2\pi} \frac{\mathrm{d}\phi}{2\pi}\, \frac{\mathrm{d}\sigma_{\mathrm{D}}^{\gamma_\lambda^* A\to q\bar{q}X}}{\mathrm{d}\vartheta_1 \mathrm{d}\vartheta_2\, \mathrm{d}^2\boldsymbol{P}\mathrm{d}^2\boldsymbol{\Delta}}, \tag{4.59}$$

with $\mathrm{d}\Pi = (2\pi)^2 P_\perp \mathrm{d}P_\perp \Delta_\perp \mathrm{d}\Delta_\perp \mathrm{d}\vartheta_1 \mathrm{d}\vartheta_2$. From Eqs. (4.45) and (4.48) it is visible that the terms involving $\mathcal{G}_{\mathrm{D}}^{(1)}(\Delta_\perp)$ and $\mathcal{G}_{\mathrm{D}}^{(2)}(\Delta_\perp)$ vanish due to the angle averaging. Therefore, the above quantity receives the contributions of $\mathcal{G}_{\mathrm{D}}^{(+)}(\Delta_\perp)$ and $\mathcal{G}_{\mathrm{D}}^{(-)}(\Delta_\perp)$. As discussed in the previous section, $\mathcal{G}_{\mathrm{D}}^{(-)}(\Delta_\perp)$ is subleading, hence for analytical estimates we consider only the contribution of $\mathcal{G}_{\mathrm{D}}^{(+)}(\Delta_\perp)$, while it is kept in the numerical calculations.

Following the notation in Eq. (4.56), the reduced transverse and longitudinal average cross sections can be written as

$$\mathcal{N}_0^T \simeq \frac{4P_\perp^2(3\bar{Q}^4 + P_\perp^4)}{(P_\perp^2 + \bar{Q}^2)^6}\, \mathcal{G}_{\mathrm{D}}^{(+)}(\Delta_\perp)\,, \quad \mathcal{N}_0^L \simeq \frac{2\bar{Q}^2(\bar{Q}^4 - 2\bar{Q}^2P_\perp^2 + 5P_\perp^4)}{(P_\perp^2 + \bar{Q}^2)^6}\, \mathcal{G}_{\mathrm{D}}^{(+)}(\Delta_\perp). \tag{4.60}$$

We are interested in getting an analytical understanding of the incoherent diffractive cross section and its magnitude w.r.t. the respective inclusive cross section. The latter is analytically known in the correlation limit [27, 113] and it is reviewed in Appendix C. Hence, we proceed to study the ratio of the averaged cross sections, namely

$$\frac{\mathrm{d}\sigma_{\mathrm{D}}^{\gamma_T^* A\to q\bar{q}X}/\mathrm{d}\Pi}{\mathrm{d}\sigma_{\mathrm{inc}}^{\gamma_T^* A\to q\bar{q}X}/\mathrm{d}\Pi} = \frac{1}{2N_c^2}\, \frac{4P_\perp^2(3\bar{Q}^4 + P_\perp^4)}{(P_\perp^4 + \bar{Q}^4)(P_\perp^2 + \bar{Q}^2)^2}\, \frac{\mathcal{G}_{\mathrm{D}}^{(+)}(\Delta_\perp)}{(4\pi^3\alpha_s/C_F)\, xG(\Delta_\perp)} \tag{4.61}$$

for the transverse polarizations and

$$\frac{\mathrm{d}\sigma_{\mathrm{D}}^{\gamma_L^* A\to q\bar{q}X}/\mathrm{d}\Pi}{\mathrm{d}\sigma_{\mathrm{inc}}^{\gamma_L^* A\to q\bar{q}X}/\mathrm{d}\Pi} = \frac{1}{2N_c^2}\, \frac{\bar{Q}^4 - 2\bar{Q}^2P_\perp^2 + 5P_\perp^4}{P_\perp^2(P_\perp^2 + \bar{Q}^2)^2}\, \frac{\mathcal{G}_{\mathrm{D}}^{(+)}(\Delta_\perp)}{(4\pi^3\alpha_s/C_F)\, xG(\Delta_\perp)}, \tag{4.62}$$

for the longitudinal one. The factor $xG(\Delta_\perp)$ is the unpolarized unintegrated gluon distribution in the target, cf. Eq. (C.3), and it is dimensionless. In both ratios we have factorized the fraction that encodes the semihard dynamics, and in the regime $\Delta_\perp \sim Q_s$ it is of the order of Q_s^2. Generally it is a function that varies slowly with $\Delta_\perp$. Thus, the behavior of the ratios, when $P_\perp \sim \bar{Q}$, has the form

$$\frac{\mathrm{d}\sigma_{\mathrm{D}}^{\gamma_\lambda^* A\to q\bar{q}X}/\mathrm{d}\Pi}{\mathrm{d}\sigma_{\mathrm{inc}}^{\gamma_\lambda^* A\to q\bar{q}X}/\mathrm{d}\Pi} \sim \frac{1}{N_c^2}\, \frac{Q_s^2}{P_\perp^2}. \tag{4.63}$$

We explicitly observe the $1/N_c^2$ suppression discussed in Sect.3.1.2. Additionally, we note the stronger suppression given by the $1/P_\perp^6$ fall-off in the diffractive case, which is much more significant than the $1/P_\perp^4$ suppression in the inclusive case. Nevertheless, the precise $P_\perp$ dependence of the ratio differs significantly between the two polarizations, and this distinction is related to the relative magnitude of $P_\perp$ w.r.t. $\bar{Q}$. In the transverse sector, at small $P_\perp$, the ratio vanishes quadratically, while at large $P_\perp$, it falls off as $1/P_\perp^2$. This indicates a maximum at a value $P_\perp^*$, which is proportional to $\bar{Q}$, and the numerical solution to the resulting algebraic equation yields $P_\perp^* \simeq 0.75\bar{Q}$. In the longitudinal sector, the scale for both small and large $P_\perp$ is of the form $1/P_\perp^2$, but with different coefficients in each limit. These features were previously observed in the numerical study by [34], our work instead focuses on providing an analytical understanding of them in the correlation limit.

The angle-averaged reduced cross sections as functions of $P_\perp$ and $\Delta_\perp$ are shown in Fig. 4.6. The harder tail in $P_\perp$, compared to $\Delta_\perp$, is visible in both the transverse and longitudinal cross sections at high momenta. On the other hand, as discussed in Eq. (4.55), when $\Delta_\perp$ decreases and becomes smaller than Q_s, the cross section shows a logarithmic increase.

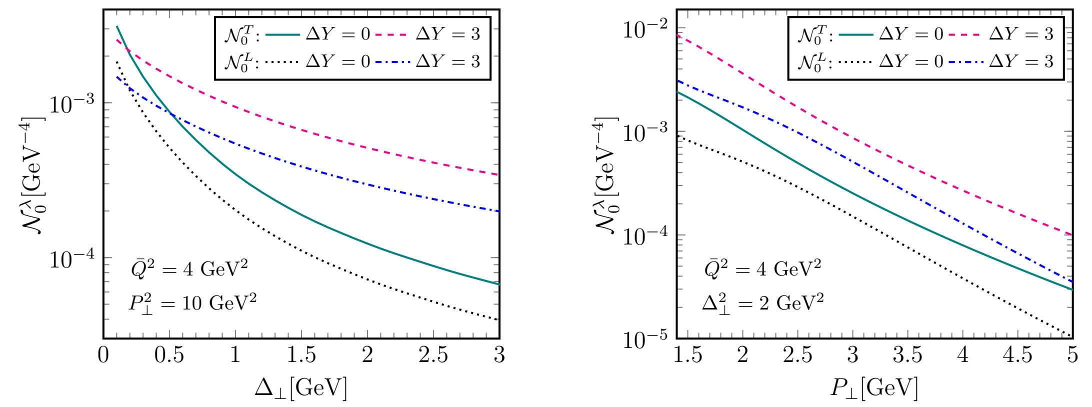

Figure 4.6: The angle-averaged reduced incoherent diffractive dijet cross section at leading twist. Left panel: as a function of the momentum transfer $\Delta_\perp$ for a fixed relative momentum $P_\perp$. Right panel: as a function of $P_\perp$ for a fixed $\Delta_\perp$.

4.6 The azimuthal anisotropies

The azimuthal anisotropies are the objects sensitive to the relative angle between $\boldsymbol{\Delta}$ and $\boldsymbol{P}$, and are defined as the dimensionless ratios

$$\langle \cos n\phi \rangle_\lambda = \int_0^{2\pi} \frac{\mathrm{d}\phi}{2\pi} \cos n\phi \, \frac{\mathrm{d}\sigma_{\mathrm{D}}^{\gamma_\lambda^* A \to q\bar{q}X}}{\mathrm{d}\vartheta_1 \mathrm{d}\vartheta_2 \, \mathrm{d}^2\boldsymbol{P} \mathrm{d}^2\boldsymbol{\Delta}} \Bigg/ \int_0^{2\pi} \frac{\mathrm{d}\phi}{2\pi} \frac{\mathrm{d}\sigma_{\mathrm{D}}^{\gamma_\lambda^* A \to q\bar{q}X}}{\mathrm{d}\vartheta_1 \mathrm{d}\vartheta_2 \, \mathrm{d}^2\boldsymbol{P} \mathrm{d}^2\boldsymbol{\Delta}} = \frac{\mathcal{N}_n^\lambda}{\mathcal{N}_0^\lambda}, \tag{4.64}$$

where n is an even integer. At leading twist, the non-vanishing anisotropies are the elliptic $\langle \cos 2\phi \rangle_\lambda$ and the quadrangular $\langle \cos 4\phi \rangle_\lambda$ ones, as visible in Eqs. (4.45) and (4.48), and read

$$\langle \cos 2\phi \rangle_T \simeq \frac{2\bar{Q}^2(\bar{Q}^2 - P_\perp^2)}{3\bar{Q}^4 + P_\perp^4} \frac{\mathcal{G}_{\mathrm{D}}^{(1)}(\Delta_\perp)}{\mathcal{G}_{\mathrm{D}}^{(+)}(\Delta_\perp)}, \qquad \langle \cos 2\phi \rangle_L \simeq \frac{4P_\perp^2(P_\perp^2 - \bar{Q}^2)}{\bar{Q}^4 - 2\bar{Q}^2 P_\perp^2 + 5P_\perp^4} \frac{\mathcal{G}_{\mathrm{D}}^{(1)}(\Delta_\perp)}{\mathcal{G}_{\mathrm{D}}^{(+)}(\Delta_\perp)} \tag{4.65}$$

and

$$\langle \cos 4\phi \rangle_T \simeq -\frac{\bar{Q}^2 P_\perp^2}{3\bar{Q}^4 + P_\perp^4} \frac{\mathcal{G}_{\mathrm{D}}^{(2)}(\Delta_\perp)}{\mathcal{G}_{\mathrm{D}}^{(+)}(\Delta_\perp)}, \qquad \langle \cos 4\phi \rangle_L \simeq \frac{2P_\perp^4}{\bar{Q}^4 - 2\bar{Q}^2 P_\perp^2 + 5P_\perp^4} \frac{\mathcal{G}_{\mathrm{D}}^{(2)}(\Delta_\perp)}{\mathcal{G}_{\mathrm{D}}^{(+)}(\Delta_\perp)}. \tag{4.66}$$

As discussed at the end of Sect. 4.3, we observe that $\langle \cos 2\phi \rangle_\lambda$ is proportional to $\mathcal{G}_{\mathrm{D}}^{(1)}(\Delta_\perp)$ while $\langle \cos 4\phi \rangle_\lambda$ is proportional to $\mathcal{G}_{\mathrm{D}}^{(2)}(\Delta_\perp)$. We also observe the opposite sign between $\langle \cos 2\phi \rangle_T$ and $\langle \cos 2\phi \rangle_L$, and similarly for the $\langle \cos 4\phi \rangle_\lambda$ anisotropies, a fact that can be written with the relations

$$\langle \cos 2\phi \rangle_T \langle \cos 2\phi \rangle_L \leq 0 \qquad \text{and} \qquad \langle \cos 4\phi \rangle_T \langle \cos 4\phi \rangle_L < 0. \tag{4.67}$$

As observed in Eq. (4.65), $\langle \cos 2\phi \rangle_\lambda$ can vanish. Indeed, one has

$$\langle \cos 2\phi \rangle_T = \langle \cos 2\phi \rangle_L = 0 \quad \text{when} \quad P_\perp = \bar{Q} \quad \text{for any} \quad \Delta_\perp, \tag{4.68}$$

which are zeros similar to the ones appearing in coherent diffractive dijet production [51]. In the "all twist" numerical solution [34], the zero in the transverse sector does not exist. We shall see

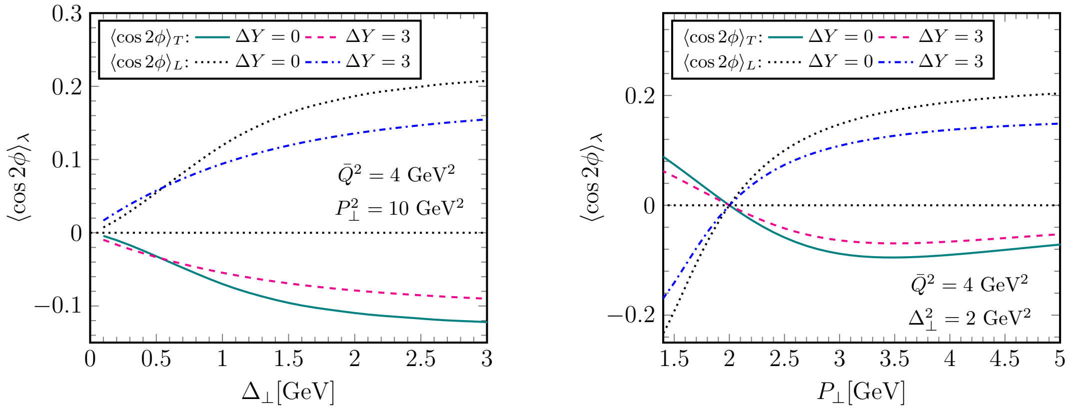

Figure 4.7: Diffractive $\langle\cos 2\phi\rangle_\lambda$ azimuthal anisotropies at leading twist. Left panel: as a function of the momentum transfer $\Delta_\perp$ for a fixed relative momentum $P_\perp$. Right panel: as a function of $P_\perp$ for a fixed $\Delta_\perp$.

in Sect. 4.6.1 that in the correlation limit, this property can be well described when taking into account the first higher twist correction.

When comparing the azimuthal anisotropies in the present case with those in inclusive dijet production, we observe that in the inclusive case, in the correlation limit at leading twist, only the $\langle\cos 2\phi\rangle_\lambda$ anisotropies are non-zero. To obtain the $\langle\cos 4\phi\rangle_\lambda$ anisotropies in such a case, higher twist effects must be considered [121], which are power suppressed by either $Q_s^2/P_\perp^2$ or $\Delta_\perp^2/P_\perp^2$. In contrast, for incoherent diffractive dijet production, the $\langle\cos 4\phi\rangle_\lambda$ anisotropies are parametrically of the same order as the $\langle\cos 2\phi\rangle_\lambda$ anisotropies, as all the hard coefficients are of the same order in $P_\perp$.

In Fig. 4.7, the $\langle\cos 2\phi\rangle_\lambda$ azimuthal anisotropies are shown for the MV model and its evolution over a few units of rapidity. We observe a smaller anisotropy as the momentum transfer $\Delta_\perp$ decreases, and the zeros at $P_\perp = \bar{Q}$, determined by the hard factors, are clearly visible.

Similar features are observed in the numerical solutions for the $\langle\cos 4\phi\rangle_\lambda$ anisotropies shown in Fig. 4.8 (except for the discussed zeros). We also note that in the MV model, and to some extent in the BK solution, the semihard factors satisfy the relation $\mathcal{G}_{\mathrm{D}}^{(2)}(\Delta_\perp) \ll \mathcal{G}_{\mathrm{D}}^{(1)}(\Delta_\perp)$ for all relevant momenta due to the presence of large logarithmic factors, as seen in Eqs. (4.53) and (4.54). Thus, although both $\langle\cos 2\phi\rangle_\lambda$ and $\langle\cos 4\phi\rangle_\lambda$ are of the same twist, the quadrangular anisotropy is eventually smaller than the elliptic one.

4.6.1 Higher twist kinematic corrections

In this work, we focus on hard jets in the correlation limit, where the relative momentum $P_\perp$ is much larger than the semihard scales, including the momentum transfer $\Delta_\perp$ and the saturation momentum Q_s. The higher twist corrections then arise from considering contributions proportional to powers of the ratios $Q_s/P_\perp$ and $\Delta_\perp/P_\perp$ beyond the leading-order expansion. The powers of the ratio $Q_s/P_\perp$ are referred to as "genuine saturation" effects, or saturation twists. To fully account for these contributions, one must employ a numerical approach [34]. Our interest, however, is focused on hard jets, which leads us to consider the "kinematic twists", where contributions involving powers of $\Delta_\perp/P_\perp$ [122–124] play a significant role.

To resum the kinematic twists one can rely on the improved TMD framework and follow

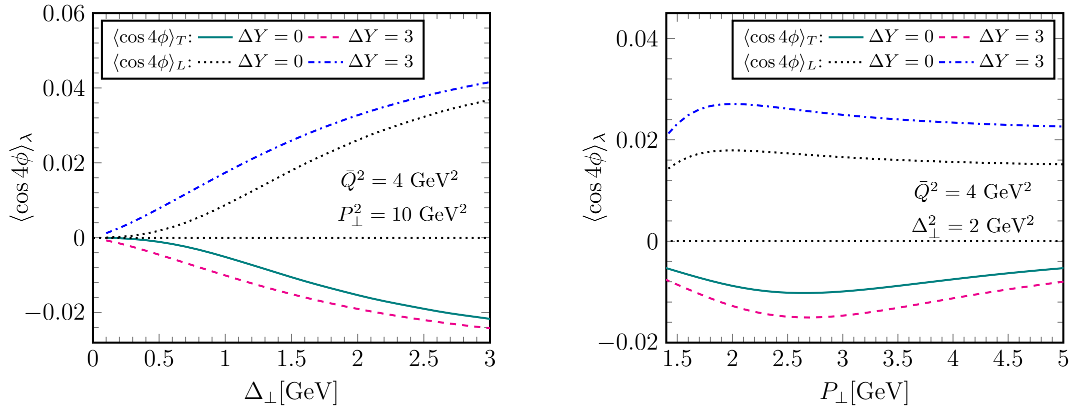

Figure 4.8: Diffractive $\langle\cos 4\phi\rangle_\lambda$ azimuthal anisotropies at leading twist. Left panel: as a function of the momentum transfer $\Delta_\perp$ for a fixed relative momentum $P_\perp$. Right panel: as a function of $P_\perp$ for a fixed $\Delta_\perp$.

the procedure developed in [123] (see e.g. [37] for the implementation in the case of inclusive dijet production). Our goal in this work is more modest, in the sense that we consider only the first higher order kinematic twist and we show that this is enough to have a good analytical description of the anisotropies in the kinematic region of interest.

Before proceeding to the calculation, we point out that at leading twist the only dependence of the fractions ϑ_1 and ϑ_2 in the reduced cross section is given by the hard quantity $\bar{Q}$. On the other hand, in the first higher twist correction we see by explicit calculation that the reduced cross section has an explicit dependence on such fractions. Hence, in order to keep the problem simple, we take $\vartheta_1 = \vartheta_2$ in the rest of this section.

Starting from the general expression in Eq. (4.17) for the transverse cross section (and similarly for the longitudinal one), the correlator $\mathcal{W}_{\rm D}(\boldsymbol{r}, \bar{\boldsymbol{r}}, \boldsymbol{B})$ defined in Eq. (4.18) must be expanded to the 6th order in the dipole sizes r and/or $\bar{r}$, in contrast to the 4th-order expansion at leading twist in Eq. (4.30). The additional two powers in the dipole sizes result in an extra $1/P_\perp^2$ factor in the cross section in momentum space. Similarly, the higher-order expansion introduces two more derivatives, which, after Fourier transforming, lead to a factor proportional to the semihard scales, either $\Delta_\perp^2$ or Q_s^2. The kinematic correction corresponds to the former case.

The leading contribution to this correction comes from terms with the fewest factors involving $\ln \mathcal{S}_g(B)$, which scales like Q_s^2. As with the leading twist, this contribution involves only two factors. In other words, by expanding f, defined in Eq. (4.23), to the 4th order in the small dipole size and inserting it into Eq. (4.28), we find that the first-order kinematic correction to the transverse and longitudinal reduced cross sections, Eqs. (4.33) and (4.46), is given by:

$$\delta\big|\mathcal{A}_{\rm D}^T\big|^2 = \frac{1}{6}\, H_T^{ikmns}(\boldsymbol{P}, \bar{Q})\, H_T^{jls*}(\boldsymbol{P}, \bar{Q})\, \mathcal{G}_{\rm D}^{ij,klmn}(\boldsymbol{\Delta}), \tag{4.69}$$

and

$$\delta\big|\mathcal{A}_{\rm D}^L\big|^2 = \frac{1}{6}\, H_L^{ikmn}(\boldsymbol{P}, \bar{Q})\, H_L^{jl*}(\boldsymbol{P}, \bar{Q})\, \mathcal{G}_{\rm D}^{ij,klmn}(\boldsymbol{\Delta}), \tag{4.70}$$

respectively. The hard factors $H_T^{ikmns}(\boldsymbol{P}, \bar{Q})$ and $H_L^{ikmn}(\boldsymbol{P}, \bar{Q})$ are the evident extension of the leading ones in Eqs. (4.34) and (4.47) with two more indices each and their details are shown in

Appendix D. On the other hand, the rank-6 semi-hard tensor reads

$$\mathcal{G}_{\rm D}^{ij,klmn}(\boldsymbol{\Delta}) = \int \frac{\mathrm{d}^2\boldsymbol{B}}{2\pi}\, e^{-i\boldsymbol{\Delta}\cdot\boldsymbol{B}}\, \Phi(B)\, [\partial^i\partial^j \ln \mathcal{S}_g(B)]\, [\partial^k\partial^l\partial^m\partial^n \ln \mathcal{S}_g(B)], \tag{4.71}$$

and its tensor decomposition is also given in Appendix D. In this section we are only interested on the final expressions for the MV model, which can be expressed in terms of elementary integrations over the adjoint dipole size B. Hence, by using the notation in Eq. (4.56), the corrections to the averaged over angle reduced cross sections for the transverse sector is given by (recall that $Q_A^2 \ln \frac{Q_s^2}{\Lambda^2} = Q_s^2$)

$$\delta\mathcal{N}_0^T = -\frac{16P_\perp^2\bar{Q}^2(7\bar{Q}^4 - 7\bar{Q}^2P_\perp^2 + 2P_\perp^4)}{(P_\perp^2+\bar{Q}^2)^8}\, Q_A^4 \int \frac{\mathrm{d}B}{B}\, J_0(\Delta_\perp B)\Phi(B) \tag{4.72}$$

while for the longitudinal one reads

$$\delta\mathcal{N}_0^L = -\frac{16\bar{Q}^2(\bar{Q}^6 - 5\bar{Q}^4P_\perp^2 + 8\bar{Q}^2P_\perp^4 - 2P_\perp^6)}{(P_\perp^2+\bar{Q}^2)^8}\, Q_A^4 \int \frac{\mathrm{d}B}{B}\, J_0(\Delta_\perp B)\Phi(B). \tag{4.73}$$

Such expressions diverge logarithmically at small B, however, they are valid in the regime where $r \ll B$, and therefore we are allowed to set a UV cutoff equal to $c_0/P_\perp$ in the integrations in Eqs. (4.72) and (4.73), where c_0 is a constant of the order of one [5].

Analogously, we can calculate the corrections to the numerator of the $\langle\cos 2\phi\rangle_\lambda$ anisotropies. For the transverse sector we find

$$\begin{aligned}\delta\mathcal{N}_2^T = \frac{8P_\perp^2}{(P_\perp^2+\bar{Q}^2)^8}\, Q_A^4 \Bigg[&(12\bar{Q}^6 - 34\bar{Q}^4P_\perp^2 + 6\bar{Q}^2P_\perp^4 - 4P_\perp^6)\int \frac{\mathrm{d}B}{B}\, J_2(\Delta_\perp B)\Phi(B)\\ &- (7\bar{Q}^6 - 20\bar{Q}^4P_\perp^2 + 3\bar{Q}^2P_\perp^4 - 2P_\perp^6)\int \frac{\mathrm{d}B}{B}\, J_2(\Delta_\perp B)\Phi(B)\ln\frac{4}{B^2\Lambda^2}\Bigg]\end{aligned} \tag{4.74}$$

and for the longitudinal one

$$\begin{aligned}\delta\mathcal{N}_2^L = \frac{8P_\perp^2\bar{Q}^2(\bar{Q}^2-P_\perp^2)}{(P_\perp^2+\bar{Q}^2)^8}\, Q_A^4 \Bigg[&(15P_\perp^2 - 13\bar{Q}^2)\int \frac{\mathrm{d}B}{B}\, J_2(\Delta_\perp B)\Phi(B)\\ &+ 8(\bar{Q}^2 - P_\perp^2)\int \frac{\mathrm{d}B}{B}\, J_2(\Delta_\perp B)\Phi(B)\ln\frac{4}{B^2\Lambda^2}\Bigg].\end{aligned} \tag{4.75}$$

Unlike in the case of $\delta\mathcal{N}_0^\lambda$, the integrals involved in the corrections $\delta\mathcal{N}_2^\lambda$ are UV finite since the Bessel function $J_2(\Delta_\perp B)$ vanishes quadratically for small arguments. We note that now only the longitudinal anisotropy vanishes when $P_\perp = \bar{Q}$, while the kinematic correction to the transverse sector shows that the value of $P_\perp$ at which $\langle\cos 2\phi\rangle_T$ changes sign increases with $\Delta_\perp$. We further observe that when $P_\perp > \bar{Q}$, the kinematic correction to $\langle\cos 2\phi\rangle_T$ is positive and increases with $\Delta_\perp$, rather than being negative and decreasing as in the case of the leading twist [cf. Eq. (4.65)]. So, in fact, the higher twist correction implies a minimum in $\Delta_\perp$ as a function of $\Delta_\perp$ for $P_\perp > \bar{Q}$. In Fig. 4.9, the $\langle\cos 2\phi\rangle_\lambda$ anisotropies are shown in the MV model when the first higher kinematic twist is included.

[5] It can be checked numerically that the precise choice of c_0 does not produce sensitive changes to the results here presented.

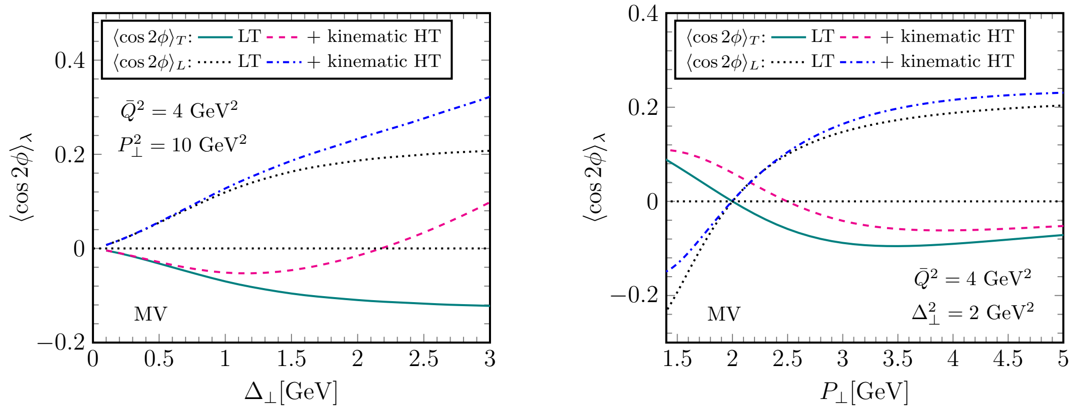

Figure 4.9: Diffractive $\langle\cos 2\phi\rangle_\lambda$ azimuthal anisotropies including the first higher kinematic twist. Left panel: as a function of the momentum transfer $\Delta_\perp$ for fixed relative momentum $P_\perp$. Right panel: as a function of $P_\perp$ for fixed $\Delta_\perp$.

All these features, obtained semi-analytically in the region where $P_\perp^2$ is (much) larger than Q_s^2 are in good agreement with the fully numerical solution and the discussion given in [34] (cf. Fig. 3 there).

We conclude this section commenting that the first higher order twist provides also expressions for the remaining non-vanishing quantities $\delta\mathcal{N}_4^\lambda$ and $\delta\mathcal{N}_6^\lambda$ which contribute to the corresponding $\langle\cos 4\phi\rangle_\lambda$ and $\langle\cos 6\phi\rangle_\lambda$ anisotropies, although, they are out of the scope of the present work.

Chapter 5

The $q\bar{q}g$ Contribution

In this chapter we consider the production mechanism of two hard jets accompanied by a third semihard jet. As was shown in the previous chapter, at leading order in QCD perturbation theory, the cross section exhibits a $1/P_{\perp}^{6}$ spectrum. When a third jet accompanies the hard dijet, with transverse momentum $\boldsymbol{k}$ such that $k_{\perp} \sim Q_s \ll P_{\perp}$, the large size $R \sim 1/k_{\perp} \sim 1/Q_s$ controls the scattering and becomes strong, leading to a $1/P_{\perp}^{4}$ spectrum. At the same time, such a NLO calculation comes with an extra factor $\alpha_s(P_{\perp})$, nevertheless, this dependence is only logarithmic and when $P_{\perp} \gg Q_s$, the softer power law is the most relevant factor. This mechanism was originally studied in detail for the case of coherent production [52, 55, 56] and here we shall apply the same ideas. The third semi-hard jet can be composed of any parton, i.e., a gluon, a quark or an antiquark. Another significant feature of the third semi-hard jet is that it must be soft. In fact, when its formation time $2k^{+}/k_{\perp}^{2}$ is of the order of the virtual photon lifetime $2q^{+}/Q^{2}$, its splitting fraction $\vartheta \equiv k^{+}/q^{+}$ satisfies the relation $\vartheta \sim k_{\perp}^{2}/Q^{2} \sim Q_s^{2}/P_{\perp}^{2} \ll 1$. At the same time, as it will be explicitly visible in next sections, partons with even smaller longitudinal momentum fraction than the above estimate diminish the rapidity gap of the process, and thus are not interesting to our purposes. In the following, we will refer to the third jet as either semi-hard jet or soft jet.

5.1 2+1 jets: soft gluons

Following the derivation for the coherent case [55] and making the appropriate adaptations to the incoherent case, here we present the 2+1 jet incoherent diffractive cross section for a gluon semi-hard jet. In this scenario, after the virtual photon decays in a quark-antiquark pair with size r, any of the two fermions is allowed to emit a soft gluon with momentum fraction ϑ_3 and transverse momentum $\boldsymbol{k}_3$ at a distance R. When $r \ll R$, the $q\bar{q}g$ fluctuation can be treated as an effective gluon-gluon dipole that subsequently scatters strongly off the nuclear target, acquiring a transverse momentum $\boldsymbol{\Delta}$ and a minus longitudinal momentum $x_{\mathbb{P}}P_N^{-}$. While the gluon fraction ϑ_3 of the plus longitudinal momentum q^{+} of the virtual photon fulfills $\vartheta_3 \ll 1$, the quark and antiquark longitudinal momentum fractions ϑ_1 and ϑ_2 follow the relation $\vartheta_1 + \vartheta_2 \simeq 1$. The final transverse momenta $\boldsymbol{k}_1$ of the quark and $\boldsymbol{k}_2$ of the antiquark are hard and their imbalance receives contributions from both the gluon recoil and the momentum transfer, since transverse momentum conservation requires $\boldsymbol{k}_1 + \boldsymbol{k}_2 = -\boldsymbol{k}_3 + \boldsymbol{\Delta}$. This is a characteristic sign of the present process in contrast to the coherent and the 2 jets incoherent one, where only either the recoil momentum or the momentum transfer, respectively, contribute to the imbalance. In Fig. 5.1 we show the two amplitudes contributing to the scattering which correspond to the scattering off

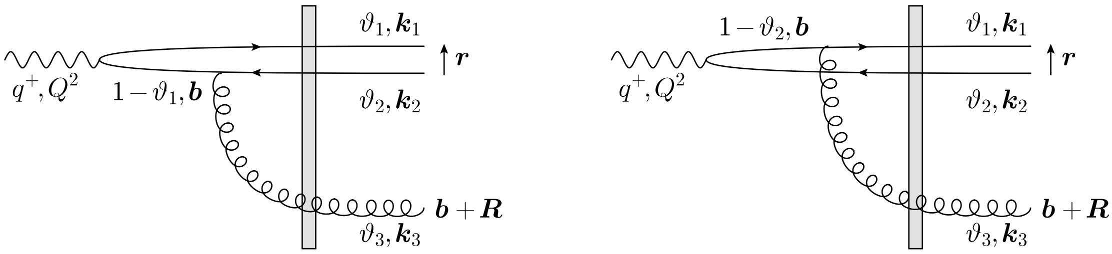

Figure 5.1: Production of a hard quark-antiquark pair accompanied by a soft gluon in DIS off a nucleus within the dipole picture. The scattering off the shockwave is considered only after the gluon emission, as the large pair is formed subsequent to the gluon vertex.

the shockwave only after the gluon emission. In fact, within the transverse momentum hierarchy here considered, the interaction of the $q\bar{q}$ pair with the target prior to the emission of the gluon effectively corresponds to the no-scattering limit.

For convenience, we work with the definitions $\boldsymbol{k}_1 = \boldsymbol{P} + \vartheta_1(\boldsymbol{\Delta} - \boldsymbol{k}_3)$ and $\boldsymbol{k}_2 = -\boldsymbol{P} + \vartheta_2(\boldsymbol{\Delta} - \boldsymbol{k}_3)$, such that we use the hard momentum $\boldsymbol{P}$ and the semi-hard momenta $\boldsymbol{k}_3$ and $\boldsymbol{\Delta}$ as independent variables. In Fig. 5.2 we provide a clear depiction of a typical configuration of interest in coordinate space.

The derivation of the cross section is similar to the one for coherent production, differing only in the diffractive correlator, and it is given in detail in [55]. Prior to presenting here the expressions for the incoherent cross section, some comments are useful. The exact quark-antiquark-gluon component in the LCWF of a virtual photon was calculated in [125, 126]. Generally, the gluon emission can change the transverse coordinate of the emitter fermion due to recoil. In order to ensure that the transverse recoil is negligible and guarantee that the relation $r \ll R$ remains valid in all stages of the process, it is necessary to impose $\vartheta_3 \ll k_{3\perp}/P_\perp$. The addition of the multiple scattering off the target is done in the shockwave formalism by multiplying the corresponding Wilson lines with the projectile wave function. The hierarchy in coordinate space and the color flow implies that the $q\bar{q}g$ system effectively acts as a gluon-gluon dipole. This fact leads to the emergence of adjoint S-matrices, which then can be used analogously to the fundamental ones in the problem of dijet production described in the previous chapter. It is also worth mentioning that besides the fact that the hard factor for coherent and incoherent 2+1 jet diffractive production is the same, it also coincides to the one in inclusive dijet production. Thus, restricting again to the case of a transverse polarized photon, the hard factor reads

$$H_T^{ij(g)}(\vartheta_1, \vartheta_2, \boldsymbol{P}, \bar{Q}) = \big(\vartheta_1^2 + \vartheta_2^2\big) \int \frac{\mathrm{d}^2\boldsymbol{r}}{2\pi}\, \frac{\mathrm{d}^2\bar{\boldsymbol{r}}}{2\pi}\, e^{-i\boldsymbol{P}\cdot(\boldsymbol{r}-\bar{\boldsymbol{r}})}\, r^i \bar{r}^j\, \frac{\boldsymbol{r}\cdot\bar{\boldsymbol{r}}}{r\bar{r}}\, \bar{Q}\, K_1\big(\bar{Q}r\big) \bar{Q}\, K_1\big(\bar{Q}\bar{r}\big). \tag{5.1}$$

where we use the superscript (g) to denote that the soft parton in the configuration is the gluon. When compared to the corresponding factor in equation (4.17), it is visible an extra factor r^i in the DA (and similarly $\bar{r}^j$ in the CCA) that comes from the vertex emission of a large-size gluon with polarization i from the fermionic dipole of size r. By performing the integrals and rewriting the rank-2 tensor in diagonal and traceless parts, we get

$$\begin{aligned} H_T^{ij(g)}(\vartheta_1, \vartheta_2, \boldsymbol{P}, \bar{Q}) &= \big(\vartheta_1^2 + \vartheta_2^2\big) \left[\frac{(P_\perp^4 + \bar{Q}^4)}{(P_\perp^2 + \bar{Q}^2)^4}\, \delta^{ij} - \frac{4\bar{Q}^2 P_\perp^2}{(P_\perp^2 + \bar{Q}^2)^4}\, \hat{P}^{ij} \right] \\ &\equiv H_T^{(g)}(P_\perp, \bar{Q})\, \delta^{ij} + H_T^{\prime(g)}(P_\perp, \bar{Q})\, \hat{P}^{ij}. \end{aligned} \tag{5.2}$$

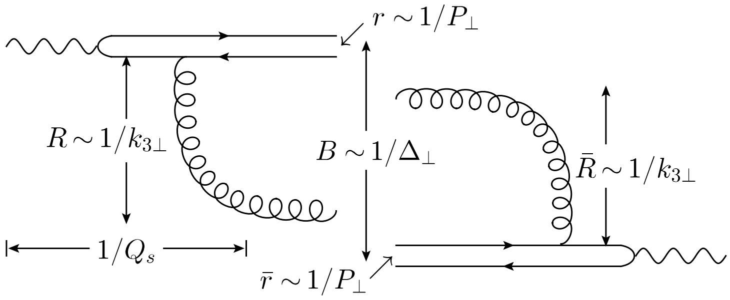

Figure 5.2: Illustration of a representative configuration contributing to the incoherent diffractive production of a hard quark-antiquark pair and a semi-hard gluon. The kinematic regime of interest is defined by $P_\perp \gg \Delta_\perp, k_{3\perp}, Q_s$, which corresponds to the relation $r, \bar{r} \ll B, R, \bar{R}, 1/Q_s$ for the various sizes and distances in coordinate space. In the typical scenario where $\Delta_\perp \sim k_{3\perp} \sim Q_s$, the distances B, R, and $\bar{R}$ are all approximately of the order of $1/Q_s$.

The three-partons invariant mass of the outgoing system for $P_\perp \gg k_{3\perp}, \Delta_\perp$ and $\vartheta_3 \ll 1$, reads

$$M_\chi^2 = (k_1 + k_2 + k_3)^2 \simeq \frac{P_\perp^2}{\vartheta_1 \vartheta_2} + \frac{k_{3\perp}^2}{\vartheta_3} \qquad \text{for } 2\,+\,1 \text{ jets.} \tag{5.3}$$

Hence, by (3.8), the splitting fraction $x_\mathbb{P}$ and the diffractive variable β can be specified keeping in mind that, as in dijet production, $|t|$ is much smaller than $Q^2 + M_\chi^2$, so it can be neglected. It is also customary to define x as the fraction of the minus longitudinal momentum of the Pomeron transferred to the $q\bar{q}$ pair, namely

$$x = \frac{\bar{Q}^2 + P_\perp^2}{\bar{Q}^2 + P_\perp^2 + (\vartheta_1\vartheta_2/\vartheta_3) k_{3\perp}^2} = \frac{\bar{Q}^2 + P_\perp^2}{\bar{Q}^2}\,\beta. \tag{5.4}$$

In other words, the fraction x regulates the rapidity interval between the hard dijet and the edge of the gap on the projectile side. The first equality in (5.4) also allow us to make a change of variables between ϑ_3 and x, a fact that will be useful in further calculations. We can also observe that for hard jets kinematics, and when ϑ_3 is of the order of $k_{3\perp}^2/P_\perp^2$, the rapidity gap in the $2+1$ jets process is roughly a unit smaller than the one in the 2 jets one, assuming equal $x_{\rm Bj}$ values.

The corresponding semi-hard factor of the cross section depends on the vectors $\boldsymbol{k}_3$ and $\boldsymbol{\Delta}$, and it has only a diagonal component, as it is shown in Appendix E, i.e.

$$\mathcal{G}^{ij}_{\rm inc}(x, x_\mathbb{P}, \boldsymbol{k}_3, \boldsymbol{\Delta}) = \frac{\delta^{ij}}{4}\, \mathcal{G}_{\rm inc}(x, x_\mathbb{P}, \boldsymbol{k}_3, \boldsymbol{\Delta}), \tag{5.5}$$

where the coefficient obtained by taking the trace of $\mathcal{G}^{ij}$ reads

$$\begin{aligned} \mathcal{G}_{\rm inc}(x, x_\mathbb{P}, \boldsymbol{k}_3, \boldsymbol{\Delta}) = \frac{1}{\pi} \int \frac{{\rm d}^2\boldsymbol{B}}{2\pi} \frac{{\rm d}^2\boldsymbol{R}}{2\pi} \frac{{\rm d}^2\bar{\boldsymbol{R}}}{2\pi}\, & e^{-i\boldsymbol{\Delta}\cdot\boldsymbol{B} - i\boldsymbol{k}_3\cdot(\boldsymbol{R}-\bar{\boldsymbol{R}})} \\ & \times \hat{R}^{ik} \hat{\bar{R}}^{ki} \mathcal{M}^2 K_2(\mathcal{M}R) \mathcal{M}^2 K_2(\mathcal{M}\bar{R}) \mathcal{W}_g(\boldsymbol{R}, \bar{\boldsymbol{R}}, \boldsymbol{B}). \end{aligned} \tag{5.6}$$

The scale $\mathcal{M}^2$ in Eq. (5.6) reads

$$\mathcal{M}^2 \equiv \frac{x}{1-x}\, k_{3\perp}^2, \tag{5.7}$$

and $\hat{R}^{ik}\hat{\bar{R}}^{ki} = (1/2)\cos 2\phi_{R\bar{R}}$, with $\phi_{R\bar{R}}$ being the angle between $\boldsymbol{R}$ and $\bar{\boldsymbol{R}}$. As previously suggested, $\mathcal{W}_g(\boldsymbol{R}, \bar{\boldsymbol{R}}, \boldsymbol{B})$ is the connected piece of the CGC correlator $\left\langle S_g(\boldsymbol{R}+\boldsymbol{b}, \boldsymbol{b})\, S_g(\bar{\boldsymbol{b}}, \bar{\boldsymbol{R}}+\bar{\boldsymbol{b}})\right\rangle$ for a homogeneous nucleus target, in analogy with Eq. (4.18), with the S-matrix S_g in the adjoint representation. It is then clear that the gluon-gluon dipole is given by the small $q\bar{q}$ pair positioned in $\boldsymbol{b}$ and the emitted gluon in $\boldsymbol{b} + R$ in the DA, and similarly for the CCA.

Since the semi-hard factor in Eq. (5.5) does not possess a traceless part, the hard factor only contributes to the cross section via its diagonal piece when performing the contraction in both transverse and longitudinal sectors. In consequence, there is no angular dependence of the type $\boldsymbol{P}\cdot\boldsymbol{\Delta}$ or $\boldsymbol{P}\cdot\boldsymbol{k}_3$ and the hard momentum dependence is given only by its magnitude $P_\perp$. Here we should also mention that the angular dependence between the $\boldsymbol{k}_3$ and $\boldsymbol{\Delta}$ is not interesting to our purposes and it disappears when integrating over $\boldsymbol{k}_3$.

Finally, we can write the incoherent diffractive cross section for 2+1 jet production when the semi-hard jet is given a soft gluon as

$$\frac{\mathrm{d}\sigma^{\gamma_\lambda^* A\to q\bar{q}(g)X}}{\mathrm{d}\vartheta_1\,\mathrm{d}\vartheta_2\,\mathrm{d}^2\boldsymbol{P}\mathrm{d}^2\boldsymbol{\Delta}\,\mathrm{d}^2\boldsymbol{k}_3\,\mathrm{d}\ln 1/x} = \alpha_{\mathrm{em}}\alpha_s\left(\sum e_f^2\right)\delta_\vartheta\, H_\lambda^{(g)}(\vartheta_1,\vartheta_2,P_\perp,\bar{Q})\,\frac{S_\perp(N_c^2-1)}{4\pi^3}\,\frac{\mathcal{G}_{\mathrm{inc}}(x,x_{\mathbb{P}},\boldsymbol{k}_3,\boldsymbol{\Delta})}{2\pi(1-x)}, \tag{5.8}$$

where we use the notation where $\delta_\vartheta \equiv \delta(1-\vartheta_1-\vartheta_2-\vartheta_3) \simeq \delta(1-\vartheta_1-\vartheta_2)$. The transverse hard factor is given by Eq. (5.2), while the longitudinal one we find

$$H_L^{(g)}(\vartheta_1,\vartheta_2,P_\perp,\bar{Q}) = 8\vartheta_1\vartheta_2\,\frac{\bar{Q}^2P_\perp^2}{(P_\perp^2+\bar{Q}^2)^4}. \tag{5.9}$$

It is now evident that for the typical hard dijet kinematics, in which ϑ_1, ϑ_2 are of the order of one-half and $P_\perp \sim \bar{Q}$, both hard factors behave like $1/P_\perp^4$.

We would like to emphasize that, in general, the CGC correlator $\mathcal{W}_g(\boldsymbol{R}, \bar{\boldsymbol{R}}, \boldsymbol{B})$ must be computed without performing any expansion in order to keep track of all possible unitarity corrections. This is due to the fact that the momenta $\Delta_\perp$ and $k_{3\perp}$ are both semi-hard, thus the corresponding sizes B and $R, \bar{R}$ can be of the order of $1/Q_s$.

5.2 2+1 jets: soft quarks

Similar to the scenario explored in the previous section, the outgoing state can also consist of a hard antiquark-gluon dijet with transverse momenta $k_{2\perp}, k_{3\perp} \sim P_\perp$ and a semi-hard quark jet with $k_{1\perp} \sim Q_s \ll P_\perp$ (or equivalently, a hard quark-gluon dijet and a semi-hard antiquark) [60]. This again represents a $q\bar{q}g$ configuration with a large size $R \sim 1/k_{1\perp} \sim 1/Q_s$, which leads to strong scattering with the target and, consequently, a dijet spectrum that falls off as $1/P_\perp^4$. Similarly to the soft gluon case of the previos section, the quark carries a small fraction $\vartheta_1 \sim k_{1\perp}^2/P_\perp^2 \ll 1$ of the longitudinal momentum q^+.

The fermionic emitters have very different momenta in the final state (for instance, the antiquark being hard and the quark semi-hard), hence the corresponding diagrams differ and must be computed separately. We consider the two distinct scenarios that lead to the desired dynamics and final state. One of them consists in the virtual photon decaying directly into a large $q\bar{q}$ pair of size R, and the semi-hard antiquark subsequently producing a hard $\bar{q}g$ pair of size $r \ll R$. Since both, the intermediate and final state configurations have a large size, the scattering with the target nucleus can occur either before or after the gluon emission. The amplitudes for these processes are depicted in Fig.5.3. In the second scenario the virtual photon decays into a hard $q\bar{q}$ pair of size r, and then the hard quark gives rise to a soft quark at a

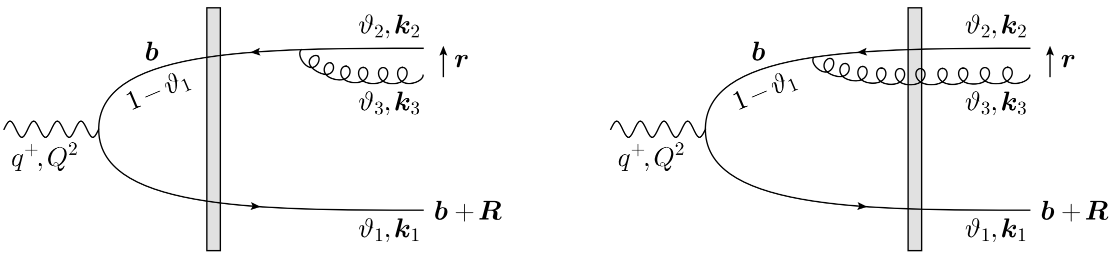

Figure 5.3: Production of a hard antiquark-gluon pair plus a soft quark in DIS off a nucleus in the dipole picture via the channel $\bar{q} \to \bar{q}g$. The large pair is formed already at the photon vertex, thus the gluon may be radiated after the scattering off the shockwave (left panel) or before the scattering off the shockwave (right panel).

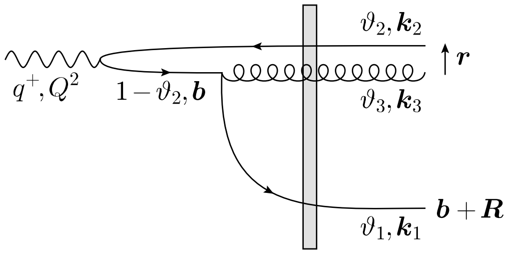

Figure 5.4: Production of a hard antiquark-gluon pair plus a soft quark in DIS off a nucleus in the dipole picture via the channel $q \to qg$. The scattering off the shockwave is taken only after the gluon radiation, since the large pair is formed after the gluon vertex.

distance $R \gg r$ and a hard gluon. Hence, the gluon and the antiquark form a hard dijet of size r. In this case, the only considerable contribution to the scattering occurs after gluon emission, as shown in the amplitude of Fig.5.4. Finally, the interference term between the two processes must also be included in the calculation of the total cross-section. A detailed derivation is given in [60] for coherent diffraction, and here we shall only present the final results adapted to the incoherent case. Similar to the soft gluon case, we now encounter the scattering of a large $q\bar{q}$ dipole with its legs at $\boldsymbol{b}+\boldsymbol{R}$ and $\boldsymbol{b}$, while the kinematics of the final hard jets are given by $\boldsymbol{k}_2 = \boldsymbol{P} + \vartheta_2(\boldsymbol{\Delta} - \boldsymbol{k}_1)$, $\boldsymbol{k}_3 = -\boldsymbol{P} + \vartheta_3(\boldsymbol{\Delta} - \boldsymbol{k}_1)$, with $\vartheta_2 + \vartheta_3 \simeq 1$ and $\Delta_\perp, k_{1\perp}, Q_s \ll P_\perp$. In coordinate space a similar picture to the one shown in Fig. 5.2 applies for the quark being the semi-hard jet.

The hard factor is the same as in coherent diffraction and in the transverse sector reads

$$H_T^{ij(q)}(\vartheta_2, \vartheta_3, P_\perp, \tilde{Q}) = \vartheta_2 \, \frac{(P_\perp^2 + \tilde{Q}^2)^2 + \vartheta_2^2 \tilde{Q}^4 + \vartheta_3^2 P_\perp^4}{P_\perp^2 (P_\perp^2 + \tilde{Q}^2)^3} \, \delta^{ij} \equiv H_T^{(q)}(\vartheta_2, \vartheta_3, P_\perp, \tilde{Q}) \, \delta^{ij}, \tag{5.10}$$

where similar to $\bar{Q}^2$ we have defined $\tilde{Q}^2 \equiv \vartheta_2 \vartheta_3 Q^2$. This tensor is obtained as the sum of the contributions given by the square of the term with gluon emission from the antiquark, the square of the term with gluon emission from the quark and the respective interference term. The property of $H_T^{ij(q)}$ being diagonal implies again that the only dependence on the hard momentum is via its magnitude. The semi-hard factor can in general be written in the form

$$\mathcal{Q}^{ij}_{\text{inc}}(x, x_{\mathbb{P}}, \boldsymbol{k}_1, \boldsymbol{\Delta}) = \frac{\delta^{ij}}{2}\, \mathcal{Q}_{\text{inc}}(x, x_{\mathbb{P}}, \boldsymbol{k}_1, \boldsymbol{\Delta}) + \hat{\mathcal{Q}}^{ij}_{\text{inc}}(x, x_{\mathbb{P}}, \boldsymbol{k}_1, \boldsymbol{\Delta}), \tag{5.11}$$

where

$$\begin{aligned}\mathcal{Q}_{\text{inc}}(x, x_{\mathbb{P}}, \boldsymbol{k}_1, \boldsymbol{\Delta}) = \frac{1}{2\pi} \int \frac{\mathrm{d}^2\boldsymbol{B}}{2\pi}\, \frac{\mathrm{d}^2\boldsymbol{R}}{2\pi}\, \frac{\mathrm{d}^2\bar{\boldsymbol{R}}}{2\pi} e^{-i\boldsymbol{\Delta}\cdot\boldsymbol{B} - i\boldsymbol{k}_1\cdot(\boldsymbol{R}-\bar{\boldsymbol{R}})} \\ \times \frac{\boldsymbol{R}\cdot\bar{\boldsymbol{R}}}{R\bar{R}}\, \mathcal{M}^2 K_1(\mathcal{M}R) \mathcal{M}^2 K_1(\mathcal{M}\bar{R}) \mathcal{W}_q(\boldsymbol{R}, \bar{\boldsymbol{R}}, \boldsymbol{B}),\end{aligned} \tag{5.12}$$

with

$$\mathcal{M}^2 \equiv \frac{x}{1-x}\, k_{1\perp}^2. \tag{5.13}$$

We recall that $\mathcal{W}_q(\boldsymbol{R}, \bar{\boldsymbol{R}}, \boldsymbol{B})$ is the connected piece of the CGC correlator $\langle S(\boldsymbol{R}+\boldsymbol{b}, \boldsymbol{b}) S(\bar{\boldsymbol{b}}, \bar{\boldsymbol{R}}+\bar{\boldsymbol{b}})\rangle$ for a homogeneous nucleus target, with S the S-matrix in the fundamental representation also appearing in Eq. (4.17). However, in this case we shall not perform any expansion in the correlator in order to analyze its behavior since, as in the soft gluon case, the sizes B, R and $\bar{R}$ can be of order of $1/Q_s$. The traceless part $\hat{\mathcal{Q}}^{ij}_{\text{inc}}$ in Eq. (5.11) does not contribute to the cross section since it must be contracted with the diagonal hard tensor in Eq. (5.10).

Having all the ingredients, the incoherent diffractive cross section for producing a hard antiquark-gluon pair with a soft quark can be written as

$$\frac{\mathrm{d}\sigma^{\gamma^*_\lambda A \to (q)\bar{q}gX}}{\mathrm{d}\vartheta_2\, \mathrm{d}\vartheta_3\, \mathrm{d}^2\boldsymbol{P} \mathrm{d}^2\boldsymbol{\Delta}\, \mathrm{d}^2\boldsymbol{k}_1\, \mathrm{d}\ln 1/x} = 2\alpha_{\text{em}}\alpha_s C_F \sum e_f^2\, \delta_\vartheta H^{(q)}_\lambda(\vartheta_2, \vartheta_3, P_\perp, \tilde{Q}) \frac{S_\perp N_c}{4\pi^3}\, \frac{\mathcal{Q}_{\text{inc}}(x, x_{\mathbb{P}}, \boldsymbol{k}_1, \boldsymbol{\Delta})}{2\pi(1-x)}, \tag{5.14}$$

where now $\delta_\vartheta \equiv \delta(1 - \vartheta_1 - \vartheta_2 - \vartheta_3) \simeq \delta(1 - \vartheta_2 - \vartheta_3)$. The longitudinal hard factor reads (see Appendix A in [60] for details)

$$H^{(q)}_L(\vartheta_2, \vartheta_3, P_\perp, \tilde{Q}) = 4\vartheta_2^2\vartheta_3\, \frac{\tilde{Q}^2}{(P_\perp^2 + \tilde{Q}^2)^3}. \tag{5.15}$$

We emphasize again that both hard factors fall-off as $1/P_\perp^4$ for typical kinematics of the hard dijet, just as in the soft gluon sector.

We conclude this chapter by noting that the structure in which the cross sections Eq. (5.8) and Eq. (5.14) are presented is deliberate and not arbitrary. This particular form has been chosen to facilitate the identification of the corresponding gluon and quark incoherent diffractive TMDs and PDFs. In the following chapter, the cross sections will be expressed in a factorized form, accompanied by a comprehensive analysis of them.

Chapter 6

Quark and Gluon Distributions

We start this chapter by interpreting the processes of interest from the target point of view. For the production of 2 hard jets we shall identify the conditions under which the dipole picture leads to the leading-twist result at high Q^2 in a partonic description of the target. Then, we shall rewrite the 2+1 jets cross sections in Eqs. (5.8) and (5.14) in a TMD factorized form. Finally, a detailed analysis of the DTMDs and DPDFs will be provided.

6.1 Incoherent DTMDs

6.1.1 SIDDIS from two hard jets production

To analyze the $q\bar{q}$ case, we will consider incoherent single inclusive diffractive DIS (SIDDIS), a process in which only the transverse momentum of a single particle is measured in the final state at fixed β and $|t|$. As there are only two particles in the final state, the longitudinal and transverse momenta of the unmeasured particle are not independent. Hence, we simply must perform a change of variables, for example from ϑ_1 to β in the transverse cross section given in Eq. (4.17). We further assume that the relative momentum is of the order of the quark and antiquark hard transverse momenta, i.e. $P_\perp \gg \Delta_\perp$. In this scenario, the total invariant mass is given by

$$M_X^2 = (k_1 + k_2)^2 = \frac{P_\perp^2}{\vartheta_1 \vartheta_2} \qquad \text{for 2 jets,} \tag{6.1}$$

which, when inserted in Eq. (3.7), leads to

$$\beta \simeq \frac{Q^2}{Q^2 + P_\perp^2/\vartheta_1\vartheta_2} = \frac{\bar{Q}^2}{\bar{Q}^2 + P_\perp^2}. \tag{6.2}$$

Recalling that $\bar{Q}^2 = \vartheta_1(1-\vartheta_1)Q^2$, it is clear that Eq. (6.2) is quadratic in ϑ_1, thus its solution in terms of the independent variables β and $P_\perp$ for values smaller than 1/2 is

$$\vartheta_1 = \vartheta_*(\beta, P_\perp) \equiv \frac{1}{2}\left(1 - \sqrt{1 - \frac{4\beta}{1-\beta}\frac{P_\perp^2}{Q^2}}\right). \tag{6.3}$$

In the same way, the second solution for values larger than 1/2 is equal to $1-\vartheta_*$. Due to the symmetry of the integrand in the cross section, Eq.(4.17), under the exchange $\vartheta_1 \leftrightarrow 1-\vartheta_1$, the current computation can be restricted to the solution in Eq.(6.3), with the final result multiplied by a factor of 2. The square root in the solution of ϑ_1 implies the upper limits

$$P_{\perp\star}^2 = \frac{1-\beta}{4\beta}\,Q^2 \qquad \text{or} \qquad \beta_\star = \frac{Q^2}{Q^2+4P_\perp^2}. \tag{6.4}$$

for the hard jet momentum (with given Q^2 and β), or equivalently, in the range of allowed values for β (with given Q^2 and $P_\perp^2$) respectively. This also reflects the fact that, when all other kinematic variables are fixed, large values of $P_\perp^2$ require a small β, meaning that the production of hard jets "consumes" part of the available rapidity interval.

The quantity $\bar{Q}^2$ can be also be expressed in terms of the variables $P_\perp^2$ and β, as we can see in Eq. (6.2), implying that in this context $\bar{Q}^2$ is independent of Q^2. Such a fact makes possible to use the notation

$$\bar{Q}^2 = \frac{\beta}{1-\beta}\,P_\perp^2 \equiv \mathcal{M}^2. \tag{6.5}$$

Making the replacements in Eq.(4.17), we can write the SIDDIS transverse cross section[1] as

$$\frac{\mathrm{d}\sigma^{\gamma_T^* A\to q\bar{q}X}}{\mathrm{d}^2\boldsymbol{P}\mathrm{d}^2\boldsymbol{\Delta}\,\mathrm{d}\ln 1/\beta} = \frac{S_\perp \alpha_{\mathrm{em}} N_c}{\pi^2} \sum e_f^2 \,\frac{1}{Q^2}\, \frac{1-\frac{2\mathcal{M}^2}{Q^2}}{\sqrt{1-\frac{4\mathcal{M}^2}{Q^2}}}\,\frac{\mathcal{Q}_{\mathrm{inc}}}{1-\beta}, \tag{6.6}$$

where $\mathcal{Q}_{\mathrm{inc}}$ is the semi-hard factor defined in Eq. (5.12), now expressed in terms of dummy variables of the present process as

$$\mathcal{Q}_{\mathrm{inc}} \equiv \frac{1}{2\pi}\int \frac{\mathrm{d}^2\boldsymbol{B}}{2\pi}\,\frac{\mathrm{d}^2\boldsymbol{r}}{2\pi}\,\frac{\mathrm{d}^2\bar{\boldsymbol{r}}}{2\pi}\, e^{-i\boldsymbol{\Delta}\cdot\boldsymbol{B}-i\boldsymbol{P}\cdot(\boldsymbol{r}-\bar{\boldsymbol{r}})}\,\frac{\boldsymbol{r}\cdot\bar{\boldsymbol{r}}}{r\bar{r}}\,\mathcal{M}^2K_1(\mathcal{M}r)\mathcal{M}^2K_1(\mathcal{M}\bar{r})\mathcal{W}_q(\boldsymbol{r},\bar{\boldsymbol{r}},\boldsymbol{B}). \tag{6.7}$$

Since $\mathcal{Q}_{\mathrm{inc}}$ does not depend on Q^2, the cross section is proportional to $1/Q^2$ only if $\mathcal{M}^2 \ll Q^2$, or equivalently, $P_\perp^2 \ll P_{\perp\star}^2$. Consequently, the solution in Eq. (6.3) inherently favors asymmetric pairs with $\vartheta_* \simeq \mathcal{M}^2/Q^2 \ll 1$. Put differently, this analysis illustrates that the leading twist result emerges when the final state is constrained to aligned jet configurations, where the fermion with fraction $1-\vartheta_*$ essentially carries the entirety of the longitudinal momentum q^+ of the virtual photon.

In this $\mathcal{M}^2 \ll Q^2$ limit, we shall further rewrite the cross section as

$$\frac{\mathrm{d}\sigma^{\gamma_T^* A\to q\bar{q}X}}{\mathrm{d}^2\boldsymbol{P}\mathrm{d}^2\boldsymbol{\Delta}\,\mathrm{d}\ln 1/\beta} = \frac{4\pi^2\alpha_{\mathrm{em}}}{Q^2}\sum e_f^2\, 2\,\frac{\mathrm{d}xq_{\mathbb{P}}^{\mathrm{inc}}(x,x_{\mathbb{P}},\boldsymbol{P},\boldsymbol{\Delta})}{\mathrm{d}^2\boldsymbol{P}\mathrm{d}^2\boldsymbol{\Delta}}\bigg|_{x=\beta}, \tag{6.8}$$

which exhibits TMD factorization and where we have introduced the (anti)quark incoherent DTMD

$$\frac{\mathrm{d}xq_{\mathbb{P}}^{\mathrm{inc}}(x,x_{\mathbb{P}},\boldsymbol{P},\boldsymbol{\Delta})}{\mathrm{d}^2\boldsymbol{P}\mathrm{d}^2\boldsymbol{\Delta}} \equiv \frac{S_\perp N_c}{4\pi^3}\,\frac{\mathcal{Q}_{\mathrm{inc}}(x,x_{\mathbb{P}},\boldsymbol{P},\boldsymbol{\Delta})}{2\pi(1-x)}. \tag{6.9}$$

The semi-hard factor $\mathcal{Q}_{\mathrm{inc}}$, given in the present case by Eq. (6.7), is viewed as a function of the rapidity related variables $x=\beta$ and $x_{\mathbb{P}}$ and the transverse momenta $\boldsymbol{P}$ and $\boldsymbol{\Delta}$. It is evident that besides the dependence on the magnitudes involved, $\mathcal{Q}_{\mathrm{inc}}$ can also depend on the scalar product $\boldsymbol{P}\cdot\boldsymbol{\Delta}$. However, in many cases, only $|t| = \Delta_\perp^2$ is measured, which eliminates any angular dependence.

[1] Notice that we have dropped the label D in the cross sections as was used in Chap. 4.

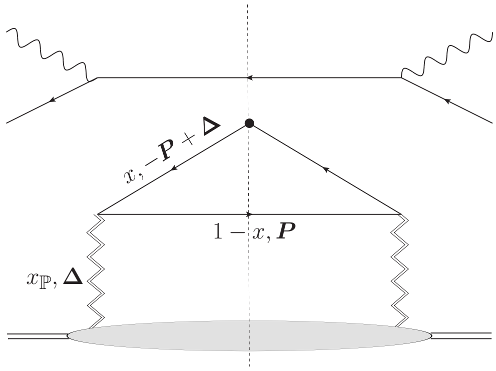

Figure 6.1: Pictorial representation of TMD factorization for incoherent diffractive processes in the $q\bar{q}$ contribution. The final evolution of the Pomeron consist in a quark-antiquark pair, where the quark carries a longitudinal fraction $1 - x$ and transverse momentum $\boldsymbol{P}$, appearing in the final state. The antiquark with fraction x and transverse momentum $-\boldsymbol{P} + \boldsymbol{\Delta}$ is absorbed by the virtual photon and brought on-shell.

At this point, it is instructive to compare our result with the coherent case, which was extensively analyzed in [60]. Upon integrating over $\boldsymbol{\Delta}$, Eqs. (6.8) and (6.9) become analogous to those in coherent diffraction, with the sole difference being the QCD correlator. As emphasized throughout this work, the incoherent diffractive correlator involves the connected piece shown in Eq. (6.7), whereas in the case of coherent diffraction, one simply replaces $\mathcal{W}_q$ with the factorized correlator $\langle T(\boldsymbol{r})\rangle \langle T(\bar{\boldsymbol{r}})\rangle$. For a homogeneous nucleus, this substitution leads to a complete factorization of the DA and CCA integrations, while the integration over $\boldsymbol{B}$ produces a δ-function in $\boldsymbol{\Delta}$. Consequently, after integrating over $\boldsymbol{\Delta}$, we recover the (anti)quark DTMD result in [60].

We now argue that the above result agrees with the following picture in the standard Bjorken frame and in the LC gauge $A^-_a = 0$, where the LCWF of the left-moving target is typically constructed. The Pomeron is interpreted as a colorless partonic fluctuation of the target, characterized by a small (minus) longitudinal fraction $x_{\mathbb{P}}$ and a transverse momentum $\boldsymbol{\Delta}$, which subsequently splits into a $q\bar{q}$ pair. One of the fermions, for instance the quark, carries a splitting fraction $1 - x$ and a transverse momentum $\boldsymbol{P}$, appearing in the final state. The other fermion, which carries a fraction x and a transverse momentum $-\boldsymbol{P}+\boldsymbol{\Delta}$, with $\Delta_\perp \ll P_\perp$ starts as a virtual particle and is only put on-shell after absorbing the virtual photon. Unlike in the coherent case where the momentum transfer is a non-perturbative scale, here $\Delta_\perp$ may reach the order of Q_s or be even larger. This description is correct if and only if $\vartheta_1 \ll 1$ and in this limit, the fraction x corresponds to the diffractive variable β in (6.2) which is the reason that justifies the choice of the variable x in Eq. (6.8). In Fig6.1 we provide an illustration of the TMD factorization just described. For a detailed discussion, see Section 2.4 in [60].

6.1.2 2+1 jets production

Rewriting Eq. (6.9) as

$$\frac{\mathrm{d}xq^{\mathrm{inc}}_{\mathbb{P}}(x, x_{\mathbb{P}}, \boldsymbol{k}_1, \boldsymbol{\Delta})}{\mathrm{d}^2\boldsymbol{k}_1\mathrm{d}^2\boldsymbol{\Delta}} \equiv \frac{S_\perp N_c}{4\pi^3}\,\frac{\mathcal{Q}_{\mathrm{inc}}(x, x_{\mathbb{P}}, \boldsymbol{k}_1, \boldsymbol{\Delta})}{2\pi(1-x)}, \tag{6.10}$$

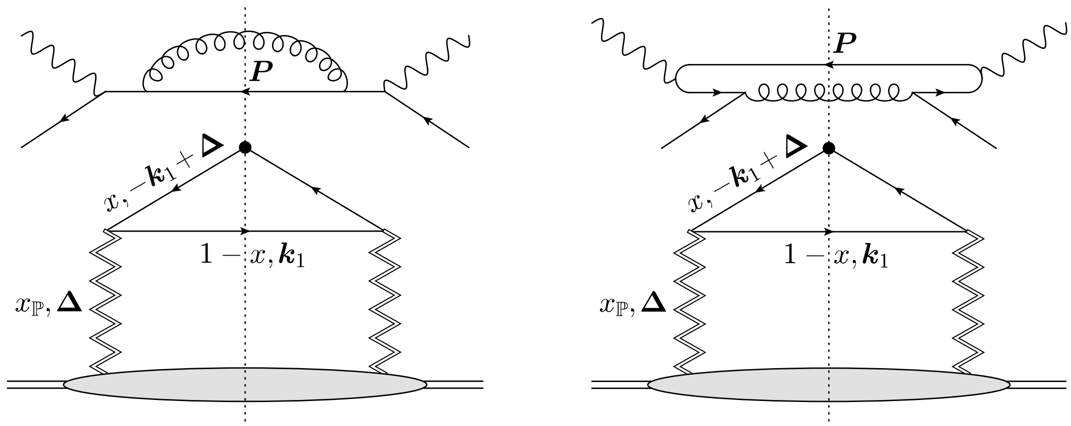

Figure 6.2: TMD factorization in incoherent diffractive production of a hard antiquark-gluon pair accompanied by a soft quark. Left panel: The antiquark emitted from the Pomeron absorbs the virtual photon, subsequently producing the hard pair. Right panel: The quark from the hard $q\bar{q}$ fluctuation of the virtual photon annihilates the antiquark emitted from the Pomeron, resulting in the production of a hard gluon. The corresponding interference diagram is not shown.

we readly see that the $2+1$ jets cross section in the soft quark sector, cf. Eq. (5.14), can be expressed as

$$\frac{\mathrm{d}\sigma^{\gamma_\lambda^* A\to(q)\bar{q}gX}}{\mathrm{d}\vartheta_2\,\mathrm{d}\vartheta_3\,\mathrm{d}^2\boldsymbol{P}\mathrm{d}^2\boldsymbol{\Delta}\,\mathrm{d}^2\boldsymbol{k}_1\,\mathrm{d}\ln 1/x} = 2\alpha_{\mathrm{em}}\alpha_s C_F \sum e_f^2\,\delta_\vartheta H_\lambda^{(q)}(\vartheta_2,\vartheta_3,P_\perp,\tilde{Q})\frac{\mathrm{d}xq_{\mathbb{P}}^{\mathrm{inc}}(x,x_{\mathbb{P}},\boldsymbol{k}_1,\boldsymbol{\Delta})}{\mathrm{d}^2\boldsymbol{k}_1\mathrm{d}^2\boldsymbol{\Delta}}. \tag{6.11}$$

Once more, we can interpret this as taking a fermion, say a quark, from the projectile LCWF and identified it as part of the Pomeron since it is soft. The Pomeron splits into a $q\bar{q}$ pair, where the quark carries a splitting fraction $1-x$ and transverse momentum $\boldsymbol{k}_1$ and appears in the final state, while the antiquark carries a fraction x and transverse momentum $-\boldsymbol{k}_1+\boldsymbol{\Delta}$. These are transferred to the hard $\bar{q}g$ pair, putting it on-shell. This interpretation, along with the TMD factorization in Eq.(6.11), is depicted in Fig.6.2.

In an analogous way in the soft gluon sector, by using the appropriate color factor and the semi-hard $\mathcal{G}_{\mathrm{inc}}$ given in Eq. (5.6), we define the incoherent gluon DTMD

$$\frac{\mathrm{d}xG_{\mathbb{P}}^{\mathrm{inc}}(x,x_{\mathbb{P}},\boldsymbol{k}_3,\boldsymbol{\Delta})}{\mathrm{d}^2\boldsymbol{k}_3\mathrm{d}^2\boldsymbol{\Delta}} \equiv \frac{S_\perp(N_c^2-1)}{4\pi^3}\,\frac{\mathcal{G}_{\mathrm{inc}}(x,x_{\mathbb{P}},\boldsymbol{k}_3,\boldsymbol{\Delta})}{2\pi(1-x)}. \tag{6.12}$$

Hence, we can express the respective cross section in the form

$$\frac{\mathrm{d}\sigma^{\gamma_\lambda^* A\to q\bar{q}(g)X}}{\mathrm{d}\vartheta_1\,\mathrm{d}\vartheta_2\,\mathrm{d}^2\boldsymbol{P}\mathrm{d}^2\boldsymbol{\Delta}\,\mathrm{d}^2\boldsymbol{k}_3\,\mathrm{d}\ln 1/x} = \alpha_{\mathrm{em}}\alpha_s \sum e_f^2\,\delta_\vartheta\,H_\lambda^{(g)}(\vartheta_1,\vartheta_2,P_\perp,\bar{Q})\,\frac{\mathrm{d}xG_{\mathbb{P}}^{\mathrm{inc}}(x,x_{\mathbb{P}},\boldsymbol{k}_3,\boldsymbol{\Delta})}{\mathrm{d}^2\boldsymbol{k}_3\mathrm{d}^2\boldsymbol{\Delta}}, \tag{6.13}$$

where the hard factors are given in Eqs. (5.2) and (5.9) for the transverse and longitudinal polarizations respectively. It is clear that a similar interpretation as the one for the quark DTMD can be given. In this case we are able to take a gluon from the projectile LCWF and interpret it as part of the Pomeron. The Pomeron splits into a pair of gluons, one carrying a

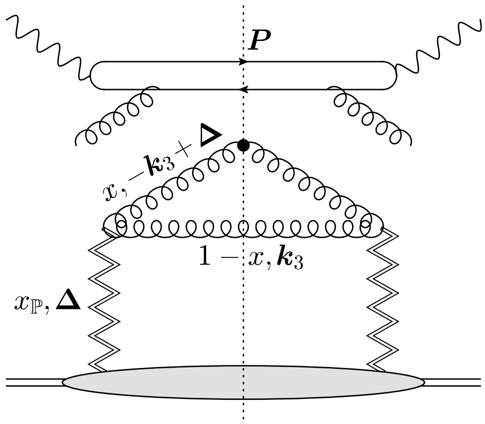

Figure 6.3: TMD factorization in incoherent diffractive production of a hard quark-antiquark pair accompanied by a soft gluon. The gluon emitted from the Pomeron is absorbed by the antiquark from the hard $q\bar{q}$ fluctuation of the virtual photon. Similar diagrams can be given for the case in which the gluon is absorbed by the quark and for the interference term.

fraction $1 - x$ and transverse momentum $\boldsymbol{k}_3$ and appears in the final state. The other gluon carries a fraction x and transverse momentum $-\boldsymbol{k}_3 + \boldsymbol{\Delta}$ which are transferred to the small $q\bar{q}$ dipole and put it on-shell. These features are illustrated in Fig. 6.3.

6.2 Analysis of the incoherent DTMDs and DPDFs

This section is dedicated to the study of the dependence of the incoherent gluon and quark DTMDs on the various variables. In particular, we are interested on how they depend on the transverse momentum $\boldsymbol{k}$ of the semi-hard parton (denoted by $\boldsymbol{k}_3$ for the gluon in Eq. (6.12) and by $\boldsymbol{k}_1$ for the quark in Eq. (6.10)) and on the splitting fraction x. Furthermore, we shall perform an integration over the semi-hard jet momentum to get the incoherent gluon and quark DPDFs. In fact, the integration over the kinematics of the soft jet in each of the 2+1 jets cross sections, derived in Chapter 5, will let us make a direct comparison between such cross sections and the exclusive two jets cross sections presented in Chapter 4. This comparison is indeed one of the main goals of the present work and will be presented in Chapter 7.

6.2.1 Incoherent DTMDs

As clearly seen from the quark and gluon TMD definitions in Eqs. (6.9) and (6.12), it suffices to study the functions $\mathcal{Q}_{\text{inc}}(x, x_{\mathbb{P}}, \boldsymbol{k}, \boldsymbol{\Delta})$ and $\mathcal{G}_{\text{inc}}(x, x_{\mathbb{P}}, \boldsymbol{k}, \boldsymbol{\Delta})$ given in (5.12) and Eqs. (5.6) respectively. The angle between the momenta $\boldsymbol{\Delta}$ and $\boldsymbol{k}$ is not interesting for our purposes and we will assume from now on that its integration is already performed. Hence, the DTMDs now depend only on the corresponding magnitudes. In this analysis we are interested on the dependence on the semi-hard momentum $k_\perp$, so we shall take $\Delta_\perp$ to have values of the order of the saturation scale Q_s. Nevertheless, when considering the incoherent DPDFs we will provide an extensive analysis of the $\Delta_\perp$-dependence.

As discussed at the end of Section 3.1.1, $x_{\mathbb{P}}$ sets the scale at which the CGC correlators $\mathcal{W}_g$ and $\mathcal{W}_q$ should be evaluated, with their relative dependence coming mainly through $Q_s(x_{\mathbb{P}})$.

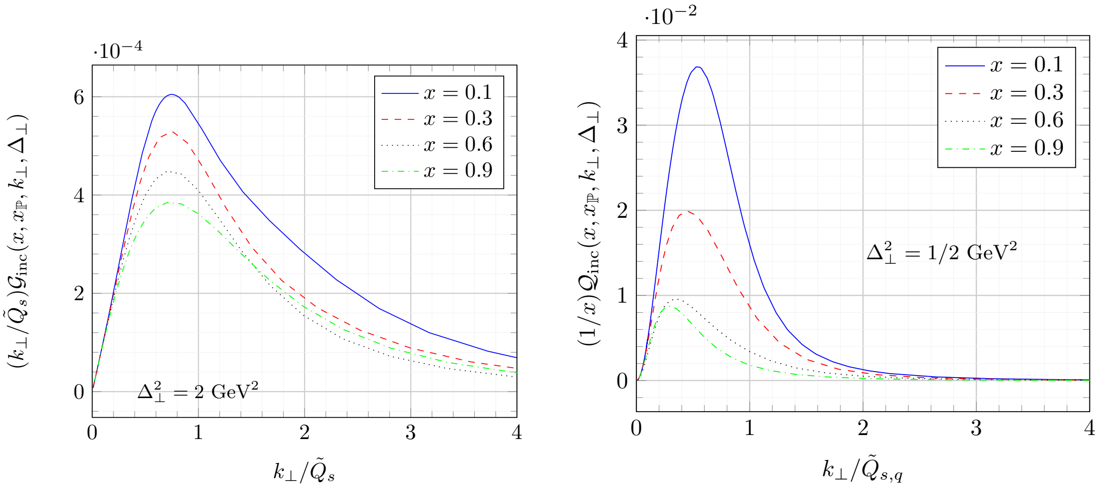

Figure 6.4: Left panel: The function $\mathcal{G}_{\rm inc}(x, x_{\mathbb{P}}, k_\perp, \Delta_\perp)$, which appears in the definition of the incoherent gluon DTMD in Eq. (6.12), multiplied with $k_\perp/\tilde{Q}_s(x)$ and plotted in terms of $k_\perp/\tilde{Q}_s(x)$ for fixed $\Delta_\perp$ and for various values of x. Right panel: The function $\mathcal{Q}_{\rm inc}(x, x_{\mathbb{P}}, k_\perp, \Delta_\perp)$, appearing in the definition of the incoherent quark DTMD in Eq. (6.10), multiplied with the factor $1/x$ and plotted in terms of $k_\perp/\tilde{Q}_{s,q}(x)$ for fixed $\Delta_\perp$ and for various values of x. In both cases an average over the angle between $\boldsymbol{k}$ and $\boldsymbol{\Delta}$ has been performed and the scattering amplitude is given by the MV model at $x_{\mathbb{P}} \simeq 10^{-2}$ with a gluon saturation scale $Q_s^2 = 2\,\mathrm{GeV}^2$.

However, $Q_s(x_{\mathbb{P}})$ is not precisely the relevant saturation scale when considering the momentum $k_\perp$. The exponentially decaying Bessel functions $K_2(\mathcal{M}R)$ and $K_1(\mathcal{M}R)$, along with the oscillatory behavior from the Fourier transform, suggest that the effective maximum size R scales as $R^2_{\rm max} \sim (1-x)/k_\perp^2$ [52, 55, 60]. Physically, this implies that the formation of a soft parton with transverse momentum $k_\perp$ remains incomplete when x is not very small and becomes strongly suppressed when $1 - x \ll 1$. The integration becomes sensitive to unitarity corrections in the correlators $\mathcal{W}_g$ and $\mathcal{W}_q$ only if $R^2_{\rm max} \sim 1/Q_s^2(x_{\mathbb{P}})$, which corresponds to $k_\perp^2 \sim \tilde{Q}_s^2(x, x_{\mathbb{P}})$, where we define the effective gluon saturation momentum [52, 55, 60]

$$\tilde{Q}_s^2(x, x_{\mathbb{P}}) \equiv (1-x)Q_s^2(x_{\mathbb{P}}). \tag{6.14}$$

A completely analogous relation can be formulated for the quark saturation scales $\tilde{Q}^2_{s,q}(x, x_{\mathbb{P}})$ and $Q^2_{s,q}(x_{\mathbb{P}})$.

Considering the correlators given in Eq. (F.2) and Eq. (F.4), with an analysis similar to the one performed in Section 4.2 within the MV model, by simple estimates it can be shown that for $k_\perp \gg \tilde{Q}_s$, both $\mathcal{G}_{\rm inc}$ and $\mathcal{Q}_{\rm inc}$ exhibit a power law tail of the type $\tilde{Q}_s^4/k_\perp^4$. On the other hand, in the limit $k_\perp \ll \tilde{Q}_s$ we find that $\mathcal{Q}_{\rm inc}$ vanishes, while $\mathcal{G}_{\rm inc}$ saturates, i.e. in this region $k_\perp \mathcal{G}_{\rm inc}$ goes linearly to zero; see the left panel of Fig. 6.4. We also point out that when $x \ll 1$, the Bessel functions in $\mathcal{Q}_{\rm inc}$ can be expanded for small arguments, i.e. $K_1(\mathcal{M}R) \simeq 1/\mathcal{M}R$ (and similarly for $K_1(\mathcal{M}\bar{R})$). From this, it is evident that $\mathcal{Q}_{\rm inc}$ scales as $\mathcal{M}^2 \propto x$ and thus vanishes linearly with x as x approaches zero. This behavior has also been observed in coherent diffraction [60]. In contrast, unlike in coherent diffraction, $\mathcal{G}_{\rm inc}$ and $\mathcal{Q}_{\rm inc}$ remain non-zero when $1 - x \ll 1$ (see the end of Appendix F for a technical explanation of this difference).

In summary, the qualitative behavior of $\mathcal{G}_{\rm inc}$ can be expressed as

$$\mathcal{G}_{\rm inc} \sim \frac{1}{\pi N_c^2 Q_s^2} \times \begin{cases} 1 & \text{for} \quad k_\perp \ll \tilde{Q}_s(x, x_{\mathbb{P}}), \\ \dfrac{\tilde{Q}_s^4(x, x_{\mathbb{P}})}{k_\perp^4} & \text{for} \quad k_\perp \gg \tilde{Q}_s(x, x_{\mathbb{P}}), \end{cases} \tag{6.15}$$

when the possible logarithmic dependence are neglected and for fixed values of $\Delta_\perp$. A similar expression can be given for $(1/x)\mathcal{Q}_{\rm inc}$, but as just discussed, it vanishes at small $k_\perp$. Another important characteristic visible in Eq. (6.15) is that as $\mathcal{G}_{\rm inc}$ and $\mathcal{Q}_{\rm inc}$ have mass dimension -2, when $\Delta_\perp \sim Q_s$, they are expected to scale as $1/Q_s^2$.

The above discussion indicates that both $k_\perp \mathcal{G}_{\rm inc}$ and $k_\perp \mathcal{Q}_{\rm inc}$ are expected to exhibit a distinct maximum at $k_\perp \sim \tilde{Q}_s$, followed by a relatively steep tail at higher momenta. This behavior is precisely what is observed in the numerical results shown in Fig. 6.4 for a fixed $\Delta_\perp$ of the order of the saturation momentum. Moreover, by numerical analysis we have confirmed that these properties hold for various values of $\Delta_\perp$. The primary effect of increasing $\Delta_\perp$ is a gradual shift of the entire spectrum towards larger momenta; however, this shift occurs very slowly and is not important for the purposes of this study.

6.2.2 Incoherent DPDFs

By integrating the DTMDs over the transverse momentum up to the scale of interest, which in this study amounts to the hard momentum $P_\perp$, we define the corresponding DPDFs. Hence, considering the incoherent gluon DPDF we have

$$\frac{\mathrm{d}xG_{\mathbb{P}}^{\rm inc}(x, x_{\mathbb{P}}, P_\perp, \Delta_\perp)}{\mathrm{d}^2\boldsymbol{\Delta}} \equiv \int^{P_\perp} \mathrm{d}^2\boldsymbol{k}\, \frac{\mathrm{d}xG_{\mathbb{P}}^{\rm inc}(x, x_{\mathbb{P}}, \boldsymbol{k}, \boldsymbol{\Delta})}{\mathrm{d}^2\boldsymbol{k}\mathrm{d}^2\boldsymbol{\Delta}} = \frac{S_\perp(N_c^2-1)}{4\pi^3} \int^{P_\perp} \mathrm{d}^2\boldsymbol{k}\, \frac{\mathcal{G}_{\rm inc}(x, x_{\mathbb{P}}, \boldsymbol{k}, \boldsymbol{\Delta})}{2\pi(1-x)} \tag{6.16}$$

and similarly for the quark one with the color factor being N_c.

Based on the high-momentum behavior of the DTMDs as described in Eq.(6.15), integrating to infinity in Eq.(6.16) requires subtracting a correction term that decreases as $1/P_\perp^2$. This weak dependence can be neglected, as it has been systematically done to corrections of this order throughout this work when assuming that $k_\perp, Q_s, \Delta_\perp \ll P_\perp$. It is also important to notice that logarithmic corrections, which are slightly more significant, may arise from DGLAP evolution between the semi-hard scale Q_s and the hard scale $P_\perp$. In references [52, 55, 56, 60] this fact is discussed in detail. While such corrections should, in principle be included in the incoherent case as well, the observable of interest in this work, which will be given in Sect. 7, has little sensitivity to the changes due to DGLAP evolution. Indeed, such an observable will be found to be dominated by values of x around one half, a regime in which DGLAP is not very significant. Therefore, although this is not strictly accurate, the DPDFs are treated as $P_\perp$-independent in this study.

We then proceed by pointing out that the $k_\perp$-integration is dominated by values in the regime $k_\perp \sim \tilde{Q}_s$ and introduces a factor $\tilde{Q}_s^2 = (1-x)Q_s^2$. This factor cancels the $1/Q_s^2$ prefactor in Eq.(6.15) as well as the $1/(1-x)$ factor in the DTMD definitions in Eqs.(6.12) and (6.10). Furthermore, the incoherent quark DPDF inherits a factor proportional to x from the respective DTMD.

A complete analysis of the gluon DPDF is given in Appendix F in the regimes $\Delta_\perp \ll Q_s$ and $\Delta_\perp \gg Q_s$ and close to the end-points $x = 0$ and $x = 1$. There we have employed the

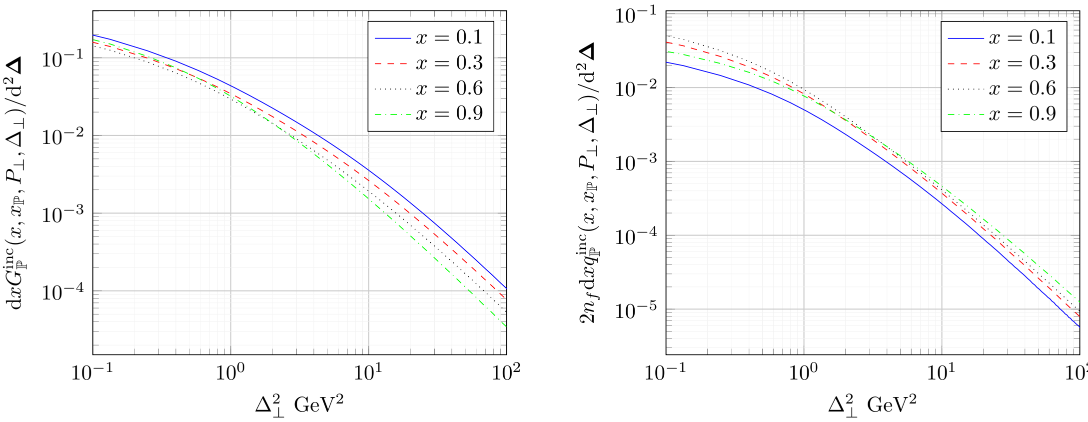

Figure 6.5: The incoherent gluon (left panel) and quark (right panel) DPDFs (the latter multiplied by $2n_f$, where $n_f = 3$ is the number of flavors) are shown as functions of the momentum transfer $\Delta_\perp^2$ for various values of x. The hard scale $P_\perp^2$ is assumed to be infinite, as discussed below Eq. (6.16). The scattering amplitude is given by the MV model with a gluon saturation scale $Q_s^2 = 2\mathrm{GeV}^2$, and a factor $S_\perp/4\pi^3$ has been omitted.

Gaussian approximation in the large-N_c limit to express $\mathcal{W}_g$ in terms of $\mathcal{S}_g$ and then used the MV model. The functional similarity between $\mathcal{W}_g$ and $\mathcal{W}_q$, as shown in Eqs. (F.2) and (F.4), also allows us to easily understand the quark DPDF based on the gluon case. The precise analytical estimates in the aforementioned regimes are given in Eqs. (F.12), (F.16), (F.24) and (F.31). Here we simply show the qualitative behavior, neglecting some constant factors and logarithms. Roughly speaking, the analytical study shows that the DPDFs exhibit (logarithmic) saturation at small momenta, while at high momenta, the characteristic $Q_s^4/\Delta_\perp^4$ tail is observed. A bit more precisely, the two incoherent DPDFs can be expressed in the piecewise form

$$\frac{\mathrm{d}xG_{\mathbb{P}}^{\mathrm{inc}}(x, x_{\mathbb{P}}, P_\perp, \Delta_\perp)}{\mathrm{d}^2\boldsymbol{\Delta}}, \frac{N_c}{x}\frac{\mathrm{d}xq_{\mathbb{P}}^{\mathrm{inc}}(x, x_{\mathbb{P}}, P_\perp, \Delta_\perp)}{\mathrm{d}^2\boldsymbol{\Delta}} \sim \frac{S_\perp}{8\pi^4} \times \begin{cases} \ln \dfrac{Q_s^2(x_{\mathbb{P}})}{\Lambda^2} & \text{for} \quad \Delta_\perp \ll Q_s(x_{\mathbb{P}}), \\ \dfrac{Q_s^4(x_{\mathbb{P}})}{\Delta_\perp^4} & \text{for} \quad \Delta_\perp \gg Q_s(x_{\mathbb{P}}). \end{cases} \tag{6.17}$$

Notice that $Q_s(x_{\mathbb{P}})$ is the appropriate saturation scale when we study the $\Delta_\perp$-dependence. The numerical results shown in Figs. 6.5 and 6.6 confirm all the previously discussed features concerning the dependence of the DPDFs on both $\Delta_\perp$ and x.

We would like to conclude this chapter by emphasizing that in the standard approach [127] the TMDs are defined through gauge-invariant field correlators, which are generally non-perturbative quantities. In the small-x limit, these reduce to correlators of Wilson lines, as discussed in Chap. 2, and the two approaches are shown to be consistent with each other [26, 27, 113]. In the saturation regime, the dynamical scale $Q_s \gg \Lambda$ emerges, allowing the problem to be addressed using weak-coupling methods. Consequently, the CGC approach employed in this work offers a means to calculate these correlators from "first principles".

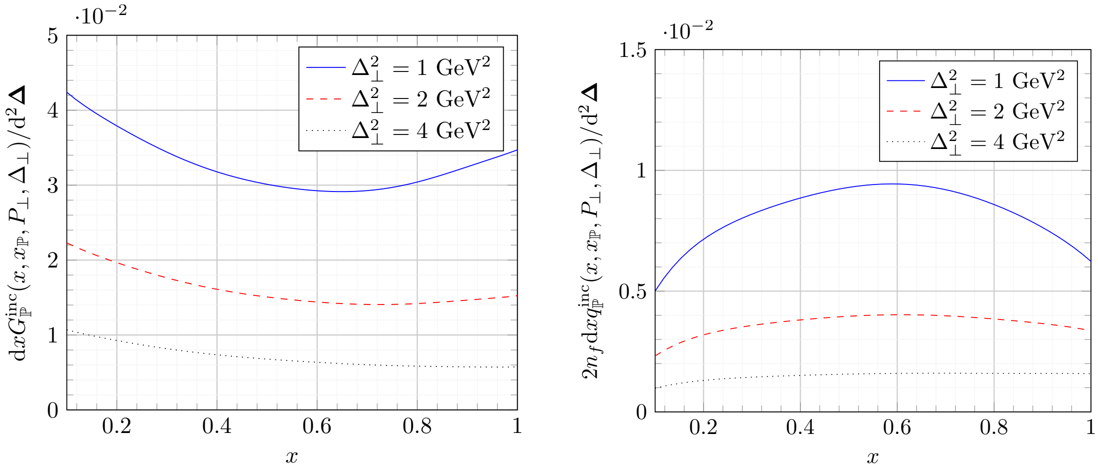

Figure 6.6: The incoherent gluon (left panel) and quark (right panel) DPDFs as functions of the splitting fraction x for various values of $\Delta_\perp^2$. The set of the plots is similar to the one for 6.5.

Chapter 7

Diffractive Dijet Production With a Minimum Rapidity Gap

Our goal here is to compare the 2 and 2+1 jets cross sections in the kinematics of interest. Hence, we should first integrate the transverse momentum of the semi-hard jet in the 2+1 jets cross sections given in Eqs. (6.13) and (6.11). This can be done by substituting the corresponding DTMDs with the DPDFs as shown in Eq. (6.16). It is also important to note that the minus longitudinal momentum splitting fraction x dependence in the 2+1 jets cross sections involves also the kinematics of the semi-hard jet. This means that such cross sections have different phase-space with respect to the 2 jets cross sections. We address this issue by imposing a minimum value for the rapidity gap $Y_{\mathbb{P}}$ in the diffractive process, irrespectively of the number of jets in the final state. We will find that this involves integrating the 2+1 jets cross section over x within a specific kinematical regime. We also remark that all the cross sections depend on the remaining variables $P_\perp$, $\Delta_\perp$ and the hard splitting fractions (where in fact only one of them is independent, since their sum is equal or approximately equal to one).

7.1 Minimum rapidity gap in the EIC

We consider s and Q^2 to be fixed, ensuring that the total available rapidity phase space, $Y_{\rm Bj} = \ln 1/x_{\rm Bj}$, also remains fixed. From Eq. (3.8), it follows that imposing a minimum value for $Y_{\mathbb{P}}$ (or equivalently, a maximum for $x_{\mathbb{P}}$) corresponds to setting a maximum value for Y_β (or a minimum for β), which defines the rapidity interval occupied by the projectile diffractive system. To be specific, let us assume a squared center-of-mass energy of $s = 8800\ \text{GeV}^2$, a value potentially achievable at the EIC in DIS off heavy nuclei, and a photon virtuality of $Q^2 = 20\ \text{GeV}^2$. These parameters yield $x_{\rm Bj} \simeq 2.3 \times 10^{-3}$, corresponding to $Y_{\rm Bj} \simeq 6.1$. We will examine two scenarios for the minimum rapidity gap as follows

$$Y_{\mathbb{P}}^{\rm min} \simeq 4.5 \ \Leftrightarrow\ x_{\mathbb{P}}^{\rm max} \simeq 1.1 \times 10^{-2} \quad | \quad Y_\beta^{\rm max} \simeq 1.6 \ \Leftrightarrow\ \beta_{\rm min} = 0.2 \tag{7.1}$$

and

$$Y_{\mathbb{P}}^{\rm min} \simeq 4 \ \Leftrightarrow\ x_{\mathbb{P}}^{\rm max} \simeq 1.8 \times 10^{-2} \quad | \quad Y_\beta^{\rm max} \simeq 2.1 \ \Leftrightarrow\ \beta_{\rm min} = 0.12. \tag{7.2}$$

These values indicate that saturation effects should be relevant as the CGC correlators must be computed at the longitudinal scale $x_{\mathbb{P}}$.

To be specific, and without loss of generality, we will assume that $\vartheta_{h1} = \vartheta_{h2} = 1/2$, where ϑ_{h1} and ϑ_{h2} represent the splitting fractions of the two forward hard jets. The remaining task is to analyze the cross sections as functions of the hard jet momentum $P_\perp^2$ and the semi-hard momentum transfer $\Delta_\perp^2$. To this end, it is necessary to see the implications of the minimum gap constraint for the 2 jets and $2+1$ jets configurations separately.

- **2 jets**: It is intuitively clear that as $P_\perp^2$ increases, the diffractive mass of the projectile system grows, leading to a reduction in the rapidity gap. More specifically, with all other kinematic variables already fixed, Eq. (6.2) implies that imposing a minimum rapidity gap translates into a maximum permissible value for the hard transverse momentum, i.e

$$P_{\perp\max}^2 = \frac{1-\beta_{\min}}{\beta_{\min}}\,\bar{Q}^2. \tag{7.3}$$

With $\vartheta_1 = \vartheta_2 = 1/2$ and $Q^2 = 20\,\mathrm{GeV}^2$, one has

$$P_{\perp\max}^2 = \begin{cases} 20\,\mathrm{GeV}^2 & \text{for} \quad \beta_{\min} = 0.2 \quad (Y_{\mathbb{P}} = 4.5) \\ 36.7\,\mathrm{GeV}^2 & \text{for} \quad \beta_{\min} = 0.12 \quad (Y_{\mathbb{P}} = 4). \end{cases} \tag{7.4}$$

Since we work in the regime where $\Delta_\perp^2 \ll P_\perp^2$, the preceding discussion for 2 jets and the subsequent analysis for $2+1$ jets are independent of the specific choice of $\Delta_\perp^2$.

- **2 + 1 jets**: The presence of a third jet implies that for a given $P_\perp^2$ the gap is not fixed. It is evident that for the same hard jet kinematics, the gap is smaller compared to the case with only 2 hard jets. This becomes apparent when examining the diffractive variable β, which can be expressed using Eq. (5.4) as

$$\beta = \frac{Q^2}{Q^2 + P_\perp^2/\vartheta_{h1}\vartheta_{h2} + k_\perp^2/\vartheta}, \tag{7.5}$$

where clearly $k_\perp^2$ and ϑ represent the transverse momentum and the splitting fraction of the semi-hard jet. From the last relation we observe that imposing a minimum value for β establishes a condition with a clear physical interpretation: the ratio $k_\perp^2/\vartheta$ should remain moderate, otherwise the semi-hard jet will excessively reduce the rapidity gap. Eq. (5.4) also guarantees that ϑ remains sufficiently small, consistent with the requirements of our approximation. This becomes evident when solving for ϑ, namely

$$\vartheta = \frac{x}{1-x}\,\frac{k_\perp^2}{Q^2 + P_\perp^2/\vartheta_{h1}\vartheta_{h2}} \sim \frac{xQ_s^2}{Q^2 + P_\perp^2/\vartheta_{h1}\vartheta_{h2}}, \tag{7.6}$$

where in the second expression we have used the fact that the $k_\perp$ spectrum has a maximum in the regime $k_\perp \sim \tilde{Q}_s$ (cf. Section 6.2.1), which controls the respective integration.

It is also clear in Eq. (5.4) that with all the variables fixed, a minimum value in β implies a minimum value in x, which is indeed the variable that we conveniently used to write our cross sections. Hence, the fraction x has a minimum value that reads

$$x_{\min} = \frac{Q^2 + P_\perp^2/\vartheta_{h1}\vartheta_{h2}}{Q^2}\,\beta_{\min}, \tag{7.7}$$

while its maximum value is one. By setting $x_{\min} = 1/2$ we can define a "typical" hard jet momentum, which reads

$$P_{\perp\text{typ}}^2 = \begin{cases} 7.5\,\text{GeV}^2 & \text{for} \quad \beta_{\min} = 0.2 \quad (Y_{\mathbb{P}} = 4.5) \\ 18.3\,\text{GeV}^2 & \text{for} \quad \beta_{\min} = 0.12 \quad (Y_{\mathbb{P}} = 4). \end{cases} \tag{7.8}$$

These hard momenta are, as intended, significantly above the saturation momentum Q_s^2 and well below the corresponding maximum values given in Eq. (7.4).

Taking all the above considerations into account, we shall present the results of our numerical calculations for $P_\perp^2$ ranging from $2Q_s^2$ to values approaching $P_{\perp\max}^2$, while noting that accuracy may decrease near the endpoints. For the smaller values of $P_\perp^2$, neglected saturation corrections of the order $Q_s^2/P_\perp^2$ or higher can become significant. Conversely, for $P_\perp^2$ close to $P_{\perp\max}^2$, the phase space available for the production of the semi-hard jet approaches to zero.

7.2 On the evolution of the CGC correlators

The CGC correlators $\mathcal{W}_g$ and $\mathcal{W}_q$ should be evaluated at the scale $Y_{\mathbb{P}}$, which with the help of Eqs. (3.8) and (5.4) reads

$$Y_{\mathbb{P}} = Y_{\text{Bj}} - \ln \frac{Q^2 + P_\perp^2/\vartheta_{h1}\vartheta_{h2}}{xQ^2}, \tag{7.9}$$

where for the 2 jets case, $x = 1$. In our observable we have fixed Q^2, Y_{Bj} and the hard jet splitting fractions ϑ_{h1} and ϑ_{h2}, however, the gap described in Eq. (7.9) may still vary with the hard jet momentum $P_\perp^2$ and/or the fraction x. A numerical evaluation that takes into account such a variation is feasible, although highly more complicated. Here instead, we argue that it is not necessary to do so, by showing that the dependence on $P_\perp^2$ via the floating $Y_{\mathbb{P}}$ is subdominant.

The QCD correlators depend on $Y_{\mathbb{P}}$ via the ratio $\Delta_\perp^2/Q_s^2(Y_{\mathbb{P}})$, thus one has

$$\Delta\mathcal{W} \simeq \frac{\mathrm{d}\mathcal{W}(\Delta_\perp^2/Q_s^2(Y_{\mathbb{P}}))}{\mathrm{d}Y_{\mathbb{P}}}\,\Delta Y_{\mathbb{P}} \simeq \frac{\mathrm{d}\mathcal{W}(\Delta_\perp^2/Q_s^2(Y_{\mathbb{P}}))}{\mathrm{d}\ln Q_s^2(Y_{\mathbb{P}})/\Delta_\perp^2}\,\frac{\mathrm{d}\ln Q_s^2(Y_{\mathbb{P}})}{\mathrm{d}Y_{\mathbb{P}}}\,\Delta Y_{\mathbb{P}}. \tag{7.10}$$

The first factor in the last expression is of $\mathcal{O}(1)$, as we focus on a semi-hard momentum transfer $\Delta_\perp^2 \sim Q_s^2$. The second factor, which governs the growth of the saturation momentum, is proportional to α_s and is estimated to be approximately 0.25 [7, 8]. The final factor encodes the $P_\perp^2$ dependence and can be straightforwardly determined using the explicit expression in Eq. (7.9). By inspecting the 2 jets case, we find that such a variation at $Y_{\mathbb{P}}^{\min}$ behaves as

$$\Delta\mathcal{W} \sim \alpha_s \ln \frac{Q^2 + P_{\perp\max}^2/\vartheta_{h1}\vartheta_{h2}}{Q^2 + P_\perp^2/\vartheta_{h1}\vartheta_{h2}}. \tag{7.11}$$

It is evident that the power-law dependence of the cross sections through the hard factors is much stronger than the logarithmic behavior in Eq. (7.11). Clearly, the analysis is similar for the 2 + 1 jets cross sections. Therefore, we shall neglect the $P_\perp$-dependence in our subsequent analysis, by computing the correlators at $Y_{\mathbb{P}}^{\min}$.

Now we focus on the $Y_{\mathbb{P}}^{\min}$-dependence in the QCD correlators. In general, in the standard approach, as discussed in Chapter 2 and performed in Section 4.4, one assumes that the scattering amplitude is initially described by the MV model at a given Y_0 and then evolves to the scale

$Y_{\mathbb{P}}^{\min}$ using the collinearly improved BK equation [99, 119, 120]. However, since the evolution between the two rapidities specified in Eqs.(7.1) and (7.2) — which differ by only half a unit — is not expected to produce significant changes in the amplitude, and given that the corresponding $x_{\mathbb{P}}$ values are approximately 10^{-2}, we adopt the MV model for the amplitude in both cases, but with distinct saturation scales. By fixing $Q_s^2 = 2$ GeV^2 at $Y_{\mathbb{P}}^{\min} = 4.5$, the growth law for the saturation momentum (see the discussion above Eq. (7.11)) suggests setting $Q_s^2 = 1.76$ GeV^2 for $Y_{\mathbb{P}}^{\min} = 4$.

7.3 Comparison of the cross sections

We are now prepared to present the final form of the diffractive cross sections relevant to this study. The expression for the 2-jet case is the one provided in Eq.(4.59) together with Eqs. (4.45) and (4.48). As discussed in Section 4.4, the averaged cross section is dominated by the term proportional to $\mathcal{G}_{\rm D}^{(+)}(\Delta_\perp)$, while the one proportional to $\mathcal{G}_{\rm D}^{(-)}(\Delta_\perp)$ can be neglected since it is both parametrically and numerically small. Hence, we rewrite here the 2 jets cross section[1] of interest as

$$\frac{\mathrm{d}\sigma^{\gamma_\lambda^* A\to q\bar{q}X}}{\mathrm{d}\Pi} \simeq \frac{S_\perp \alpha_{\rm em}\, N_c}{4\pi^3} \sum e_f^2\, \delta_\vartheta\, \frac{2C_F}{N_c^3}\, H_\lambda(\vartheta_1,\vartheta_2,P_\perp,\bar{Q})\, \mathcal{G}^{(+)}(\Delta_\perp), \tag{7.12}$$

with $C_F = (N_c^2-1)/2N_c$ and where we recall the shorthand notation $\mathrm{d}\Pi = (2\pi)^2 P_\perp \mathrm{d}P_\perp \Delta_\perp \mathrm{d}\Delta_\perp \mathrm{d}\vartheta_1 \mathrm{d}\vartheta_2$. We also rewrite here the transverse (T) and longitudinal (L) hard factors in the form

$$H_T(\vartheta_1,\vartheta_2,P_\perp,\bar{Q}) = \left(\vartheta_1^2+\vartheta_2^2\right) \frac{P_\perp^2(3\bar{Q}^4+P_\perp^4)}{(P_\perp^2+\bar{Q}^2)^6}, \tag{7.13}$$

$$H_L(\vartheta_1,\vartheta_2,P_\perp,\bar{Q}) = \vartheta_1\vartheta_2\, \frac{2\bar{Q}^2(\bar{Q}^4-2\bar{Q}^2P_\perp^2+5P_\perp^4)}{(P_\perp^2+\bar{Q}^2)^6}. \tag{7.14}$$

For the $2+1$ jets we simply integrate Eqs. (6.13) and (6.11) over the semi-hard jet kinematics to find

$$\frac{\mathrm{d}\sigma^{\gamma_\lambda^* A\to q\bar{q}(g)X}}{\mathrm{d}\Pi} = \alpha_{\rm em}\alpha_s \sum e_f^2\, \delta_\vartheta\, H_\lambda^{(g)}(\vartheta_1,\vartheta_2,P_\perp,\bar{Q}) \int_{x_{\min}}^1 \frac{\mathrm{d}x}{x}\, \frac{\mathrm{d}xG_{\mathbb{P}}^{\rm inc}(x,x_{\mathbb{P}},P_\perp,\Delta_\perp)}{\mathrm{d}^2\boldsymbol{\Delta}}, \tag{7.15}$$

and

$$\frac{\mathrm{d}\sigma^{\gamma_\lambda^* A\to (q)\bar{q}gX}}{\mathrm{d}\Pi} = 2\alpha_{\rm em}\alpha_s C_F \sum e_f^2\, \delta_\vartheta\, H_\lambda^{(q)}(\vartheta_1,\vartheta_2,P_\perp,\tilde{Q}) \int_{x_{\min}}^1 \frac{\mathrm{d}x}{x}\, \frac{\mathrm{d}xq_{\mathbb{P}}^{\rm inc}(x,x_{\mathbb{P}},P_\perp,\Delta_\perp)}{\mathrm{d}^2\boldsymbol{\Delta}}, \tag{7.16}$$

with $x_{\min}$ as defined in Eq.(7.7) and where all cross sections should be considered up to a maximum hard jet momentum satisfying Eq.(7.4). We shall work in the large-N_c limit, hence we set $C_F \to N_c/2$ in Eqs.(7.12) and (7.16), replace $N_c^2-1 \to N_c^2$ in Eq.(6.16) for the gluon DPDF, and use Eqs. (F.2) and (F.4) to determine the scattering correlators $\mathcal{W}_g$ and $\mathcal{W}_q$. The QCD running coupling is evaluated at the hard scale $P_\perp^2$, and at one-loop accuracy, it is given by Eq. (1.8), which we rewrite here for convenience as

$$\alpha_s\left(P_\perp^2\right) = \frac{1}{b\ln P_\perp^2/\Lambda^2} \qquad \text{with} \qquad b = \frac{11N_c-2n_f}{12\pi}. \tag{7.17}$$

[1] As in Eq. (6.6), we have dropped the label D in the cross section and in the semi-hard factor as well.

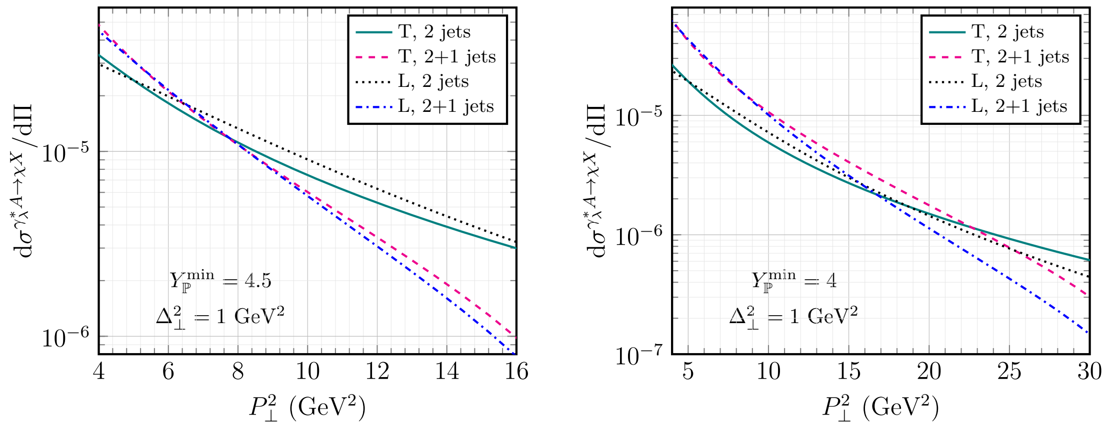

Figure 7.1: The transverse and longitudinal cross sections for the production of incoherent diffractive 2 jets and $2+1$ jets as functions of the hard jet momentum $P_\perp^2$ for fixed momentum transfer $\Delta_\perp^2$ and for $Y_{\mathbb{P}}^{\min} = 4.5$ (left panel) or $Y_{\mathbb{P}}^{\min} = 4$ (right panel). The remaining independent kinematic variables are fixed according to $x_{\rm Bj} = 2.3\times 10^{-3}$, $Q^2 = 20\,\mathrm{GeV}^2$ and $\vartheta_{h1} = \vartheta_{h2} = 1/2$. The scattering amplitude is given by the MV model and a factor $\alpha_{\rm em}(S_\perp/4\pi^3)\delta_\vartheta$ has been omitted.

It is equally probable to produce either a soft quark or a soft antiquark, thus the total $2+1$ jets cross section is given by

$$\frac{d\sigma^{\gamma_\lambda^* A\to q\bar{q}gX}}{d\Pi} = \frac{d\sigma^{\gamma_\lambda^* A\to q\bar{q}(g)X}}{d\Pi} + 2\,\frac{d\sigma^{\gamma_\lambda^* A\to (q)\bar{q}gX}}{d\Pi}. \tag{7.18}$$

The study of the parametric behavior of the cross sections is easily done by seeing the explicit exact expressions for the hard factors in Eqs. (7.13), (7.14), (5.2), (5.9), (5.10) and (5.15), the estimates for $\mathcal{G}^{(+)}(\Delta_\perp)$ in the cases shown in Eqs. (4.53), (4.54) and (4.55), as well as the incoherent DPDFs in Eq. (6.17). Assuming that $\bar{Q},\tilde{Q} \sim P_\perp$ and by neglecting some constant factors and logarithms we find for 2 jets

$$\frac{d\sigma^{\gamma_\lambda^* A\to q\bar{q}X}}{d\Pi} \sim \frac{S_\perp \alpha_{\rm em}}{4\pi^3 N_c}\sum e_f^2\,\delta_\vartheta\,\frac{Q_s^2}{P_\perp^6}\times\begin{cases}\ln\dfrac{Q_s^2}{\Lambda^2} & \text{for}\quad \Delta_\perp \ll Q_s,\\[2mm] \dfrac{Q_s^2}{\Delta_\perp^2} & \text{for}\quad \Delta_\perp \gg Q_s,\end{cases} \tag{7.19}$$

and for $2+1$ jets

$$\frac{d\sigma^{\gamma_\lambda^* A\to q\bar{q}gX}}{d\Pi} \sim \frac{S_\perp \alpha_{\rm em}}{4\pi^3 N_c}\sum e_f^2\,\delta_\vartheta\,\frac{\alpha_s N_c}{\pi}\,\frac{1}{P_\perp^4}\times\begin{cases}\ln\dfrac{Q_s^2}{\Lambda^2} & \text{for}\quad \Delta_\perp \ll Q_s,\\[2mm] \dfrac{Q_s^4}{\Delta_\perp^4} & \text{for}\quad \Delta_\perp \gg Q_s,\end{cases} \tag{7.20}$$

where the soft gluon and soft quark sectors are of the same order. This means that the cross sections saturate logarithmically for $\Delta_\perp \ll Q_s$ as well. One observes that the $2+1$ jets cross section is parametrically larger in the regime $\Delta_\perp \lesssim Q_s$ by a factor $\alpha_s P_\perp^2/Q_s^2$ and also when $Q_s^2 \ll \Delta_\perp^2 \ll P_\perp^2$ by a factor $\alpha_s P_\perp^2/\Delta_\perp^2$. Another important remark is that such a dominant contribution exhibits a natural $1/\Delta_\perp^4 = 1/|t|^2$ tail at large $|t|$.

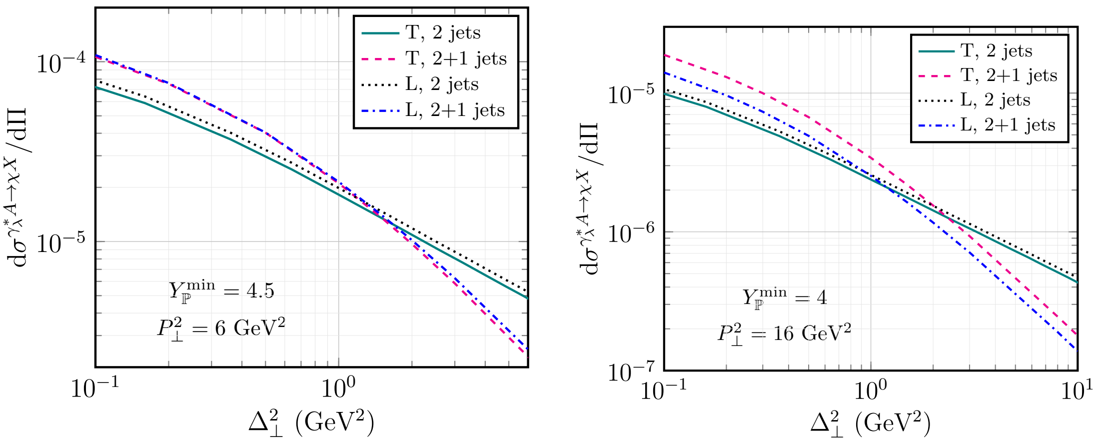

Figure 7.2: The transversely and longitudinally polarized cross sections for incoherent diffractive production of 2 jets and $2+1$ jets as functions of the momentum transfer $\Delta_\perp^2$ for fixed hard jet momentum $P_\perp^2$. The rest is as in Fig. 7.1.

Finally, we have numerically computed the cross sections presented in Eqs.(7.12) and (7.18), and shown them in Fig.7.1 as functions of $P_\perp^2$. Again, the momentum transfer $\Delta_\perp^2$ is fixed and assumed to be of the order of Q_s^2. The selected kinematic variables are realistic as presented in Section 7.1, though we are not strictly within the regime where the parametric estimates outlined earlier are fully applicable. As a consequence, the $2+1$ jet contributions do not dominate the cross section. However, we observe that their contribution remains larger than that of the two-jet process up to a certain value of the hard jet momentum, which is approximately the typical value estimated in Eq.(7.8). Overall, the two contributions are of comparable magnitude across the entire range displayed in Fig.7.1.

It is also visible that, as discussed at the end of Section 7.1, when $P_\perp^2$ approaches its maximum value dictated in Eq.(7.4), the $2+1$ jets cross section vanishes since there is no phase-space for the emission of the third jet. This is explicitly seen in the interval of the integration in Eqs. (7.15) and (7.16), and it is the reason that one must not naively expect a favorable situation for $2+1$ jets at high $P_\perp^2$.

In a similar way, in Fig.7.2, we present the numerical results for the cross sections as functions of $\Delta_\perp^2$. The hard jet momentum $P_\perp^2$ is fixed and taken to be of the order of its typical value, which depends on $Y_{\mathbb{P}}^{\min}$, as indicated in Eq.(7.8). Once again, we observe that the two contributions are approximately of the same order across a broad range of momenta. With the chosen kinematics, the $2+1$ jet cross section remains larger than the two-jet cross section for momentum transfers up to the saturation scale.

Conclusions

We have studied the incoherent diffractive production of 2 and 2+1 jets in eA collisions. In both cases we work in the correlation limit, i.e. a specific kinematic regime in which there are two hard jets in the final state which are almost back-to-back in transverse space, having approximate transverse momenta $\boldsymbol{P}$ and $-\boldsymbol{P}$. Such a momentum $\boldsymbol{P}$ is *hard* when it is much larger than both the saturation scale and the momentum transfer, i.e. when $P_\perp \gg Q_s, \Delta_\perp$. No assumption has been made regarding the magnitude of $\Delta_\perp$ when compared to Q_s, hence inverse powers of $\Delta_\perp^2$ are resummed to all orders.

For the case of dijet production, at leading twist, we have separated the hard dynamics, i.e., the dependence on the relative momentum $P_\perp$ and $\bar{Q}$, from the semi-hard dynamics, which are governed by the imbalance $\Delta_\perp$. We then computed the first higher-order kinematic twist, corresponding to the correction of relative order $\Delta_\perp^2/P_\perp^2$. This approach allowed us to provide a reliable analytical description of the cross sections and azimuthal anisotropies, even in the regime where $\Delta_\perp$ — which represents both the dijet imbalance and the transverse momentum transferred from the nucleus — starts to become comparable to $P_\perp$.

We also found that, at leading twist, the dijet cross section exhibits a rapid decay with increasing hard jet momentum, specifically following a $1/P_\perp^6$ dependence. This behavior arises from the fact that the scattering process involves dipoles of small size. Furthermore, when analyzing the dependence on the momentum transfer, we obtained a rather unusual $1/\Delta_\perp^2 = 1/|t|$ fall-off for large values of $|t|$.

Following the approach used in the analogous problem of coherent diffraction [52, 55, 56, 60], we demonstrated that the leading contribution in power counting is given when the hard dijet is accompanied by a third, semi-hard jet. We expressed this $2+1$ cross section in a factorized form, as the product of a hard factor and either an incoherent quark or gluon DTMD (when the semi-hard jet is explicit), or the corresponding DPDF (when the semi-hard jet is integrated over). While this process is proportional to the running coupling $\alpha_s(P_\perp^2)$, which is small, the scattering is sensitive only to large-size configurations in the projectile wave function, leading to a hard factor in the $2+1$ jets cross section that falls off as $1/P_\perp^4$.

Additionally, we found that the quark and gluon DPDFs saturate logarithmically when $|t| \ll Q_s^2$ and show a natural $1/\Delta_\perp^4 = 1/|t|^2$ tail in the regime $Q_s^2 \ll |t| \ll P_\perp^2$. Finally, in contrast to the two-jet case [34, 63], we did not observe any dependence of the $2+1$ jets cross section on the angle between the hard jet momentum and the momentum transfer.

In order to compare the 2 jets and 2+1 jets cross sections we proceeded to impose a minimum value for the rapidity gap of the diffractive process by considering kinematics hopefully achievable at the future Electron-Ion Collider (EIC). We find that at sufficiently high energy collisions the 2+1 jets cross section dominates, while for the typical values expected at the EIC the two cross sections are of the same order. Hence, for practical purposes, it is important to consider both contributions.

This study assumes a partonic content in the outgoing state, therefore further work is required in order to compute the cross sections for producing real jets or hadrons.

Appendix A

Useful integrals

Here we provide some integrals useful to calculate the high-momentum behavior of the transverse momentum dependent quantities studied in this work. For instance, we consider the integral

$$\int_0^\infty \mathrm{d}\tilde{B}\,\tilde{B}^{1+2\gamma} J_0(\tilde{B}) = \frac{4^{\frac{1}{2}+\gamma}\Gamma(1+\gamma)}{\Gamma(-\gamma)} \tag{A.1}$$

which in general is valid for $-1 < \gamma < -1/2$. To calculate integrals involving a power of $\ln \tilde{B}^2$ we differentiate with γ and by analytic continuation we shall take Eq. (A.1) to be true for values of γ outside the aforementioned interval. One useful example for our purposes is

$$\int_0^\infty \mathrm{d}\tilde{B}\,\tilde{B}^3 \ln \tilde{B}^2\, J_0(\tilde{B}) = \lim_{\gamma\to 1} \frac{\mathrm{d}}{\mathrm{d}\gamma} \frac{4^{\frac{1}{2}+\gamma}\Gamma(1+\gamma)}{\Gamma(-\gamma)} = 8. \tag{A.2}$$

Similar integrations can be considered involving other Bessel functions, in particular we list the following

$$\int_0^\infty \mathrm{d}\tilde{B}\,\tilde{B} \ln \tilde{B}^2\, J_0(\tilde{B}) = -2, \tag{A.3}$$

$$\int_0^\infty \mathrm{d}\tilde{B}\,\tilde{B} \ln^2 \tilde{B}^2\, J_0(\tilde{B}) = 8(\gamma_E - \ln 2), \tag{A.4}$$

$$\int_0^\infty \mathrm{d}\tilde{B}\,\tilde{B}\, J_2(\tilde{B}) = 2, \tag{A.5}$$

$$\int_0^\infty \mathrm{d}\tilde{B}\,\tilde{B} \ln \tilde{B}^2\, J_2(\tilde{B}) = 2(2\ln 2 - 2\gamma_E + 1), \tag{A.6}$$

and

$$\int_0^\infty \mathrm{d}\tilde{B}\,\tilde{B}\, J_4(\tilde{B}) = 4, \tag{A.7}$$

where $\gamma_E \simeq 0.5772$ is the Euler's constant. For completeness, we would like to remind also here that

$$\int \frac{\mathrm{d}^2\boldsymbol{B}}{2\pi}\, e^{-i\boldsymbol{\Delta}\cdot\boldsymbol{B}} = \delta^{(2)}(\boldsymbol{\Delta}) \tag{A.8}$$

and so

$$\int \frac{\mathrm{d}^2\boldsymbol{B}}{2\pi}\, e^{-i\boldsymbol{\Delta}\cdot\boldsymbol{B}} B^2 = -\nabla^2_{\Delta} \int \frac{\mathrm{d}^2\boldsymbol{B}}{2\pi}\, e^{-i\boldsymbol{\Delta}\cdot\boldsymbol{B}} = -2\pi\nabla^2_{\Delta}\delta^{(2)}(\boldsymbol{\Delta}). \tag{A.9}$$

Appendix B

Tensor decompositions and contractions in the $q\bar{q}$ contribution

Starting from Eq. (4.35) (together with Eq. (4.37)), we find that the semihard factor admits a tensor decomposition, in which the coefficients are given by five different scalar quantities which depend only on the magnitude $\Delta_\perp$, namely

$$\begin{aligned}
\mathcal{G}_{\mathrm{D}}^{ij,kl}(\boldsymbol{\Delta}) = {} & \frac{\delta^{ij}}{2}\,\frac{\delta^{kl}}{2}\left[\mathcal{G}_{\mathrm{D}}^{(+)}(\Delta_\perp) - \frac{1}{2}\,\mathcal{G}_{\mathrm{D}}^{(-)}(\Delta_\perp)\right] + \left(\frac{\delta^{ik}}{2}\,\frac{\delta^{jl}}{2} + \frac{\delta^{il}}{2}\,\frac{\delta^{jk}}{2}\right)\frac{1}{2}\,\mathcal{G}_{\mathrm{D}}^{(-)}(\Delta_\perp) \\
& + \left(\frac{\delta^{ij}}{2}\hat{\Delta}^{kl} + \frac{\delta^{kl}}{2}\hat{\Delta}^{ij}\right)\left[\mathcal{G}_{\mathrm{D}}^{(1)}(\Delta_\perp) - \frac{2}{3}\,\mathcal{G}_{\mathrm{D}}^{(1')}(\Delta_\perp)\right] \\
& + \left(\frac{\delta^{ik}}{2}\hat{\Delta}^{jl} + \frac{\delta^{jl}}{2}\hat{\Delta}^{ik} + \frac{\delta^{il}}{2}\hat{\Delta}^{jk} + \frac{\delta^{jk}}{2}\hat{\Delta}^{il}\right)\frac{1}{3}\,\mathcal{G}_{\mathrm{D}}^{(1')}(\Delta_\perp) \\
& + \left(\hat{\Delta}^{ij}\hat{\Delta}^{kl} - \frac{1}{2}\,\frac{\delta^{ij}}{2}\,\frac{\delta^{kl}}{2} + \hat{\Delta}^{ik}\hat{\Delta}^{jl} - \frac{1}{2}\,\frac{\delta^{ik}}{2}\,\frac{\delta^{jl}}{2} + \hat{\Delta}^{il}\hat{\Delta}^{jk} - \frac{1}{2}\,\frac{\delta^{il}}{2}\,\frac{\delta^{jk}}{2}\right)\frac{1}{3}\,\mathcal{G}_{\mathrm{D}}^{(2)}(\Delta_\perp).
\end{aligned} \tag{B.1}$$

The traceless tensor $\hat{\Delta}^{ij}$ is defined as

$$\hat{\Delta}^{ij} \equiv \frac{\Delta^i\Delta^j}{\Delta_\perp^2} - \frac{\delta^{ij}}{2}, \tag{B.2}$$

while the functions involved in the coefficients read

$$\mathcal{G}_{\mathrm{D}}^{(+)}(\Delta_\perp) = \int \frac{\mathrm{d}^2\boldsymbol{B}}{2\pi}\, e^{-i\boldsymbol{\Delta}\cdot\boldsymbol{B}}\,\Phi(B)[F_+(B)]^2, \tag{B.3}$$

$$\mathcal{G}_{\mathrm{D}}^{(-)}(\Delta_\perp) = \int \frac{\mathrm{d}^2\boldsymbol{B}}{2\pi}\, e^{-i\boldsymbol{\Delta}\cdot\boldsymbol{B}}\,\Phi(B)[F_-(B)]^2, \tag{B.4}$$

$$\mathcal{G}_{\mathrm{D}}^{(1)}(\Delta_\perp) = \int \frac{\mathrm{d}^2\boldsymbol{B}}{2\pi}\, e^{-i\boldsymbol{\Delta}\cdot\boldsymbol{B}}\,\Phi(B)F_+(B)F_-(B)\cos 2\phi_{\Delta B} \tag{B.5}$$

$$\mathcal{G}_{\mathrm{D}}^{(1')}(\Delta_\perp) = \int \frac{\mathrm{d}^2\boldsymbol{B}}{2\pi}\, e^{-i\boldsymbol{\Delta}\cdot\boldsymbol{B}}\,\Phi(B)[F_-(B)]^2\cos 2\phi_{\Delta B}, \tag{B.6}$$

and

$$\mathcal{G}_{\mathrm{D}}^{(2)}(\Delta_\perp) = \int \frac{\mathrm{d}^2\boldsymbol{B}}{2\pi}\, e^{-i\boldsymbol{\Delta}\cdot\boldsymbol{B}}\, \Phi(B)[F_-(B)]^2 \cos 4\phi_{\Delta B}, \tag{B.7}$$

with $\phi_{\Delta B}$ the angle between the vectors $\boldsymbol{\Delta}$ and $\boldsymbol{B}$.

When calculating the cross section only the coefficients $\mathcal{G}_{\mathrm{D}}^{(+)}(\Delta_\perp)$, $\mathcal{G}_{\mathrm{D}}^{(-)}(\Delta_\perp)$, $\mathcal{G}_{\mathrm{D}}^{(1)}(\Delta_\perp)$ and $\mathcal{G}_{\mathrm{D}}^{(2)}(\Delta_\perp)$ survive as mentioned in Sect. 4.3.

The hard factors can be written in a similar form by using the traceless tensor

$$\hat{P}^{ij} \equiv \frac{P^i P^j}{P_\perp^2} - \frac{\delta^{ij}}{2}. \tag{B.8}$$

Contracting the transverse hard factor $H_T^{iks} H_T^{jls*}$ in Eq. (4.33), we get after some algebra the convenient expression

$$\begin{aligned} H_T^{iks}(\boldsymbol{P},\bar{Q})\, H_T^{jls*}(\boldsymbol{P},\bar{Q}) = {} & \frac{16P^2(3\bar{Q}^4 + 2\bar{Q}^2P_\perp^2 - P_\perp^4)}{(P_\perp^2+\bar{Q}^2)^6}\, \frac{\delta^{ik}}{2}\, \frac{\delta^{jl}}{2} \\ & + \frac{16P^2(\bar{Q}^4 - \bar{Q}^2P_\perp^2 + P_\perp^4)}{(P_\perp^2+\bar{Q}^2)^6} \left(\frac{\delta^{ij}}{2}\, \frac{\delta^{kl}}{2} + \frac{\delta^{il}}{2}\, \frac{\delta^{kj}}{2} \right) \\ & + \frac{16P_\perp^2(\bar{Q}^4 - P_\perp^4)}{(P_\perp^2+\bar{Q}^2)^6} \left(\frac{\delta^{ik}}{2} \hat{P}^{jl} + \frac{\delta^{jl}}{2} \hat{P}^{ik} \right) \\ & + \frac{8P_\perp^2(\bar{Q}^2 - P_\perp^2)^2}{(P_\perp^2+\bar{Q}^2)^6} \left(\frac{\delta^{ij}}{2} \hat{P}^{kl} + \frac{\delta^{kl}}{2} \hat{P}^{ij} + \frac{\delta^{il}}{2} \hat{P}^{kj} + \frac{\delta^{kj}}{2} \hat{P}^{il} \right) \\ & - \frac{32\bar{Q}^2P_\perp^4}{(P_\perp^2+\bar{Q}^2)^6} \left(\hat{P}^{ij}\hat{P}^{kl} - \frac{1}{2}\, \frac{\delta^{ij}}{2}\, \frac{\delta^{kl}}{2} + \hat{P}^{il}\hat{P}^{kj} - \frac{1}{2}\, \frac{\delta^{il}}{2}\, \frac{\delta^{kj}}{2} \right). \end{aligned} \tag{B.9}$$

The longitudinal hard factor can be obtained in the same way with the simplification that there are no indices to contract in Eq. (4.47), so we find

$$\begin{aligned} H_L^{ik}(\boldsymbol{P},\bar{Q})\, H_L^{jl}(\boldsymbol{P},\bar{Q}) = {} & \frac{16\bar{Q}^2(\bar{Q}^4 - 2\bar{Q}^2P_\perp^2 + 3P_\perp^4)}{(P_\perp^2+\bar{Q}^2)^6}\, \frac{\delta^{ik}}{2}\, \frac{\delta^{jl}}{2} \\ & - \frac{32\bar{Q}^2P_\perp^2(\bar{Q}^2 - P_\perp^2)}{(P_\perp^2+\bar{Q}^2)^6} \left(\frac{\delta^{ik}}{2}\hat{P}^{jl} + \frac{\delta^{jl}}{2}\hat{P}^{ik} \right) \\ & + \frac{64\bar{Q}^2P_\perp^4}{(P_\perp^2+\bar{Q}^2)^6} \left(\hat{P}^{ik}\hat{P}^{jl} - \frac{1}{2}\, \frac{\delta^{ik}}{2}\, \frac{\delta^{jl}}{2} \right). \end{aligned} \tag{B.10}$$

Using the formulae

$$\delta^{ij}\hat{P}^{ij} = 0\,, \qquad \hat{P}^{ij}\hat{P}^{ij} = \frac{1}{2} \qquad \text{and} \qquad \hat{P}^{ij}\hat{P}^{jk} = \frac{1}{4}\,\delta^{ik} \tag{B.11}$$

(and similarly for $\hat{\Delta}^{ij}$) and

$$2\hat{P}^{ij}\hat{\Delta}^{ji} = 2\cos^2\phi - 1 = \cos 2\phi \tag{B.12}$$

$$8\hat{P}^{ij}\hat{\Delta}^{jk}\hat{P}^{kl}\hat{\Delta}^{li} = 8\cos^4\phi - 8\cos^2\phi + 1 = \cos 4\phi \tag{B.13}$$

where ϕ is the angle between $\boldsymbol{P}$ and $\boldsymbol{\Delta}$, we can contract $\mathcal{G}_{\mathrm{D}}^{ij,kl}$ in Eq. (B.1) with either $H_T^{iks}H_T^{jls*}$ as expressed in Eq. (B.9) or $H_L^{ik}H_L^{jl}$ as expressed in Eq. (B.10) to get Eqs. (4.45) and (4.48).

Appendix C

Inclusive dijet production

We review here the cross section for inclusive dijet production [27, 113]. In analogy to the expression is Eq. (4.17), the diffractive correlator $\mathcal{W}_{\mathrm{D}}$ is replaced with the inclusive one,

$$\mathcal{W}_{\mathrm{incl}}(\boldsymbol{r},\bar{\boldsymbol{r}},\boldsymbol{B}) = \frac{1}{N_c}\left\langle \mathrm{tr}\big[V(\boldsymbol{x})V^\dagger(\boldsymbol{y})V(\bar{\boldsymbol{y}})V^\dagger(\bar{\boldsymbol{x}})\big] - \mathrm{tr}\big[V(\boldsymbol{x})V^\dagger(\boldsymbol{y})\big] - \mathrm{tr}\big[V(\bar{\boldsymbol{y}})V^\dagger(\bar{\boldsymbol{x}})\big] + 1\right\rangle. \tag{C.1}$$

We assume the Gaussian approximation, and in the correlation limit we single out the semihard dynamics into the gluon TMD which in the present notation is defined as

$$xG^{ij}(\boldsymbol{\Delta}) = \frac{C_F}{4\pi^3\alpha_s}\int \frac{\mathrm{d}^2\boldsymbol{B}}{2\pi}\, e^{-i\boldsymbol{\Delta}\cdot\boldsymbol{B}}\, \frac{1-\mathcal{S}_g(B)}{\ln\mathcal{S}_g(B)}\,\partial^i\partial^j \ln\mathcal{S}_g(B) = \frac{\delta^{ij}}{2}\, xG(\Delta_\perp) + \hat{\Delta}^{ij}\, xh(\Delta_\perp). \tag{C.2}$$

The unpolarized and polarized unintegrated gluon distribution of the nucleus are given by

$$xG(\Delta_\perp) = \frac{C_F}{4\pi^3\alpha_s}\int_0^\infty \mathrm{d}B B\, J_0(\Delta_\perp B)\,\frac{1-\mathcal{S}_g(B)}{\ln\mathcal{S}_g(B)}\, F_+(B) \tag{C.3}$$

and

$$xh(\Delta_\perp) = -\frac{C_F}{4\pi^3\alpha_s}\int_0^\infty \mathrm{d}B B\, J_2(\Delta_\perp B)\,\frac{1-\mathcal{S}_g(B)}{\ln\mathcal{S}_g(B)}\, F_-(B), \tag{C.4}$$

where the functions $F_+(B)$ and $F_-(B)$ are defined in Eq. (4.37)). The inclusive cross sections can then be written by contracting with the corresponding hard factors, i.e.

$$\begin{aligned}\frac{\mathrm{d}\sigma_{\mathrm{inc}}^{\gamma_T^* A\to q\bar{q}X}}{\mathrm{d}\vartheta_1\mathrm{d}\vartheta_2\mathrm{d}^2\boldsymbol{P}\mathrm{d}^2\boldsymbol{\Delta}} =& S_\perp\alpha_{\mathrm{em}}\Big(\sum e_f^2\Big)\,\delta(1-\vartheta_1-\vartheta_2)\,\big(\vartheta_1^2+\vartheta_2^2\big)\\ &\times\left[\frac{P_\perp^4+\bar{Q}^4}{(P_\perp^2+\bar{Q}^2)^4}\,\alpha_s xG(\Delta_\perp) - \frac{2\bar{Q}^2P_\perp^2}{(P_\perp^2+\bar{Q}^2)^4}\,\alpha_s xh(\Delta_\perp)\cos 2\phi\right]\end{aligned} \tag{C.5}$$

and

$$\begin{aligned}\frac{\mathrm{d}\sigma_{\mathrm{inc}}^{\gamma_L^* A\to q\bar{q}X}}{\mathrm{d}\vartheta_1\mathrm{d}\vartheta_2\mathrm{d}^2\boldsymbol{P}\mathrm{d}^2\boldsymbol{\Delta}} =& S_\perp\alpha_{\mathrm{em}}\Big(\sum e_f^2\Big)\,\delta(1-\vartheta_1-\vartheta_2)(4\vartheta_1\vartheta_2)\\ &\times\frac{2\bar{Q}^2P_\perp^2}{(P_\perp^2+\bar{Q}^2)^4}\big[\alpha_s xG(\Delta_\perp) + \alpha_s xh(\Delta_\perp)\cos 2\phi\big].\end{aligned} \tag{C.6}$$

Appendix D

Next to leading kinematic twist in the $q\bar{q}$ contribution

The first kinematic corrections to the transverse and longitudinal cross sections are given in Eqs. (4.69) and (4.70). They involve the hard tensors $H_T^{ikmns}(\boldsymbol{P},\bar{Q})$ and $H_L^{ikmn}(\boldsymbol{P},\bar{Q})$, which can be written as

$$
\begin{aligned}
H_T^{ikmns}(\boldsymbol{P},\bar{Q}) = &-\frac{8i}{(P_\perp^2+\bar{Q}^2)^3}\big(P^i(\delta^{kl}\delta^{ms}+\delta^{km}\delta^{ls}+\delta^{ks}\delta^{lm}) \\
&+P^k(\delta^{il}\delta^{ms}+\delta^{im}\delta^{ls}+\delta^{is}\delta^{lm})+P^l(\delta^{ik}\delta^{ms}+\delta^{im}\delta^{ks}+\delta^{is}\delta^{km}) \\
&+\ P^m(\delta^{ik}\delta^{ls}+\delta^{il}\delta^{ks}+\delta^{is}\delta^{kl})+P^s(\delta^{ik}\delta^{lm}+\delta^{il}\delta^{km}+\delta^{im}\delta^{kl})\big) \\
&+\frac{48i}{(P_\perp^2+\bar{Q})^4}\big(\delta^{ik}P^lP^mP^s+\delta^{il}P^kP^mP^s+\delta^{im}P^kP^lP^s \\
&+\ \delta^{is}P^kP^lP^m+\delta^{kl}P^iP^mP^s+\delta^{km}P^iP^lP^s+\delta^{ks}P^iP^lP^m\big) \\
&-\frac{384i}{(P_\perp^2+\bar{Q})^5}P^iP^kP^lP^mPs
\end{aligned}
\tag{D.1}
$$

and

$$
\begin{aligned}
H_L^{ikmn}(\boldsymbol{P},\bar{Q}) = &\frac{32\bar{Q}(\bar{Q}^4-4\bar{Q}^2P_\perp^2+P_\perp^4)}{(P_\perp^2+\bar{Q}^2)^5}\left(\frac{\delta^{ij}}{2}\frac{\delta^{kl}}{2}+\frac{\delta^{ik}}{2}\frac{\delta^{jl}}{2}+\frac{\delta^{il}}{2}\frac{\delta^{jk}}{2}\right) \\
&+\frac{32\bar{Q}P_\perp^2(P_\perp^2-3\bar{Q}^2)}{(P_\perp^2+\bar{Q}^2)^5}\left(\frac{\delta^{ij}}{2}\hat{P}^{kl}+\frac{\delta^{kl}}{2}\hat{P}^{ij}+\frac{\delta^{ik}}{2}\hat{P}^{jl}+\frac{\delta^{jl}}{2}\hat{P}^{ik}+\frac{\delta^{il}}{2}\hat{P}^{jk}+\frac{\delta^{jk}}{2}\hat{P}^{il}\right) \\
&+\frac{128\bar{Q}P_\perp^4}{(P_\perp^2+\bar{Q}^2)^5}\left(\hat{P}^{ij}\hat{P}^{kl}-\frac{1}{2}\frac{\delta^{ij}}{2}\frac{\delta^{kl}}{2}+\hat{P}^{ik}\hat{P}^{jl}-\frac{1}{2}\frac{\delta^{ik}}{2}\frac{\delta^{jl}}{2}+\hat{P}^{il}\hat{P}^{jk}-\frac{1}{2}\frac{\delta^{il}}{2}\frac{\delta^{jk}}{2}\right).
\end{aligned}
\tag{D.2}
$$

The tensor decomposition of the semi-hard factor given in Eq. (4.71) can be written as

$$\begin{aligned}
\mathcal{G}_{\mathrm{D}}^{ij,klmn}(\mathbf{\Delta}) = & \frac{\delta^{ij}}{2}\zeta_0^{klmn}\mathcal{G}_{\mathrm{D}}^{(a_0)}(\mathbf{\Delta}) \\
& + \left[\frac{\delta^{kl}}{2}\zeta_0^{ijmn} + \frac{\delta^{km}}{2}\zeta_0^{ijln} + \frac{\delta^{kn}}{2}\zeta_0^{ijlm} + \frac{\delta^{mn}}{2}\zeta_0^{ijkl} + \frac{\delta^{ln}}{2}\zeta_0^{ijkm} + \frac{\delta^{lm}}{2}\zeta_0^{ijkn}\right]\mathcal{G}_{\mathrm{D}}^{(b_0)}(\mathbf{\Delta}) \\
& + \xi_0^{ijklmn}\mathcal{G}_{\mathrm{D}}^{(c_0)}(\mathbf{\Delta}) + \hat{\Delta}^{ij}\zeta_0^{klmn}\mathcal{G}_{\mathrm{D}}^{(a_1)}(\mathbf{\Delta}) + \frac{\delta^{ij}}{2}\zeta_1^{klmn}\mathcal{G}_{\mathrm{D}}^{(b_1)}(\mathbf{\Delta}) \\
& + \left[\frac{\delta^{kl}}{2}\zeta_1^{ijmn} + \frac{\delta^{km}}{2}\zeta_1^{ijln} + \frac{\delta^{kn}}{2}\zeta_1^{ijlm} + \frac{\delta^{mn}}{2}\zeta_1^{ijkl} + \frac{\delta^{ln}}{2}\zeta_1^{ijkm} + \frac{\delta^{lm}}{2}\zeta_1^{ijkn}\right]\mathcal{G}_{\mathrm{D}}^{(c_1)}(\mathbf{\Delta}) \\
& + \xi_1^{ijklmn}\mathcal{G}_{\mathrm{D}}^{(d_1)}(\mathbf{\Delta}) \\
& + \left[\frac{\delta^{kl}}{2}\zeta_2^{ijmn} + \frac{\delta^{km}}{2}\zeta_2^{ijln} + \frac{\delta^{kn}}{2}\zeta_2^{ijlm} + \frac{\delta^{mn}}{2}\zeta_2^{ijkl} + \frac{\delta^{ln}}{2}\zeta_2^{ijkm} + \frac{\delta^{lm}}{2}\zeta_2^{ijkn}\right]\mathcal{G}_{\mathrm{D}}^{(a_2)}(\mathbf{\Delta}) \\
& + \frac{\delta^{ij}}{2}\zeta_2^{klmn}\mathcal{G}_{\mathrm{D}}^{(b_2)}(\mathbf{\Delta}) + \xi_2^{ijklmn}\mathcal{G}_{\mathrm{D}}^{(c_2)}(\mathbf{\Delta}) + \xi_3^{ijklmn}\mathcal{G}_{\mathrm{D}}^{(3)}(\mathbf{\Delta}),
\end{aligned} \tag{D.3}$$

where in order to compact the expression we have defined the following tensors

$$\zeta_0^{ijkl} = \frac{\delta^{ij}}{2}\frac{\delta^{kl}}{2} + \frac{\delta^{ik}}{2}\frac{\delta^{jl}}{2} + \frac{\delta^{il}}{2}\frac{\delta^{jk}}{2}, \tag{D.4}$$

$$\zeta_1^{ijkl} = \frac{\delta^{ij}}{2}\hat{\Delta}^{kl} + \frac{\delta^{kl}}{2}\hat{\Delta}^{ij} + \frac{\delta^{ik}}{2}\hat{\Delta}^{jl} + \frac{\delta^{jl}}{2}\hat{\Delta}^{ik} + \frac{\delta^{il}}{2}\hat{\Delta}^{jk} + \frac{\delta^{jk}}{2}\hat{\Delta}^{il}, \tag{D.5}$$

$$\zeta_2^{ijkl} = \hat{\Delta}^{ij}\hat{\Delta}^{kl} - \frac{1}{2}\frac{\delta^{ij}}{2}\frac{\delta^{kl}}{2} + \hat{\Delta}^{ik}\hat{\Delta}^{jl} - \frac{1}{2}\frac{\delta^{ik}}{2}\frac{\delta^{jl}}{2} + \hat{\Delta}^{il}\hat{\Delta}^{jk} - \frac{1}{2}\frac{\delta^{il}}{2}\frac{\delta^{jk}}{2}, \tag{D.6}$$

$$\xi_0^{ijkl} = \frac{\delta^{ij}}{2}\zeta_0^{klmn} + \frac{\delta^{ik}}{2}\zeta_0^{jlmn} + \frac{\delta^{il}}{2}\zeta_0^{jkmn} + \frac{\delta^{im}}{2}\zeta_0^{jkln} + \frac{\delta^{in}}{2}\zeta_0^{jklm}, \tag{D.7}$$

$$\begin{aligned}
\xi_1^{ijkl} =& \hat{\Delta}^{ij}\zeta_0^{klmn} + \hat{\Delta}^{ik}\zeta_0^{jlmn} + \hat{\Delta}^{il}\zeta_0^{jkmn} + \hat{\Delta}^{im}\zeta_0^{jkln} + \hat{\Delta}^{in}\zeta_0^{jklm} \\
&+ \hat{\Delta}^{jk}\zeta_0^{ilmn} + \hat{\Delta}^{jl}\zeta_0^{ikmn} + \hat{\Delta}^{jm}\zeta_0^{ikln} + \hat{\Delta}^{jn}\zeta_0^{iklm} + \hat{\Delta}^{kl}\zeta_0^{ijmn} \\
&+ \hat{\Delta}^{km}\zeta_0^{ijln} + \hat{\Delta}^{kn}\zeta_0^{ijlm} + \hat{\Delta}^{lm}\zeta_0^{ijkn} + \hat{\Delta}^{ln}\zeta_0^{ijkm} + \hat{\Delta}^{mn}\zeta_0^{ijkl},
\end{aligned} \tag{D.8}$$

$$\begin{aligned}
\xi_2^{ijkl} =& \frac{\delta^{ij}}{2}\zeta_2^{klmn} + \frac{\delta^{ik}}{2}\zeta_2^{jlmn} + \frac{\delta^{il}}{2}\zeta_2^{jkmn} + \frac{\delta^{im}}{2}\zeta_2^{jkln} + \frac{\delta^{in}}{2}\zeta_2^{jklm} \\
&+ \frac{\delta^{jk}}{2}\zeta_2^{ilmn} + \frac{\delta^{jl}}{2}\zeta_2^{ikmn} + \frac{\delta^{jm}}{2}\zeta_2^{ikln} + \frac{\delta^{jn}}{2}\zeta_2^{iklm} + \frac{\delta^{kl}}{2}\zeta_2^{ijmn} \\
&+ \frac{\delta^{km}}{2}\zeta_2^{ijln} + \frac{\delta^{kn}}{2}\zeta_2^{ijlm} + \frac{\delta^{lm}}{2}\zeta_2^{ijkn} + \frac{\delta^{ln}}{2}\zeta_2^{ijkm} + \frac{\delta^{mn}}{2}\zeta_2^{ijkl},
\end{aligned} \tag{D.9}$$

and finally

$$\xi_3^{ijkl} = \frac{\Delta^i\Delta^j\Delta^k\Delta^l\Delta^m\Delta^n}{\Delta^6} - \frac{1}{15}\xi_2^{ijkl} - \frac{1}{12}\xi_1^{ijkl} - \frac{1}{6}\xi_0^{ijkl}. \tag{D.10}$$

The semi-hard coefficientes in Eq. (D.3) are

$$\mathcal{G}_{\mathrm{D}}^{(a_0)}(\boldsymbol{\Delta}) = \int \frac{\mathrm{d}^2\boldsymbol{B}}{2\pi}\, e^{-i\boldsymbol{\Delta}\cdot\boldsymbol{B}}\Phi(B)\left[F_+(B)F_3(B) + (F_+(B) - F_-(B))(2F_4(B) + \frac{1}{2}F_5(B))\right], \tag{D.11}$$

$$\mathcal{G}_{\mathrm{D}}^{(b_0)}(\boldsymbol{\Delta}) = \frac{1}{2}\int \frac{\mathrm{d}^2\boldsymbol{B}}{2\pi}\, e^{-i\boldsymbol{\Delta}\cdot\boldsymbol{B}}\Phi(B)F_-(B)F_4(B), \tag{D.12}$$

$$\mathcal{G}_{\mathrm{D}}^{(c_0)}(\boldsymbol{\Delta}) = \frac{1}{6}\int \frac{\mathrm{d}^2\boldsymbol{B}}{2\pi}\, e^{-i\boldsymbol{\Delta}\cdot\boldsymbol{B}}\Phi(B)F_-(B)F_5(B), \tag{D.13}$$

$$\mathcal{G}_{\mathrm{D}}^{(a_1)}(\boldsymbol{\Delta}) = \int \frac{\mathrm{d}^2\boldsymbol{B}}{2\pi}\, e^{-i\boldsymbol{\Delta}\cdot\boldsymbol{B}}\Phi(B)F_-(B)F_3(B)\cos 2\phi_{\Delta B}, \tag{D.14}$$

$$\mathcal{G}_{\mathrm{D}}^{(b_1)}(\boldsymbol{\Delta}) = \int \frac{\mathrm{d}^2\boldsymbol{B}}{2\pi}\, e^{-i\boldsymbol{\Delta}\cdot\boldsymbol{B}}\Phi(B)\left[(F_+(B) - F_-(B))(F_4(B) + \frac{1}{3}F_5(B))\right]\cos 2\phi_{\Delta B}, \tag{D.15}$$

$$\mathcal{G}_{\mathrm{D}}^{(c_1)}(\boldsymbol{\Delta}) = \frac{1}{3}\int \frac{\mathrm{d}^2\boldsymbol{B}}{2\pi}\, e^{-i\boldsymbol{\Delta}\cdot\boldsymbol{B}}\Phi(B)F_-(B)F_4(B)\cos 2\phi_{\Delta B}, \tag{D.16}$$

$$\mathcal{G}_{\mathrm{D}}^{(d_1)}(\boldsymbol{\Delta}) = \frac{1}{12}\int \frac{\mathrm{d}^2\boldsymbol{B}}{2\pi}\, e^{-i\boldsymbol{\Delta}\cdot\boldsymbol{B}}\Phi(B)F_-(B)F_5(B)\cos 2\phi_{\Delta B}, \tag{D.17}$$

$$\mathcal{G}_{\mathrm{D}}^{(a_2)}(\boldsymbol{\Delta}) = \frac{1}{3}\int \frac{\mathrm{d}^2\boldsymbol{B}}{2\pi}\, e^{-i\boldsymbol{\Delta}\cdot\boldsymbol{B}}\Phi(B)F_-(B)F_4(B)\cos 4\phi_{\Delta B}, \tag{D.18}$$

$$\mathcal{G}_{\mathrm{D}}^{(b_2)}(\boldsymbol{\Delta}) = \frac{1}{3}\int \frac{\mathrm{d}^2\boldsymbol{B}}{2\pi}\, e^{-i\boldsymbol{\Delta}\cdot\boldsymbol{B}}\Phi(B)(F_+ - F_-(B))F_5(B)\cos 4\phi_{\Delta B}, \tag{D.19}$$

$$\mathcal{G}_{\mathrm{D}}^{(c_2)}(\boldsymbol{\Delta}) = \frac{1}{15}\int \frac{\mathrm{d}^2\boldsymbol{B}}{2\pi}\, e^{-i\boldsymbol{\Delta}\cdot\boldsymbol{B}}\Phi(B)F_-(B)F_5(B)\cos 4\phi_{\Delta B}, \tag{D.20}$$

$$\mathcal{G}_{\mathrm{D}}^{(3)}(\boldsymbol{\Delta}) = \int \frac{\mathrm{d}^2\boldsymbol{B}}{2\pi}\, e^{-i\boldsymbol{\Delta}\cdot\boldsymbol{B}}\Phi(B)F_-(B)F_5(B)\cos 6\phi_{\Delta B}, \tag{D.21}$$

$$\tag{D.22}$$

where the functions $F_+(B)$ and $F_-(B)$ are defined in Eq. (4.38) while we define

$$F_3(B) = 16\frac{\partial}{\partial B^2}\frac{\partial}{\partial B^2}\ln\mathcal{S}_g(B), \tag{D.23}$$

$$F_4(B) = 16B^2\frac{\partial}{\partial B^2}\frac{\partial}{\partial B^2}\frac{\partial}{\partial B^2}\ln\mathcal{S}_g(B), \tag{D.24}$$

$$F_5(B) = 16B^4\frac{\partial}{\partial B^2}\frac{\partial}{\partial B^2}\frac{\partial}{\partial B^2}\frac{\partial}{\partial B^2}\ln\mathcal{S}_g(B). \tag{D.25}$$

Hence, having the tensors $H_T^{ikmns}(\boldsymbol{P},\bar{Q})$, $H_T^{jls^*}(\boldsymbol{P},\bar{Q})$ and $\mathcal{G}_{\mathrm{D}}^{ij,klmn}(\boldsymbol{\Delta})$ encoded in Eqs. (D.1), (4.34) and (D.3) respectively, we can find the higher twist correction to the reduced cross sections. By using the notation in Eq. (4.56), we find that the correction of the averaged over angle cross section in the transverse sector reads

$$\begin{aligned}\delta\mathcal{N}_0^T = \frac{24P_\perp^2\bar{Q}^2}{(P_\perp^2+\bar{Q}^2)^8}\Big[&2P_\perp^4(\mathcal{G}_{\mathrm{D}}^{(a_0)}(\boldsymbol{\Delta}) + 5\mathcal{G}_{\mathrm{D}}^{(b_0)}(\boldsymbol{\Delta}) + 4\mathcal{G}_{\mathrm{D}}^{(c_0)}(\boldsymbol{\Delta}))\\ &- (P_\perp^2 - \bar{Q}^2)\bar{Q}^2(3\mathcal{G}_{\mathrm{D}}^{(a_0)}(\boldsymbol{\Delta}) + 19\mathcal{G}_{\mathrm{D}}^{(b_0)}(\boldsymbol{\Delta}) + 16\mathcal{G}_{\mathrm{D}}^{(c_0)}(\boldsymbol{\Delta}))\Big]\end{aligned} \tag{D.26}$$

while the contribution to the elliptic anisotropy in the same sector can be written as

$$\begin{aligned}\delta\mathcal{N}_2^T = &\frac{6P_\perp^2}{(P_\perp^2+\bar{Q}^2)^8}\Big[\bar{Q}^6(4\mathcal{G}_{\rm D}^{(a_1)}(\boldsymbol{\Delta})+7\mathcal{G}_{\rm D}^{(b_1)}(\boldsymbol{\Delta})+45\mathcal{G}_{\rm D}^{(c_1)}(\boldsymbol{\Delta})+56\mathcal{G}_{\rm D}^{(d_1)}(\boldsymbol{\Delta}))\\ &-2P_\perp^2\bar{Q}^4(5\mathcal{G}_{\rm D}^{(a_1)}(\boldsymbol{\Delta})+10\mathcal{G}_{\rm D}^{(b_1)}(\boldsymbol{\Delta})+60\mathcal{G}_{\rm D}^{(c_1)}(\boldsymbol{\Delta})+76\mathcal{G}_{\rm D}^{(d_1)}(\boldsymbol{\Delta}))\\ &+P_\perp^4\bar{Q}^2[2\mathcal{G}_{\rm D}^{(a_1)}(\boldsymbol{\Delta})+3(\mathcal{G}_{\rm D}^{(b_1)}(\boldsymbol{\Delta})+7\mathcal{G}_{\rm D}^{(c_1)}(\boldsymbol{\Delta})+8\mathcal{G}_{\rm D}^{(d_1)}(\boldsymbol{\Delta}))]\\ &-\ 2P_\perp^6(\mathcal{G}_{\rm D}^{(b_1)}(\boldsymbol{\Delta})+3\mathcal{G}_{\rm D}^{(c_1)}(\boldsymbol{\Delta})+4\mathcal{G}_{\rm D}^{(d_1)}(\boldsymbol{\Delta}))\Big]\,. \end{aligned} \tag{D.27}$$

Similarly, in the longitudinal sector, using the Eqs. (D.2) and (4.47) for the hard tensors $H_L^{ikmn}(\boldsymbol{P},\bar{Q})$ and $H_L^{jl*}(\boldsymbol{P},\bar{Q})$, we find for the averaged cross section

$$\begin{aligned}\delta\mathcal{N}_0^L = &\frac{8\bar{Q}^2}{(P_\perp^2+\bar{Q}^2)^8}\Big[-2P_\perp^6(2\mathcal{G}_{\rm D}^{(a_0)}(\boldsymbol{\Delta})+11\mathcal{G}_{\rm D}^{(b_0)}(\boldsymbol{\Delta})+9\mathcal{G}_{\rm D}^{(c_0)}(\boldsymbol{\Delta}))\\ &+2P_\perp^4\bar{Q}^2(7\mathcal{G}_{\rm D}^{(a_0)}(\boldsymbol{\Delta})+40\mathcal{G}_{\rm D}^{(b_0)}(\boldsymbol{\Delta})+33\mathcal{G}_{\rm D}^{(c_0)}(\boldsymbol{\Delta}))\\ &-5P_\perp^2\bar{Q}^4(\mathcal{G}_{\rm D}^{(a_0)}(\boldsymbol{\Delta})+7\mathcal{G}_{\rm D}^{(b_0)}(\boldsymbol{\Delta})+6\mathcal{G}_{\rm D}^{(c_0)}(\boldsymbol{\Delta}))\\ &+\ \bar{Q}^6(\mathcal{G}_{\rm D}^{(a_0)}(\boldsymbol{\Delta})+7\mathcal{G}_{\rm D}^{(b_0)}(\boldsymbol{\Delta})+6\mathcal{G}_{\rm D}^{(c_0)}(\boldsymbol{\Delta}))\Big]\,, \end{aligned} \tag{D.28}$$

whereas for the elliptic contribution we have

$$\begin{aligned}\delta\mathcal{N}_2^L = &\frac{2P_\perp^2\bar{Q}^2}{(P_\perp^2+\bar{Q}^2)^8}\Big[-P_\perp^4[7\mathcal{G}_{\rm D}^{(a_1)}(\boldsymbol{\Delta})+6(4\mathcal{G}_{\rm D}^{(b_1)}(\boldsymbol{\Delta})+19\mathcal{G}_{\rm D}^{(c_1)}(\boldsymbol{\Delta})+24\mathcal{G}_{\rm D}^{(d_1)}(\boldsymbol{\Delta}))]\\ &+4P_\perp^2\bar{Q}^2[7\mathcal{G}_{\rm D}^{(a_1)}(\boldsymbol{\Delta})+12\mathcal{G}_{\rm D}^{(b_1)}(\boldsymbol{\Delta})+78\mathcal{G}_{\rm D}^{(c_1)}(\boldsymbol{\Delta})+96\mathcal{G}_{\rm D}^{(d_1)}(\boldsymbol{\Delta})]\\ &-\ \bar{Q}^4[13\mathcal{G}_{\rm D}^{(a_1)}(\boldsymbol{\Delta})+6(4\mathcal{G}_{\rm D}^{(b_1)}(\boldsymbol{\Delta})+25\mathcal{G}_{\rm D}^{(c_1)}(\boldsymbol{\Delta})+32\mathcal{G}_{\rm D}^{(d_1)}(\boldsymbol{\Delta}))]\Big]\,. \end{aligned} \tag{D.29}$$

By using the MV model (cf. Eq. (2.48)) in Eqs. (D.26), (D.27), (D.28) and (D.29) we arrive respectively at Eqs. (4.72), (4.73), (4.74) and (4.75).

Appendix E

The gluon semi-hard tensor and its index structure in the $q\bar{q}g$ contribution

As discussed in Chapter 3, coherent and incoherent diffraction differ on how their respective correlators are averaged, i.e. either at the amplitude or at the cross section level respectively. This allows us to obtain the semi-hard tensor for incoherent diffraction of a gluon-gluon dipole from its counterpart in the coherent case [55] by applying the replacement

$$\delta^{(2)}(\boldsymbol{\Delta})\mathcal{T}_g(R)\mathcal{T}_g(\bar{R}) \to \int \frac{\mathrm{d}^2\boldsymbol{B}}{(2\pi)^2}\, e^{-i\boldsymbol{\Delta}\cdot\boldsymbol{B}}\, \mathcal{W}_g(\boldsymbol{R},\bar{\boldsymbol{R}},\boldsymbol{B}). \tag{E.1}$$

Hence, we find

$$\mathcal{G}^{ij}_{\mathrm{inc}}(x, x_{\mathbb{P}}, \boldsymbol{k}_3, \boldsymbol{\Delta}) = \frac{1}{4\pi}\int \frac{\mathrm{d}^2\boldsymbol{B}}{2\pi}\,\frac{\mathrm{d}^2\boldsymbol{R}}{2\pi}\,\frac{\mathrm{d}^2\bar{\boldsymbol{R}}}{2\pi}\, e^{-i\boldsymbol{\Delta}\cdot\boldsymbol{B}-i\boldsymbol{k}_3\cdot(\boldsymbol{R}-\bar{\boldsymbol{R}})}$$
$$\left(\hat{R}^{ik}\hat{\bar{R}}^{kj} + \hat{R}^{jk}\hat{\bar{R}}^{ki}\right)\mathcal{M}^2 K_2(\mathcal{M}R)\,\mathcal{M}^2 K_2(\mathcal{M}\bar{R})\,\mathcal{W}_g(\boldsymbol{R},\bar{\boldsymbol{R}},\boldsymbol{B}), \tag{E.2}$$

where we have symmetrized the indices i and j by anticipating an eventual contraction with a symmetric hard tensor. The momentum dependence indicates that, in general, the tensor $\mathcal{G}^{ij}_{\mathrm{inc}}$ can be decomposed into a diagonal term plus three traceless terms, namely

$$\mathcal{G}^{ij}_{\mathrm{inc}} = \mathcal{G}_{\mathrm{inc}}\,\frac{\delta^{ij}}{4} + A_1\hat{\Delta}^{ij} + A_2\hat{k}_3^{ij} + A_3\left(\frac{\Delta^i k_3^j}{\Delta_\perp k_{3\perp}} + \frac{\Delta^j k_3^i}{\Delta_\perp k_{3\perp}} - \frac{\boldsymbol{\Delta}\cdot\boldsymbol{k}_3}{\Delta_\perp k_{3\perp}}\,\delta^{ij}\right), \tag{E.3}$$

where the coefficients $\mathcal{G}_{\mathrm{inc}}$, A_1, A_2 and A_3 are scalars depending only on $\Delta_\perp$, $k_{3\perp}$ and $\boldsymbol{\Delta}\cdot\boldsymbol{k}_3$. Reminding the "hat" notation given in Eq. (4.39) for arbitrary vectors, it is straightforward to prove that

$$\hat{R}^{ik}\hat{\bar{R}}^{kj}\hat{V}^{ij} = 0. \tag{E.4}$$

Similarly, the aforementioned symmetrization allows us to show that

$$\left(\hat{R}^{ik}\hat{\bar{R}}^{kj} + \hat{R}^{jk}\hat{\bar{R}}^{ki}\right)\left(\frac{V_1^i V_2^j}{V_{1\perp}V_{2\perp}} - \frac{\boldsymbol{V}_1\cdot\boldsymbol{V}_2}{V_{1\perp}V_{2\perp}}\,\frac{\delta^{ij}}{2}\right) = 0 \tag{E.5}$$

for arbitrary vectors $\boldsymbol{V}_1$ and $\boldsymbol{V}_2$. Hence, contracting (E.3) with each one of the traceless tensors appearing in the decomposition in Eq. (E.3) and using the last two identities, it is easy to show that $A_1 = A_2 = A_3 = 0$. The contraction of the remaining diagonal term leads to the final form of the semi-hard gluon tensor given in Eqs. (5.5) and (5.6).

Appendix F

The incoherent gluon DPDF in limiting cases

Here, we provide in detail the analytical calculations of the dominant term of the incoherent gluon DPDF at low and high momenta in the limiting cases $x \ll 1$ and $1-x \ll 1$. To this end, we consider Eq. (6.16) and rewrite it here for convenience

$$\frac{\mathrm{d}xG_{\mathbb{P}}^{\mathrm{inc}}(x, x_{\mathbb{P}}, P_\perp, \Delta_\perp)}{\mathrm{d}^2\boldsymbol{\Delta}} = \frac{S_\perp(N_c^2-1)}{4\pi^3}\,\frac{1}{2\pi}\int \mathrm{d}^2\boldsymbol{k}\,\frac{\mathcal{G}_{\mathrm{inc}}(x, x_{\mathbb{P}}, \boldsymbol{k}, \boldsymbol{\Delta})}{1-x}, \tag{F.1}$$

where, recalling also the discussion in Sect. 6.2.2, the upper limit of the integration over $\boldsymbol{k}$ is unrestricted and thus the DPDF is $P_\perp$-independent. We work in the Gaussian approximation [109, 112, 128–130] where the multipoint correlator $\mathcal{W}_g$, which enters the definition of $\mathcal{G}_{\mathrm{inc}}$ in Eq. (5.6), reads [131]

$$\mathcal{W}_g(\boldsymbol{R}, \bar{\boldsymbol{R}}, \boldsymbol{B}) = \frac{2}{N_c^2} f^2 \mathcal{S}_g(R)\,\mathcal{S}_g(\bar{R})\left[\frac{e^{-F}-1+F}{F^2} + \frac{e^{-(F-f)}-1+(F-f)}{(F-f)^2}\right], \tag{F.2}$$

where[1]

$$F = \frac{1}{2}\ln\frac{\mathcal{S}_g(R)\mathcal{S}_g(\bar{R})}{\mathcal{S}_g(|\boldsymbol{B}+\boldsymbol{R}-\bar{\boldsymbol{R}}|)\mathcal{S}_g(B)} \qquad \text{and} \qquad f = \frac{1}{2}\ln\frac{\mathcal{S}_g(|\boldsymbol{B}+\boldsymbol{R}|)\mathcal{S}_g(|\boldsymbol{B}-\bar{\boldsymbol{R}}|)}{\mathcal{S}_g(|\boldsymbol{B}+\boldsymbol{R}-\bar{\boldsymbol{R}}|)\mathcal{S}_g(B)}. \tag{F.3}$$

The above expressions hold in the large-N_c approximation, meaning that terms of order $1/N_c^4$ or higher are not included, and it remains valid for any values of $\boldsymbol{R}$, $\bar{\boldsymbol{R}}$, and $\boldsymbol{B}$. We also provide here the corresponding expression for the correlator $\mathcal{W}_q$ in the fundamental representation (cf. Eq. (4.29) and the discussion above for the large-N_c limit) which is utilized for the numerical evaluation of the incoherent quark DPDF, namely

$$\mathcal{W}_q(\boldsymbol{R}, \bar{\boldsymbol{R}}, \boldsymbol{B}) = \frac{1}{N_c^2} f^2 \mathcal{S}(R)\mathcal{S}(\bar{R})\,\frac{e^{-F}-1+F}{F^2}. \tag{F.4}$$

As discussed in Section 2.2.1, in the Gaussian approximation we have the relation $\mathcal{S}(R) = [\mathcal{S}_g(R)]^{C_F/N_c}$, which reduces to $\mathcal{S}(R) \simeq \sqrt{\mathcal{S}_g(R)}$ at large-N_c. We will take again $\mathcal{S}_g(R)$ to be given by the MV model, cf. Eqs. (2.48) and (2.49).

[1] Note the analogy with the definitions given in Eq. (4.23) for the double dipole correlator in the fundamental representation Eq. (4.22).

The expressions in Eqs. (F.2) and (F.4) have a similar functional form, where the key distinction arises from the additional term in Eq. (F.2), which renders the square bracket symmetric under transformation $F \to F - f$. This symmetry guarantees that the gluon correlator $\mathcal{W}_g$ remains invariant when exchanging the positions of the gluons within one of the two dipoles.

F.1 The case $x \ll 1$

For $x \ll 1$, we find that $\mathcal{M} \simeq k_\perp \sqrt{x} \ll k_\perp$, implying that contributions from the region where $k_\perp R \gtrsim 1/\sqrt{x} \gg 1$ are suppressed. This suppression arises due to the strong oscillations induced by the exponential factor $e^{-i\boldsymbol{k}\cdot\boldsymbol{R}}$, which prevents significant contributions when the argument of the Bessel functions K_2 approaches or exceeds unity. Consequently, we can expand the Bessel functions for small arguments, using the approximation $\mathcal{M}^2 K_2(\mathcal{M}R) \simeq 2/R^2$ (and analogously for $\mathcal{M}^2 K_2(\mathcal{M}\bar{R})$). This simplification renders the integral over $\boldsymbol{k}$ trivial, leading to $(2\pi)^2\delta^{(2)}(\boldsymbol{R} - \bar{\boldsymbol{R}})$. As a result, we can directly integrate over $\bar{\boldsymbol{R}}$, yielding a particularly simple final expression

$$\int \mathrm{d}^2\boldsymbol{k}\, \mathcal{G}_{\mathrm{inc}} = 4 \int \frac{\mathrm{d}^2\boldsymbol{B}}{2\pi}\, e^{-i\boldsymbol{\Delta}\cdot\boldsymbol{B}} \int \frac{\mathrm{d}^2\boldsymbol{R}}{2\pi}\, \frac{\mathcal{W}_g(\boldsymbol{R}, \bar{\boldsymbol{R}} = \boldsymbol{R}, \boldsymbol{B})}{R^4}. \tag{F.5}$$

The relation $\bar{\boldsymbol{R}} = \boldsymbol{R}$ implies that the functions F and f in Eq. (F.3) simplify and read

$$F = \ln \frac{\mathcal{S}_g(R)}{\mathcal{S}_g(B)} \qquad \text{and} \qquad f = \frac{1}{2} \ln \frac{\mathcal{S}_g(|\boldsymbol{B}+\boldsymbol{R}|)\mathcal{S}_g(|\boldsymbol{B}-\boldsymbol{R}|)}{\mathcal{S}_g^2(B)}. \tag{F.6}$$

Low momenta $\Delta_\perp \ll Q_s$

In this regime, the dominant contribution originates from configurations where $B \gg 2/Q_s, R$, while no specific hierarchy is assumed between R and $2/Q_s$. This allows us to directly obtain

$$F \simeq F - f \simeq -\ln \mathcal{S}_g(B) = \frac{Q_A^2 B^2}{4}\, \ln \frac{4}{B^2\Lambda^2} \gg 1. \tag{F.7}$$

For f, the leading term cancels, and by performing a Taylor expansion for $R \ll B$, we identify the dominant logarithmic enhanced term[2]

$$f \simeq -\frac{Q_A^2 R^2}{4} \ln \frac{4}{B^2\Lambda^2}. \tag{F.8}$$

Substituting the last two equations into Eq. (F.2), we observe that the correlator takes the form

$$\mathcal{W}_g(\boldsymbol{R}, \boldsymbol{R}, \boldsymbol{B}) \simeq \frac{1}{N_c^2}\, Q_A^2 R^4 \mathcal{S}_g^2(R)\, \frac{\ln 4/B^2\Lambda^2}{B^2}. \tag{F.9}$$

The integration over $\boldsymbol{R}$ is controlled by dipole sizes of the order of $2/Q_s$. Specifically, in the MV model, we find[3]

$$\int_0^\infty \mathrm{d}R\, R\, \mathcal{S}_g^2(R) \simeq \frac{1}{Q_s^2}, \tag{F.10}$$

[2]When R appears alongside B within a logarithm, it can be set to zero. This property, along with its counterpart for $B \ll R$ in the high-momentum region, will be frequently utilized throughout this Appendix.

[3]The leading result coincides with that obtained using the GBW model. By using the MV model, one can compute corrections that are suppressed by inverse powers of $\ln Q_s^2/\Lambda^2$ [132], which we neglect here.

where have extended the integration to infinity, as R is not constrained with respect to $2/Q_s$, which allows us to account for the exact coefficient. Recall that $Q_s^2 = Q_A^2 \ln Q_s^2/\Lambda^2$, and thus we obtain

$$\int \mathrm{d}^2\boldsymbol{k}\, \mathcal{G}_{\mathrm{inc}} \simeq \frac{4}{N_c^2}\, \frac{1}{\ln Q_s^2/\Lambda^2} \int \frac{\mathrm{d}^2\boldsymbol{B}}{2\pi}\, e^{-i\boldsymbol{\Delta}\cdot\boldsymbol{B}}\, \frac{\ln 4/B^2\Lambda^2}{B^2}. \tag{F.11}$$

By performing the straightforward angular integration, we notice that the integral becomes logarithmic in the regime $2/Q_s \ll B \ll 2/\Delta_\perp$. After taking the large-N_c limit of the factor multiplying the integral in Eq. (F.1), we finally obtain

$$\frac{\mathrm{d}xG_{\mathbb{P}}^{\mathrm{inc}}}{\mathrm{d}^2\boldsymbol{\Delta}} \simeq \frac{S_\perp}{8\pi^4}\, \frac{1}{\ln Q_s^2/\Lambda^2} \left(\ln^2 \frac{Q_s^2}{\Lambda^2} - \ln^2 \frac{\Delta_\perp^2}{\Lambda^2} \right) \quad \text{for} \quad x \ll 1 \quad \text{and} \quad \Delta_\perp \ll Q_s. \tag{F.12}$$

High momenta $\Delta_\perp \gg Q_s$

The dominant contribution is coming from dipoles with a small size B. More precisely, we observe a logarithmic enhancement in the region where $B \ll R \ll 2/Q_s$. Given that in this limit $\mathcal{S}(R) \simeq 1$ and $F, f, F - f \ll 1$, it follows that the correlator simplifies to $\mathcal{W}_g \simeq 2f^2/N_c^2$ within the 4-gluon exchange approximation. Expanding f in the regime $B \ll R$, we obtain

$$\mathcal{W}_g(\boldsymbol{R}, \boldsymbol{R}, \boldsymbol{B}) \simeq \frac{Q_A^4 R^4}{8N_c^2} \ln^2 \frac{4}{R^2\Lambda^2} + \frac{Q_A^4 B^2 R^2}{4N_c^2} \left(\ln^2 \frac{4}{R^2\Lambda^2} - \ln \frac{4}{B^2\Lambda^2} \ln \frac{4}{R^2\Lambda^2} \right). \tag{F.13}$$

The first term in this expression is independent of $\boldsymbol{B}$ and is not relevant to our analysis, as after the Fourier transform, cf. (F.1), it will result in a term proportional to $\delta^{(2)}(\boldsymbol{\Delta})$.[4] Substituting the second term of Eq. (F.13) into Eq. (F.5), we observe that the integration over R becomes logarithmic (in the regime $B \ll R \ll 2/Q_s$) and yields

$$\int \mathrm{d}^2\boldsymbol{k}\, \mathcal{G}_{\mathrm{inc}} \simeq -\frac{Q_A^4}{12N_c^2} \int \frac{\mathrm{d}^2\boldsymbol{B}}{2\pi}\, e^{-i\boldsymbol{\Delta}\cdot\boldsymbol{B}}\, B^2 \left(\ln^3 \frac{4}{B^2 Q_s^2} + 3 \ln \frac{Q_s^2}{\Lambda^2} \ln^2 \frac{4}{B^2 Q_s^2} \right). \tag{F.14}$$

The above expression is proportional to B^2, hence it follows directly from Eq. (F.12) that the incoherent DPDF must exhibit a $1/\Delta_\perp^4$ scaling behavior. Nevertheless, we emphasize that the logarithmic dependence on B in Eq. (F.14) is essential[5] to obtain a non-zero result for $\Delta_\perp \neq 0$, since

$$\int \frac{\mathrm{d}^2\boldsymbol{B}}{2\pi}\, e^{-i\boldsymbol{\Delta}\cdot\boldsymbol{B}} B^2 = -\nabla_\Delta^2 \int \frac{\mathrm{d}^2\boldsymbol{B}}{2\pi}\, e^{-i\boldsymbol{\Delta}\cdot\boldsymbol{B}} = -2\pi \nabla_\Delta^2 \delta^{(2)}(\boldsymbol{\Delta}). \tag{F.15}$$

Now, by performing the angular integration and making use of the integrals Eq. (A.1) and Eq. (A.2) together with the change of variables $B = \tilde{B}/\Delta_\perp$, we finally obtain the leading behavior

$$\frac{\mathrm{d}xG_{\mathbb{P}}^{\mathrm{inc}}}{\mathrm{d}^2\boldsymbol{\Delta}} \simeq \frac{S_\perp}{4\pi^4}\, \frac{Q_A^4}{\Delta_\perp^4} \left(\ln^2 \frac{\Delta_\perp^2}{\Lambda^2} - \ln^2 \frac{Q_s^2}{\Lambda^2} \right) \quad \text{for} \quad x \ll 1 \quad \text{and} \quad \Delta_\perp \gg Q_s. \tag{F.16}$$

[4]While such a term is significant for the cross section integrated over $\boldsymbol{\Delta}$, a proper evaluation of this contribution requires relaxing the assumption $R \ll 2/Q_s$.

[5]These logarithms originate from the logarithmic structure of the MV model amplitude. If the GBW model were used instead, no power-law tail would emerge at large $\Delta_\perp$, resulting in an unphysical distribution that decays exponentially for large $\Delta_\perp$.

F.2 The case $1 - x \ll 1$

When $1-x \ll 1$, we find that $\mathcal{M} \simeq k_\perp/\sqrt{1-x} \gg k_\perp$, leading to a suppression of the contribution from the region where $k_\perp R \gtrsim 1$, due to the rapid exponential decay of the K_2 Bessel functions. As a result, we can approximate $e^{-i\boldsymbol{k}\cdot(\boldsymbol{R}-\bar{\boldsymbol{R}})} \simeq 1$, allowing the integration over $\boldsymbol{k}$ to be performed analytically, yielding

$$\int \mathrm{d}^2\boldsymbol{k}\, \frac{\mathcal{G}_{\mathrm{inc}}}{1-x}\bigg|_{x=1} = \int \frac{\mathrm{d}^2\boldsymbol{B}}{2\pi}\, e^{-i\boldsymbol{\Delta}\cdot\boldsymbol{B}} \int \frac{\mathrm{d}^2\boldsymbol{R}}{2\pi} \int \frac{\mathrm{d}^2\bar{\boldsymbol{R}}}{2\pi}\, \frac{\Psi(\bar{R}/R)}{R^3\bar{R}^3} \cos 2\phi_{R\bar{R}}\, \mathcal{W}_g(\boldsymbol{R},\bar{\boldsymbol{R}},\boldsymbol{B}), \tag{F.17}$$

where we have defined the dimensionless function

$$\Psi(\rho) = \frac{16\rho}{(\rho^2-1)^5}\, \left(\rho^8 - 8\rho^6 + 8\rho^2 - 1 + 12\rho^4 \ln\rho^2\right). \tag{F.18}$$

As implicitly done in these expressions, we find convenient to introduce a change of variables from the size $\bar{R}$ to the ratio $\rho \equiv \bar{R}/R$. By definition, the function in Eq. (F.18) satisfies the symmetry property $\Psi(1/\rho) = \Psi(\rho)$, as the initial integral remains unchanged under the exchange $R \leftrightarrow \bar{R}$. Exploiting this symmetry, we restrict the integration to the region $\bar{R} < R \Leftrightarrow \rho < 1$ and compensate by multiplying the result by a factor of 2. Additionally, it is useful to note that $\Psi(\rho) \simeq 16\rho$ for $\rho \ll 1$, while at $\rho = 1$, the function remains finite with $\Psi(1) = 32/5$.

Low momenta $\Delta_\perp \ll Q_s$

The dominant contributions arise from configurations where the sizes satisfy $B \gg 2/Q_s, R, \bar{R}$, without any additional strict hierarchy between $2/Q_s$, R, and $\bar{R}$. As for F and $F - f$, their expressions remain as in Eq. (F.7), since only the largest scale B plays a role in their determination. In the expansion of f for $R, \bar{R} \ll B$, the leading term cancels, leading to

$$f \simeq -\frac{Q_A^2 \boldsymbol{R}\cdot\bar{\boldsymbol{R}}}{4} \ln\frac{4}{B^2\Lambda^2} = -\frac{Q_A^2 R^2}{4}\rho\cos\phi_{R\bar{R}} \ln\frac{4}{B^2\Lambda^2}. \tag{F.19}$$

Eq. (F.2) becomes

$$\mathcal{W}_g(\boldsymbol{R},\bar{\boldsymbol{R}},\boldsymbol{B}) \simeq \frac{1}{N_c^2}\, Q_A^2 R^4 \mathcal{S}_g(R)\mathcal{S}_g(\rho R)\rho^2\cos^2\phi_{R\bar{R}}\, \frac{\ln 4/B^2\Lambda^2}{B^2}, \tag{F.20}$$

allowing for a straightforward evaluation of the two angular integrations, for instance by choosing $\phi_{R\bar{R}}$ and the angle between $\boldsymbol{B}$ and $\boldsymbol{R}$ as independent variables, leading to

$$\int \mathrm{d}^2\boldsymbol{k}\, \frac{\mathcal{G}_{\mathrm{inc}}}{1-x}\bigg|_{x=1} \simeq \frac{Q_A^2}{4N_c^2} \int \frac{\mathrm{d}^2\boldsymbol{B}}{2\pi}\, e^{-i\boldsymbol{\Delta}\cdot\boldsymbol{B}}\, \frac{\ln 4/B^2\Lambda^2}{B^2} \int_0^1 \mathrm{d}\rho\, \Psi(\rho) \int_0^\infty \mathrm{d}R^2 \mathcal{S}_g(R)\mathcal{S}_g(\rho R). \tag{F.21}$$

The remaining integrations over R and ρ can be carried out directly, yielding

$$\int_0^\infty \mathrm{d}R^2 \mathcal{S}_g(R)\mathcal{S}_g(\rho R) \simeq \frac{4}{(1+\rho^2)Q_s^2} \qquad \text{and} \qquad \int_0^1 \mathrm{d}\rho\, \frac{\Psi(\rho)}{1+\rho^2} = \frac{3\pi^2 - 16}{4}, \tag{F.22}$$

so that Eq. (F.21) becomes

$$\int \mathrm{d}^2\boldsymbol{k}\, \frac{\mathcal{G}_{\mathrm{inc}}}{1-x}\bigg|_{x=1} \simeq \frac{3\pi^2-16}{4N_c^2}\frac{1}{\ln Q_s^2/\Lambda^2} \int \frac{\mathrm{d}^2\boldsymbol{B}}{2\pi}\, e^{-i\boldsymbol{\Delta}\cdot\boldsymbol{B}}\, \frac{\ln 4/B^2\Lambda^2}{B^2}, \tag{F.23}$$

where we have once again used $Q_s^2 = Q_A^2 \ln Q_s^2/\Lambda^2$. The last integral is the same as the one found in Eq. (F.11). Taking the large-N_c limit of the prefactor in Eq. (F.1), we obtain

$$\frac{\mathrm{d}xG_{\mathbb{P}}^{\mathrm{inc}}}{\mathrm{d}^2\boldsymbol{\Delta}} \simeq \frac{S_\perp}{8\pi^4}\,\frac{3\pi^2-16}{16}\,\frac{1}{\ln Q_s^2/\Lambda^2}\left(\ln^2\frac{Q_s^2}{\Lambda^2} - \ln^2\frac{\Delta_\perp^2}{\Lambda^2}\right) \quad \text{for} \quad 1-x \ll 1 \quad \text{and} \quad \Delta_\perp \ll Q_s. \tag{F.24}$$

We observe that the above expression, along with the corresponding one for $x \ll 1$ in Eq. (F.12), share the same functional form, and the numerical values of their respective coefficients are not very far from each other.

High momenta $\Delta_\perp \gg Q_s$

This is the most intricate calculation of the Appendix, and we will provide a brief summary by highlighting the key steps. The relevant configurations are those that satisfy the strong ordering $B \ll R, \bar{R} \ll 2/Q_s$, with no additional constraint between R and $\bar{R}$. The correlator in Eq. (F.2) simplifies to $\mathcal{W}_g \simeq 2f^2/N_c^2$, with

$$\begin{aligned} f \to -\frac{Q_A^2}{8}\Bigg\{ & R^2 \ln\frac{4}{R^2\Lambda^2} + \bar{R}^2 \ln\frac{4}{\bar{R}^2\Lambda^2} - (\boldsymbol{R}-\bar{\boldsymbol{R}})^2 \ln\frac{4}{(\boldsymbol{R}-\bar{\boldsymbol{R}})^2\Lambda^2} \\ & + B^2\left[\ln\frac{4}{R^2\Lambda^2} + \ln\frac{4}{\bar{R}^2\Lambda^2} - \ln\frac{4}{B^2\Lambda^2} - \ln\frac{4}{(\boldsymbol{R}-\bar{\boldsymbol{R}})^2\Lambda^2}\right]\Bigg\}. \end{aligned} \tag{F.25}$$

We want to point out that f contains a linear term in $\boldsymbol{B}$, but it has not been included since it can be shown that it does not contribute. When squaring f, we notice that only the "cross term" in the r.h.s. in Eq. (F.25) is of our interest, since it is the one proportional to B^2. Hence, the correlator gives

$$\begin{aligned} \mathcal{W}_g(\boldsymbol{R},\bar{\boldsymbol{R}},\boldsymbol{B}) \to \frac{Q_A^4 B^2 R^2}{16N_c^2} & \left[2\rho\cos\phi_{R\bar{R}}\,\ln\frac{4}{R^2\Lambda^2} + \big(1-2\rho\cos\phi_{R\bar{R}}+\rho^2\big)\ln\big(1-2\rho\cos\phi_{R\bar{R}}+\rho^2\big)\right] \\ & \times\left[\ln\frac{B^2}{R^2} + \ln\big(1-2\rho\cos\phi_{R\bar{R}}+\rho^2\big)\right], \end{aligned} \tag{F.26}$$

where we have omitted terms involving $\ln\rho^2$ since, in the regime where $\rho \ll 1$, they do not contribute to any logarithmic enhancement. Only logarithmic terms that involve two among the rather different scales B, R, and $2/\Lambda$ are significant. Furthermore, when expanding the product of the two brackets in Eq. (F.26), only the terms linear in $\ln\big(1-2\rho\cos\phi_{R\bar{R}}+\rho^2\big)$ remain relevant. The term without this logarithm vanishes upon angular integration, while the quadratic term is not logarithmically enhanced. As a result, Eq. (F.26) simplifies to

$$\mathcal{W}_g(\boldsymbol{R},\bar{\boldsymbol{R}},\boldsymbol{B}) \to \frac{Q_A^4 B^2 R^2}{16N_c^2}\left[2\rho\cos\phi_{R\bar{R}}\,\ln\frac{4}{B^2\Lambda^2} + \big(1+\rho^2\big)\ln\frac{B^2}{R^2}\right]\ln\big(1-2\rho\cos\phi_{R\bar{R}}+\rho^2\big). \tag{F.27}$$

Substituting the above into Eq. (F.17) and doing the angular integrations we obtain

$$\begin{aligned} \int \mathrm{d}^2\boldsymbol{k}\,\frac{\mathcal{G}_{\mathrm{inc}}}{1-x}\bigg|_{x=1} \simeq & \frac{Q_A^4}{32N_c^2}\int\frac{\mathrm{d}^2\boldsymbol{B}}{2\pi}\,e^{-i\boldsymbol{\Delta}\cdot\boldsymbol{B}}B^2 \\ & \times\int_{B^2}^{4/Q_s^2}\frac{\mathrm{d}R^2}{R^2}\int_0^1\mathrm{d}\rho\,\Psi(\rho)\left[(1+\rho^2)\ln\frac{R^2}{B^2} - \frac{2}{3}(3+\rho^2)\ln\frac{4}{B^2\Lambda^2}\right]. \end{aligned} \tag{F.28}$$

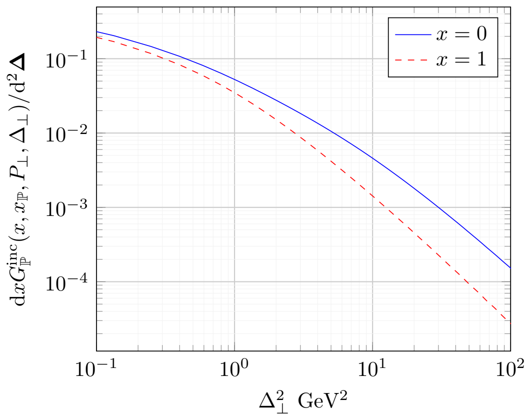

Figure F.1: The incoherent gluon DPDF as function of the momentum transfer $\Delta_\perp^2$ for $x = 0$ and $x = 1$. As in Fig. 6.5, a factor $S_\perp/4\pi^3$ has been omitted and the scattering amplitude is given by the MV model with a gluon saturation scale $Q_s^2 = 2\,\mathrm{GeV}^2$.

In principle, the lower limit of the integration over ρ is $B/R \ll 1$. However, it has been safely set to zero since, in this regime, the integrand is proportional to ρ. This allows for a simple integration, which yields

$$\int \mathrm{d}^2\boldsymbol{k}\, \frac{\mathcal{G}_{\mathrm{inc}}}{1-x}\bigg|_{x=1} \simeq \frac{Q_A^4}{24N_c^2} \int \frac{\mathrm{d}^2\boldsymbol{B}}{2\pi}\, e^{-i\boldsymbol{\Delta}\cdot\boldsymbol{B}} B^2 \int_{B^2}^{4/Q_s^2} \frac{\mathrm{d}R^2}{R^2} \left(5\ln\frac{R^2}{B^2} - 8\ln\frac{4}{B^2\Lambda^2}\right). \tag{F.29}$$

The logarithmic integration over R^2 leads to

$$\int \mathrm{d}^2\boldsymbol{k}\, \frac{\mathcal{G}_{\mathrm{inc}}}{1-x}\bigg|_{x=1} \simeq -\frac{Q_A^4}{48N_c^2} \int \frac{\mathrm{d}^2\boldsymbol{B}}{2\pi}\, e^{-i\boldsymbol{\Delta}\cdot\boldsymbol{B}} B^2 \left(11\ln^2\frac{4}{B^2Q_s^2} + 16\ln\frac{Q_s^2}{\Lambda^2}\ln\frac{4}{B^2Q_s^2}\right). \tag{F.30}$$

It remains to follow the steps as in going from Eq. (F.14) to Eq. (F.16), and again with the help of Appendix A, we arrive at

$$\frac{\mathrm{d}xG_{\mathbb{P}}^{\mathrm{inc}}}{\mathrm{d}^2\boldsymbol{\Delta}} \simeq \frac{S_\perp}{8\pi^4}\frac{Q_A^4}{3\Delta_\perp^4}\left(11\ln\frac{\Delta_\perp^2}{\Lambda^2} - 3\ln\frac{Q_s^2}{\Lambda^2}\right) \quad \text{for} \quad 1-x \ll 1 \quad \text{and} \quad \Delta_\perp \gg Q_s. \tag{F.31}$$

The analytical estimates in the regimes $\Delta_\perp \ll Q_s$ and $\Delta_\perp \gg Q_s$ and near the end-points $x = 0$ and $x = 1$ provided in Eqs. (F.12), (F.16), (F.24) and (F.31) are confirmed by numerical calculations presented in Fig. F.1.

To conclude this Appendix, we would like to compare the coherent and incoherent DPDF x-dependence in the limit where x is close to one. First, to perform the integration over the gluon transverse momentum, leading to Eq. (F.17), one can introduce a change of variable from $k_\perp$ to $\mathcal{M}$ using the relation $k_\perp^2 \simeq (1-x)\mathcal{M}^2$. Since $\mathcal{M}$ sets the scale in the argument of the K_2 Bessel functions and the phase factor $e^{-i\boldsymbol{k}\cdot(\boldsymbol{R}-\bar{\boldsymbol{R}})} \simeq 1$, the only explicit dependence on $1-x$ arises from the change in the integration measure, i.e., $\mathrm{d}k_\perp^2 \simeq (1-x)\mathrm{d}\mathcal{M}^2$. This factor of $1-x$ cancels the corresponding term in the denominator of Eq. (6.16), ultimately rendering the incoherent DPDF independent of $1-x$.

However, it is crucial to note that the integrand in Eq. (F.17) contains an oscillatory factor $\cos 2\phi_{R\bar{R}}$. The reason a nonzero result is obtained upon angular integration is the additional dependence on $\cos 2\phi_{R\bar{R}}$ (or equivalently $\cos^2 \phi_{R\bar{R}}$) introduced by the CGC scattering correlator $\mathcal{W}_g(\boldsymbol{R}, \bar{\boldsymbol{R}}, \boldsymbol{B})$, as seen in Eqs. (F.20) and (F.27). This behavior contrasts with the case of the coherent DPDF, where the corresponding correlator, $\mathcal{T}_g(R)\mathcal{T}_g(\bar{R})$, is independent of the angle. To obtain a nonzero result, the exponential $e^{-i\boldsymbol{k}\cdot(\boldsymbol{R}-\bar{\boldsymbol{R}})}$ must be expanded to fourth order to generate the required angular dependence [55]. When applying the aforementioned change of variable to $\mathcal{M}^2$, the additional power of $k_\perp^4$ introduces a factor of $(1-x)^2$, which is transmitted to the coherent gluon DPDF. Similarly, for the quark DPDF, the integrand involves $\cos \phi_{R\bar{R}}$, meaning that it suffices to expand $e^{-i\boldsymbol{k}\cdot(\boldsymbol{R}-\bar{\boldsymbol{R}})}$ only to second order. In this case, the extra power of $k_\perp^2$ results in a multiplicative factor of $1 - x$ [60].

Bibliography

[1] L. N. Lipatov, "Reggeization of the Vector Meson and the Vacuum Singularity in Non-abelian Gauge Theories," *Sov. J. Nucl. Phys.*, vol. 23, pp. 338–345, 1976.

[2] E. A. Kuraev, L. N. Lipatov, and V. S. Fadin, "The Pomeranchuk Singularity in Non-abelian Gauge Theories," *Sov. Phys. JETP*, vol. 45, pp. 199–204, 1977.

[3] I. I. Balitsky and L. N. Lipatov, "The Pomeranchuk Singularity in Quantum Chromodynamics," *Sov. J. Nucl. Phys.*, vol. 28, pp. 822–829, 1978.

[4] A. H. Mueller, "Soft gluons in the infinite momentum wave function and the BFKL pomeron," *Nucl. Phys. B*, vol. 415, pp. 373–385, 1994. DOI: 10.1016/0550-3213(94)90116-3.

[5] L. V. Gribov, E. M. Levin, and M. G. Ryskin, "Semihard Processes in QCD," *Phys. Rept.*, vol. 100, pp. 1–150, 1983. DOI: 10.1016/0370-1573(83)90022-4.

[6] A. H. Mueller and J.-w. Qiu, "Gluon Recombination and Shadowing at Small Values of x," *Nucl. Phys. B*, vol. 268, pp. 427–452, 1986. DOI: 10.1016/0550-3213(86)90164-1.

[7] K. J. Golec-Biernat and M. Wusthoff, "Saturation in diffractive deep inelastic scattering," *Phys. Rev. D*, vol. 60, p. 114 023, 1999. DOI: 10.1103/PhysRevD.60.114023. arXiv: hep-ph/9903358.

[8] D. N. Triantafyllopoulos, "The Energy dependence of the saturation momentum from RG improved BFKL evolution," *Nucl. Phys. B*, vol. 648, pp. 293–316, 2003. DOI: 10.1016/S0550-3213(02)01000-3. arXiv: hep-ph/0209121.

[9] F. Gelis, E. Iancu, J. Jalilian-Marian, and R. Venugopalan, "The Color Glass Condensate," *Ann. Rev. Nucl. Part. Sci.*, vol. 60, pp. 463–489, 2010. DOI: 10.1146/annurev.nucl.010909.083629. arXiv: 1002.0333 [hep-ph].

[10] Y. V. Kovchegov and E. Levin, *Quantum Chromodynamics at High Energy.* Oxford University Press, 2013, vol. 33. DOI: 10.1017/9781009291446.

[11] I. Balitsky, "Operator expansion for high-energy scattering," *Nucl. Phys. B*, vol. 463, pp. 99–160, 1996. DOI: 10.1016/0550-3213(95)00638-9. arXiv: hep-ph/9509348.

[12] Y. V. Kovchegov, "Small x F(2) structure function of a nucleus including multiple pomeron exchanges," *Phys. Rev. D*, vol. 60, p. 034 008, 1999. DOI: 10.1103/PhysRevD.60.034008. arXiv: hep-ph/9901281.

[13] J. Jalilian-Marian, A. Kovner, A. Leonidov, and H. Weigert, "The Wilson renormalization group for low x physics: Towards the high density regime," *Phys. Rev. D*, vol. 59, p. 014 014, 1998. DOI: 10.1103/PhysRevD.59.014014. arXiv: hep-ph/9706377.

[14] J. Jalilian-Marian, A. Kovner, A. Leonidov, and H. Weigert, "The BFKL equation from the Wilson renormalization group," *Nucl. Phys. B*, vol. 504, pp. 415–431, 1997. DOI: 10.1016/S0550-3213(97)00440-9. arXiv: hep-ph/9701284.

[15] H. Weigert, "Unitarity at small Bjorken x," *Nucl. Phys. A*, vol. 703, pp. 823–860, 2002. DOI: 10.1016/S0375-9474(01)01668-2. arXiv: hep-ph/0004044.

[16] E. Iancu, A. Leonidov, and L. D. McLerran, "Nonlinear gluon evolution in the color glass condensate. 1.," *Nucl. Phys. A*, vol. 692, pp. 583–645, 2001. DOI: 10.1016/S0375-9474(01)00642-X. arXiv: hep-ph/0011241.

[17] A. Kovner, J. G. Milhano, and H. Weigert, "Relating different approaches to nonlinear QCD evolution at finite gluon density," *Phys. Rev. D*, vol. 62, p. 114 005, 2000. DOI: 10.1103/PhysRevD.62.114005. arXiv: hep-ph/0004014.

[18] E. Iancu, A. Leonidov, and L. D. McLerran, "The Renormalization group equation for the color glass condensate," *Phys. Lett. B*, vol. 510, pp. 133–144, 2001. DOI: 10.1016/S0370-2693(01)00524-X. arXiv: hep-ph/0102009.

[19] E. Ferreiro, E. Iancu, A. Leonidov, and L. McLerran, "Nonlinear gluon evolution in the color glass condensate. 2.," *Nucl. Phys. A*, vol. 703, pp. 489–538, 2002. DOI: 10.1016/S0375-9474(01)01329-X. arXiv: hep-ph/0109115.

[20] E. Iancu, A. H. Mueller, D. N. Triantafyllopoulos, and S. Y. Wei, "Saturation effects in SIDIS at very forward rapidities," *JHEP*, vol. 07, p. 196, 2021. DOI: 10.1007/JHEP07(2021)196. arXiv: 2012.08562 [hep-ph].

[21] F. Bergabo and J. Jalilian-Marian, "Single inclusive hadron production in DIS at small x: next to leading order corrections," *JHEP*, vol. 01, p. 095, 2023. DOI: 10.1007/JHEP01(2023)095. arXiv: 2210.03208 [hep-ph].

[22] P. Caucal, E. Ferrand, and F. Salazar, "Semi-inclusive single-jet production in DIS at next-to-leading order in the Color Glass Condensate," *JHEP*, vol. 05, p. 110, 2024. DOI: 10.1007/JHEP05(2024)110. arXiv: 2401.01934 [hep-ph].

[23] P. Caucal and E. Iancu, "The evolution of the transverse-momentum dependent gluon distribution at small x," Jun. 2024. arXiv: 2406.04238 [hep-ph].

[24] T. Altinoluk, J. Jalilian-Marian, and C. Marquet, "Sudakov double logs in single-inclusive hadron production in DIS at small x from the color glass condensate formalism," *Phys. Rev. D*, vol. 110, no. 9, p. 094 056, 2024. DOI: 10.1103/PhysRevD.110.094056. arXiv: 2406.08277 [hep-ph].

[25] C. Marquet, "Forward inclusive dijet production and azimuthal correlations in p(A) collisions," *Nucl. Phys. A*, vol. 796, pp. 41–60, 2007. DOI: 10.1016/j.nuclphysa.2007.09.001. arXiv: 0708.0231 [hep-ph].

[26] A. Metz and J. Zhou, "Distribution of linearly polarized gluons inside a large nucleus," *Phys. Rev. D*, vol. 84, p. 051 503, 2011. DOI: 10.1103/PhysRevD.84.051503. arXiv: 1105.1991 [hep-ph].

[27] F. Dominguez, J.-W. Qiu, B.-W. Xiao, and F. Yuan, "On the linearly polarized gluon distributions in the color dipole model," *Phys. Rev. D*, vol. 85, p. 045 003, 2012. DOI: 10.1103/PhysRevD.85.045003. arXiv: 1109.6293 [hep-ph].

[28] A. H. Mueller, B.-W. Xiao, and F. Yuan, "Sudakov double logarithms resummation in hard processes in the small-x saturation formalism," *Phys. Rev. D*, vol. 88, no. 11, p. 114 010, 2013. DOI: 10.1103/PhysRevD.88.114010. arXiv: 1308.2993 [hep-ph].

[29] P. Kotko, K. Kutak, C. Marquet, E. Petreska, S. Sapeta, and A. van Hameren, "Improved TMD factorization for forward dijet production in dilute-dense hadronic collisions," *JHEP*, vol. 09, p. 106, 2015. DOI: 10.1007/JHEP09(2015)106. arXiv: 1503.03421 [hep-ph].

[30] A. Dumitru, T. Lappi, and V. Skokov, “Distribution of Linearly Polarized Gluons and Elliptic Azimuthal Anisotropy in Deep Inelastic Scattering Dijet Production at High Energy,” *Phys. Rev. Lett.*, vol. 115, no. 25, p. 252 301, 2015. DOI: 10.1103/PhysRevLett.115.252301. arXiv: 1508.04438 [hep-ph].

[31] P. Kotko, K. Kutak, S. Sapeta, A. M. Stasto, and M. Strikman, “Estimating nonlinear effects in forward dijet production in ultra-peripheral heavy ion collisions at the LHC,” *Eur. Phys. J. C*, vol. 77, no. 5, p. 353, 2017. DOI: 10.1140/epjc/s10052-017-4906-6. arXiv: 1702.03063 [hep-ph].

[32] A. Dumitru, V. Skokov, and T. Ullrich, “Measuring the Weizsäcker-Williams distribution of linearly polarized gluons at an electron-ion collider through dijet azimuthal asymmetries,” *Phys. Rev. C*, vol. 99, no. 1, p. 015 204, 2019. DOI: 10.1103/PhysRevC.99.015204. arXiv: 1809.02615 [hep-ph].

[33] S. R. Klein and H. Mäntysaari, “Imaging the nucleus with high-energy photons,” *Nature Rev. Phys.*, vol. 1, no. 11, pp. 662–674, 2019. DOI: 10.1038/s42254-019-0107-6. arXiv: 1910.10858 [hep-ex].

[34] H. Mäntysaari, N. Mueller, F. Salazar, and B. Schenke, “Multigluon Correlations and Evidence of Saturation from Dijet Measurements at an Electron-Ion Collider,” *Phys. Rev. Lett.*, vol. 124, no. 11, p. 112 301, 2020. DOI: 10.1103/PhysRevLett.124.112301. arXiv: 1912.05586 [nucl-th].

[35] E. Iancu and Y. Mulian, “Forward dijets in proton-nucleus collisions at next-to-leading order: the real corrections,” *JHEP*, vol. 03, p. 005, 2021. DOI: 10.1007/JHEP03(2021)005. arXiv: 2009.11930 [hep-ph].

[36] Y. Hatta, B.-W. Xiao, F. Yuan, and J. Zhou, “Azimuthal angular asymmetry of soft gluon radiation in jet production,” *Phys. Rev. D*, vol. 104, no. 5, p. 054 037, 2021. DOI: 10.1103/PhysRevD.104.054037. arXiv: 2106.05307 [hep-ph].

[37] R. Boussarie, H. Mäntysaari, F. Salazar, and B. Schenke, “The importance of kinematic twists and genuine saturation effects in dijet production at the Electron-Ion Collider,” *JHEP*, vol. 09, p. 178, 2021. DOI: 10.1007/JHEP09(2021)178. arXiv: 2106.11301 [hep-ph].

[38] P. Caucal, F. Salazar, and R. Venugopalan, “Dijet impact factor in DIS at next-to-leading order in the Color Glass Condensate,” *JHEP*, vol. 11, p. 222, 2021. DOI: 10.1007/JHEP11(2021)222. arXiv: 2108.06347 [hep-ph].

[39] P. Taels, T. Altinoluk, G. Beuf, and C. Marquet, “Dijet photoproduction at low x at next-to-leading order and its back-to-back limit,” *JHEP*, vol. 10, p. 184, 2022. DOI: 10.1007/JHEP10(2022)184. arXiv: 2204.11650 [hep-ph].

[40] P. Caucal, F. Salazar, B. Schenke, T. Stebel, and R. Venugopalan, “Back-to-Back Inclusive Dijets in Deep Inelastic Scattering at Small x: Complete NLO Results and Predictions,” *Phys. Rev. Lett.*, vol. 132, no. 8, p. 081 902, 2024. DOI: 10.1103/PhysRevLett.132.081902. arXiv: 2308.00022 [hep-ph].

[41] J. L. Albacete and C. Marquet, “Azimuthal correlations of forward di-hadrons in d+Au collisions at RHIC in the Color Glass Condensate,” *Phys. Rev. Lett.*, vol. 105, p. 162 301, 2010. DOI: 10.1103/PhysRevLett.105.162301. arXiv: 1005.4065 [hep-ph].

[42] A. Stasto, B.-W. Xiao, and F. Yuan, “Back-to-Back Correlations of Di-hadrons in dAu Collisions at RHIC,” *Phys. Lett. B*, vol. 716, pp. 430–434, 2012. DOI: 10.1016/j.physletb.2012.08.044. arXiv: 1109.1817 [hep-ph].

[43] E. Iancu and J. Laidet, "Gluon splitting in a shockwave," *Nucl. Phys. A*, vol. 916, pp. 48–78, 2013. DOI: 10.1016/j.nuclphysa.2013.07.012. arXiv: 1305.5926 [hep-ph].

[44] L. Zheng, E. C. Aschenauer, J. H. Lee, and B.-W. Xiao, "Probing Gluon Saturation through Dihadron Correlations at an Electron-Ion Collider," *Phys. Rev. D*, vol. 89, no. 7, p. 074 037, 2014. DOI: 10.1103/PhysRevD.89.074037. arXiv: 1403.2413 [hep-ph].

[45] J. L. Albacete, G. Giacalone, C. Marquet, and M. Matas, "Forward dihadron back-to-back correlations in pA collisions," *Phys. Rev. D*, vol. 99, no. 1, p. 014 002, 2019. DOI: 10.1103/PhysRevD.99.014002. arXiv: 1805.05711 [hep-ph].

[46] F. Bergabo and J. Jalilian-Marian, "One-loop corrections to dihadron production in DIS at small x," *Phys. Rev. D*, vol. 106, no. 5, p. 054 035, 2022. DOI: 10.1103/PhysRevD.106.054035. arXiv: 2207.03606 [hep-ph].

[47] S. Benić and A. Dumitru, "Prompt photon - jet angular correlations at central rapidities in p+A collisions," *Phys. Rev. D*, vol. 97, no. 1, p. 014 012, 2018. DOI: 10.1103/PhysRevD.97.014012. arXiv: 1710.01991 [hep-ph].

[48] J. Bartels, H. Jung, and M. Wusthoff, "Quark - anti-quark gluon jets in DIS diffractive dissociation," *Eur. Phys. J. C*, vol. 11, pp. 111–125, 1999. DOI: 10.1007/s100520050618. arXiv: hep-ph/9903265.

[49] T. Altinoluk, N. Armesto, G. Beuf, and A. H. Rezaeian, "Diffractive Dijet Production in Deep Inelastic Scattering and Photon-Hadron Collisions in the Color Glass Condensate," *Phys. Lett. B*, vol. 758, pp. 373–383, 2016. DOI: 10.1016/j.physletb.2016.05.032. arXiv: 1511.07452 [hep-ph].

[50] Y. Hatta, B.-W. Xiao, and F. Yuan, "Probing the Small- x Gluon Tomography in Correlated Hard Diffractive Dijet Production in Deep Inelastic Scattering," *Phys. Rev. Lett.*, vol. 116, no. 20, p. 202 301, 2016. DOI: 10.1103/PhysRevLett.116.202301. arXiv: 1601.01585 [hep-ph].

[51] F. Salazar and B. Schenke, "Diffractive dijet production in impact parameter dependent saturation models," *Phys. Rev. D*, vol. 100, no. 3, p. 034 007, 2019. DOI: 10.1103/PhysRevD.100.034007. arXiv: 1905.03763 [hep-ph].

[52] E. Iancu, A. H. Mueller, and D. N. Triantafyllopoulos, "Probing Parton Saturation and the Gluon Dipole via Diffractive Jet Production at the Electron-Ion Collider," *Phys. Rev. Lett.*, vol. 128, no. 20, p. 202 001, 2022. DOI: 10.1103/PhysRevLett.128.202001. arXiv: 2112.06353 [hep-ph].

[53] Y. Hatta, B.-W. Xiao, and F. Yuan, "Semi-inclusive diffractive deep inelastic scattering at small x," *Phys. Rev. D*, vol. 106, no. 9, p. 094 015, 2022. DOI: 10.1103/PhysRevD.106.094015. arXiv: 2205.08060 [hep-ph].

[54] G. Beuf, H. Hänninen, T. Lappi, Y. Mulian, and H. Mäntysaari, "Diffractive deep inelastic scattering at NLO in the dipole picture: The qq¯g contribution," *Phys. Rev. D*, vol. 106, no. 9, p. 094 014, 2022. DOI: 10.1103/PhysRevD.106.094014. arXiv: 2206.13161 [hep-ph].

[55] E. Iancu, A. H. Mueller, D. N. Triantafyllopoulos, and S. Y. Wei, "Gluon dipole factorisation for diffractive dijets," *JHEP*, vol. 10, p. 103, 2022. DOI: 10.1007/JHEP10(2022)103. arXiv: 2207.06268 [hep-ph].

[56] E. Iancu, A. H. Mueller, D. N. Triantafyllopoulos, and S. Y. Wei, "Probing gluon saturation via diffractive jets in ultra-peripheral nucleus-nucleus collisions," *Eur. Phys. J. C*, vol. 83, no. 11, p. 1078, 2023. DOI: 10.1140/epjc/s10052-023-12165-8. arXiv: 2304.12401 [hep-ph].

[57] X.-B. Tong, B.-W. Xiao, and Y.-Y. Zhang, "Harmonics of lepton-jet correlations in inclusive and diffractive scatterings," *Phys. Rev. D*, vol. 109, no. 5, p. 054 004, 2024. DOI: 10.1103/PhysRevD.109.054004. arXiv: 2310.20662 [hep-ph].

[58] T. Kar, A. Kovner, M. Li, and V. V. Skokov, "Incoherent diffractive dijet production and gluon Bose enhancement in the nuclear wave function," *JHEP*, vol. 07, p. 134, 2024. DOI: 10.1007/JHEP07(2024)134. arXiv: 2312.04493 [hep-ph].

[59] D. Y. Shao, Y. Shi, C. Zhang, J. Zhou, and Y.-j. Zhou, "Revisiting azimuthal angular asymmetries in diffractive di-jet production," *JHEP*, vol. 07, p. 189, 2024. DOI: 10.1007/JHEP07(2024)189. arXiv: 2402.05465 [hep-ph].

[60] S. Hauksson, E. Iancu, A. H. Mueller, D. N. Triantafyllopoulos, and S. Y. Wei, "TMD factorisation for diffractive jets in photon-nucleus interactions," *JHEP*, vol. 06, p. 180, 2024. DOI: 10.1007/JHEP06(2024)180. arXiv: 2402.14748 [hep-ph].

[61] C. Marquet and H. Weigert, "New observables to test the Color Glass Condensate beyond the large- N_c limit," *Nucl. Phys. A*, vol. 843, pp. 68–97, 2010. DOI: 10.1016/j.nuclphysa.2010.05.056. arXiv: 1003.0813 [hep-ph].

[62] S. Demirci, T. Lappi, and S. Schlichting, "Proton hot spots and exclusive vector meson production," *Phys. Rev. D*, vol. 106, no. 7, p. 074 025, 2022. DOI: 10.1103/PhysRevD.106.074025. arXiv: 2206.05207 [hep-ph].

[63] B. Rodriguez-Aguilar, D. N. Triantafyllopoulos, and S. Y. Wei, "Incoherent diffractive dijet production in electron DIS off nuclei at high energy," *Phys. Rev. D*, vol. 107, no. 11, p. 114 007, 2023. DOI: 10.1103/PhysRevD.107.114007. arXiv: 2302.01106 [hep-ph].

[64] B. Rodriguez-Aguilar, D. N. Triantafyllopoulos, and S. Y. Wei, "Incoherent diffractive production of jets in electron DIS off nuclei at high energy," *Phys. Rev. D*, vol. 110, no. 7, p. 074 018, 2024. DOI: 10.1103/PhysRevD.110.074018. arXiv: 2407.17665 [hep-ph].

[65] C.-N. Yang and R. L. Mills, "Conservation of Isotopic Spin and Isotopic Gauge Invariance," *Phys. Rev.*, vol. 96, J.-P. Hsu and D. Fine, Eds., pp. 191–195, 1954. DOI: 10.1103/PhysRev.96.191.

[66] H. Fritzsch, M. Gell-Mann, and H. Leutwyler, "Advantages of the Color Octet Gluon Picture," *Phys. Lett. B*, vol. 47, pp. 365–368, 1973. DOI: 10.1016/0370-2693(73)90625-4.

[67] D. J. Gross and F. Wilczek, "Ultraviolet Behavior of Nonabelian Gauge Theories," *Phys. Rev. Lett.*, vol. 30, J. C. Taylor, Ed., pp. 1343–1346, 1973. DOI: 10.1103/PhysRevLett.30.1343.

[68] S. Weinberg, "Nonabelian Gauge Theories of the Strong Interactions," *Phys. Rev. Lett.*, vol. 31, pp. 494–497, 1973. DOI: 10.1103/PhysRevLett.31.494.

[69] V. N. Gribov, B. L. Ioffe, and I. Y. Pomeranchuk, "What is the range of interactions at high-energies (На Каких Расстояниях Происходит Взаимодействие При Высоких Энергиях?)" *Yad. Fiz.*, vol. 2, pp. 768–776, 1965. [Online]. Available: https://elib.biblioatom.ru/text/pomeranchuk_sobranie-trudov_t3_1972/p381/.

[70] B. L. Ioffe, "Space-time picture of γ-quantum scattering by nucleons at high energies," *Pisma Zh. Eksp. Teor. Fiz.*, vol. 9, p. 163, 2 1969. [Online]. Available: http://jetpletters.ru/ps/1658/article_25299.shtml.

[71] B. L. Ioffe, "Longitudinal distances in gamma quantum scattering and asymptotic electroproduction cross sections," *Pisma Zh. Eksp. Teor. Fiz.*, vol. 10, p. 143, 3 1969. [Online]. Available: http://jetpletters.ru/ps/1688/article_25703.shtml.

[72] B. L. Ioffe, "Space-time picture of photon and neutrino scattering and electroproduction cross-section asymptotics," *Phys. Lett. B*, vol. 30, pp. 123–125, 1969. DOI: 10.1016/0370-2693(69)90415-8.

[73] V. N. Gribov, "Interaction of gamma quanta and electrons with nuclei at high-energies," *Zh. Eksp. Teor. Fiz.*, vol. 57, pp. 1306–1323, 1969.

[74] J. D. Bjorken and J. B. Kogut, "Correspondence Arguments for High-Energy Collisions," *Phys. Rev. D*, vol. 8, p. 1341, 1973. DOI: 10.1103/PhysRevD.8.1341.

[75] B. Z. Kopeliovich, L. I. Lapidus, and A. B. Zamolodchikov, "Dynamics of Color in Hadron Diffraction on Nuclei," *JETP Lett.*, vol. 33, pp. 595–597, 1981.

[76] G. Bertsch, S. J. Brodsky, A. S. Goldhaber, and J. F. Gunion, "Diffractive Excitation in QCD," *Phys. Rev. Lett.*, vol. 47, p. 297, 1981. DOI: 10.1103/PhysRevLett.47.297.

[77] A. H. Mueller, "Small x Behavior and Parton Saturation: A QCD Model," *Nucl. Phys. B*, vol. 335, pp. 115–137, 1990. DOI: 10.1016/0550-3213(90)90173-B.

[78] Y. V. Kovchegov, "Quantum structure of the nonAbelian Weizsacker-Williams field for a very large nucleus," *Phys. Rev. D*, vol. 55, pp. 5445–5455, 1997. DOI: 10.1103/PhysRevD.55.5445. arXiv: hep-ph/9701229.

[79] G. P. Salam, "A Resummation of large subleading corrections at small x," *JHEP*, vol. 07, p. 019, 1998. DOI: 10.1088/1126-6708/1998/07/019. arXiv: hep-ph/9806482.

[80] M. Ciafaloni and D. Colferai, "The BFKL equation at next-to-leading level and beyond," *Phys. Lett. B*, vol. 452, pp. 372–378, 1999. DOI: 10.1016/S0370-2693(99)00281-6. arXiv: hep-ph/9812366.

[81] M. Ciafaloni, D. Colferai, and G. P. Salam, "Renormalization group improved small x equation," *Phys. Rev. D*, vol. 60, p. 114 036, 1999. DOI: 10.1103/PhysRevD.60.114036. arXiv: hep-ph/9905566.

[82] V. N. Gribov and L. N. Lipatov, "Deep inelastic e p scattering in perturbation theory," *Sov. J. Nucl. Phys.*, vol. 15, pp. 438–450, 1972.

[83] G. Altarelli and G. Parisi, "Asymptotic Freedom in Parton Language," *Nucl. Phys. B*, vol. 126, pp. 298–318, 1977. DOI: 10.1016/0550-3213(77)90384-4.

[84] Y. L. Dokshitzer, "Calculation of the Structure Functions for Deep Inelastic Scattering and e+ e- Annihilation by Perturbation Theory in Quantum Chromodynamics.," *Sov. Phys. JETP*, vol. 46, pp. 641–653, 1977.

[85] T. Regge, "Introduction to complex orbital momenta," *Nuovo Cim.*, vol. 14, p. 951, 1959. DOI: 10.1007/BF02728177.

[86] T. Regge, "Bound states, shadow states and Mandelstam representation," *Nuovo Cim.*, vol. 18, pp. 947–956, 1960. DOI: 10.1007/BF02733035.

[87] J. R. Forshaw and D. A. Ross, *Quantum Chromodynamics and the Pomeron*. Oxford University Press, 1998, vol. 9. DOI: 10.1017/9781009290111.

[88] P. D. B. Collins, *An Introduction to Regge Theory and High Energy Physics* (Cambridge Monographs on Mathematical Physics). Cambridge University Press, Jul. 2023. DOI: 10.1017/9781009403269.

[89] F. Gelis, T. Lappi, and R. Venugopalan, "High energy scattering in Quantum Chromodynamics," *Int. J. Mod. Phys. E*, vol. 16, D. Peres Menezes, M. Chiapparini, M. J. Menon, and S. dos Santos Avancini, Eds., pp. 2595–2637, 2007. DOI: 10.1142/S0218301307008331. arXiv: 0708.0047 [hep-ph].

[90] A.-K. Angelopoulou, A. D. Le, and S. Munier, "Scattering from an external field in quantum chromodynamics at high energies: from foundations to interdisciplinary connections," Nov. 2023. arXiv: 2311.14796 [hep-ph].

[91] F. Gelis, *Quantum Field Theory.* Cambridge University Press, Jul. 2019.

[92] J. D. Bjorken, J. B. Kogut, and D. E. Soper, "Quantum Electrodynamics at Infinite Momentum: Scattering from an External Field," *Phys. Rev. D*, vol. 3, p. 1382, 1971. DOI: 10.1103/PhysRevD.3.1382.

[93] E. Iancu and R. Venugopalan, "The Color glass condensate and high-energy scattering in QCD," in *Quark-gluon plasma 4*, R. C. Hwa and X.-N. Wang, Eds. Mar. 2003, pp. 249–3363. DOI: 10.1142/9789812795533_0005. arXiv: hep-ph/0303204.

[94] L. D. McLerran and R. Venugopalan, "Gluon distribution functions for very large nuclei at small transverse momentum," *Phys. Rev. D*, vol. 49, pp. 3352–3355, 1994. DOI: 10.1103/PhysRevD.49.3352. arXiv: hep-ph/9311205.

[95] L. D. McLerran and R. Venugopalan, "Computing quark and gluon distribution functions for very large nuclei," *Phys. Rev. D*, vol. 49, pp. 2233–2241, 1994. DOI: 10.1103/PhysRevD.49.2233. arXiv: hep-ph/9309289.

[96] A. Kovner, M. Lublinsky, and Y. Mulian, "Jalilian-Marian, Iancu, McLerran, Weigert, Leonidov, Kovner evolution at next to leading order," *Phys. Rev. D*, vol. 89, no. 6, p. 061 704, 2014. DOI: 10.1103/PhysRevD.89.061704. arXiv: 1310.0378 [hep-ph].

[97] A. Kovner, M. Lublinsky, and Y. Mulian, "NLO JIMWLK evolution unabridged," *JHEP*, vol. 08, p. 114, 2014. DOI: 10.1007/JHEP08(2014)114. arXiv: 1405.0418 [hep-ph].

[98] I. Balitsky and G. A. Chirilli, "Next-to-leading order evolution of color dipoles," *Phys. Rev. D*, vol. 77, p. 014 019, 2008. DOI: 10.1103/PhysRevD.77.014019. arXiv: 0710.4330 [hep-ph].

[99] B. Ducloué, E. Iancu, A. H. Mueller, G. Soyez, and D. N. Triantafyllopoulos, "Non-linear evolution in QCD at high-energy beyond leading order," *JHEP*, vol. 04, p. 081, 2019. DOI: 10.1007/JHEP04(2019)081. arXiv: 1902.06637 [hep-ph].

[100] B. Ducloué, E. Iancu, G. Soyez, and D. N. Triantafyllopoulos, "HERA data and collinearly-improved BK dynamics," *Phys. Lett. B*, vol. 803, p. 135 305, 2020. DOI: 10.1016/j.physletb.2020.135305. arXiv: 1912.09196 [hep-ph].

[101] V. Barone and E. Predazzi, *High-Energy Particle Diffraction* (Texts and Monographs in Physics). Berlin Heidelberg: Springer-Verlag, 2002, vol. v.565, ISBN: 978-3-540-42107-8.

[102] H. Mäntysaari, J. Penttala, F. Salazar, and B. Schenke, "Finite-size effects on small-x evolution and saturation in proton and nuclear targets," Nov. 2024. arXiv: 2411.13533 [hep-ph].

[103] H. Mäntysaari and B. Schenke, "Evidence of strong proton shape fluctuations from incoherent diffraction," *Phys. Rev. Lett.*, vol. 117, no. 5, p. 052 301, 2016. DOI: 10.1103/PhysRevLett.117.052301. arXiv: 1603.04349 [hep-ph].

[104] H. Mäntysaari and B. Schenke, "Revealing proton shape fluctuations with incoherent diffraction at high energy," *Phys. Rev. D*, vol. 94, no. 3, p. 034 042, 2016. DOI: 10.1103/PhysRevD.94.034042. arXiv: 1607.01711 [hep-ph].

[105] E. Iancu, A. H. Mueller, and S. Munier, "Universal behavior of QCD amplitudes at high energy from general tools of statistical physics," *Phys. Lett. B*, vol. 606, pp. 342–350, 2005. DOI: 10.1016/j.physletb.2004.12.009. arXiv: hep-ph/0410018.

[106] E. Iancu and D. N. Triantafyllopoulos, "A Langevin equation for high energy evolution with pomeron loops," *Nucl. Phys. A*, vol. 756, pp. 419–467, 2005. DOI: 10.1016/j.nuclphysa.2005.03.124. arXiv: hep-ph/0411405.

[107] E. Iancu and D. N. Triantafyllopoulos, "Non-linear QCD evolution with improved triple-pomeron vertices," *Phys. Lett. B*, vol. 610, pp. 253–261, 2005. DOI: 10.1016/j.physletb.2005.02.015. arXiv: hep-ph/0501193.

[108] Y. Hatta, E. Iancu, C. Marquet, G. Soyez, and D. N. Triantafyllopoulos, "Diffusive scaling and the high-energy limit of deep inelastic scattering in QCD at large N(c)," *Nucl. Phys. A*, vol. 773, pp. 95–155, 2006. DOI: 10.1016/j.nuclphysa.2006.04.003. arXiv: hep-ph/0601150.

[109] E. Iancu, K. Itakura, and L. McLerran, "A Gaussian effective theory for gluon saturation," *Nucl. Phys. A*, vol. 724, pp. 181–222, 2003. DOI: 10.1016/S0375-9474(03)01477-5. arXiv: hep-ph/0212123.

[110] E. Iancu and Y. Mulian, "Forward trijet production in proton–nucleus collisions," *Nucl. Phys. A*, vol. 985, pp. 66–127, 2019. DOI: 10.1016/j.nuclphysa.2019.02.003. arXiv: 1809.05526 [hep-ph].

[111] F. Dominguez, C. Marquet, and B. Wu, "On multiple scatterings of mesons in hot and cold QCD matter," *Nucl. Phys. A*, vol. 823, pp. 99–119, 2009. DOI: 10.1016/j.nuclphysa.2009.03.008. arXiv: 0812.3878 [nucl-th].

[112] A. Dumitru, J. Jalilian-Marian, T. Lappi, B. Schenke, and R. Venugopalan, "Renormalization group evolution of multi-gluon correlators in high energy QCD," *Phys. Lett. B*, vol. 706, pp. 219–224, 2011. DOI: 10.1016/j.physletb.2011.11.002. arXiv: 1108.4764 [hep-ph].

[113] F. Dominguez, C. Marquet, B.-W. Xiao, and F. Yuan, "Universality of Unintegrated Gluon Distributions at small x," *Phys. Rev. D*, vol. 83, p. 105 005, 2011. DOI: 10.1103/PhysRevD.83.105005. arXiv: 1101.0715 [hep-ph].

[114] E. Iancu, K. Itakura, and L. McLerran, "Geometric scaling above the saturation scale," *Nucl. Phys. A*, vol. 708, pp. 327–352, 2002. DOI: 10.1016/S0375-9474(02)01010-2. arXiv: hep-ph/0203137.

[115] A. H. Mueller and D. N. Triantafyllopoulos, "The Energy dependence of the saturation momentum," *Nucl. Phys. B*, vol. 640, pp. 331–350, 2002. DOI: 10.1016/S0550-3213(02)00581-3. arXiv: hep-ph/0205167.

[116] S. Munier and R. B. Peschanski, "Geometric scaling as traveling waves," *Phys. Rev. Lett.*, vol. 91, p. 232 001, 2003. DOI: 10.1103/PhysRevLett.91.232001. arXiv: hep-ph/0309177.

[117] I. Balitsky, "Quark contribution to the small-x evolution of color dipole," *Phys. Rev. D*, vol. 75, p. 014 001, 2007. DOI: 10.1103/PhysRevD.75.014001. arXiv: hep-ph/0609105.

[118] Y. V. Kovchegov and H. Weigert, "Triumvirate of Running Couplings in Small-x Evolution," *Nucl. Phys. A*, vol. 784, pp. 188–226, 2007. DOI: 10.1016/j.nuclphysa.2006.10.075. arXiv: hep-ph/0609090.

[119] G. Beuf, "Improving the kinematics for low-x QCD evolution equations in coordinate space," *Phys. Rev. D*, vol. 89, no. 7, p. 074 039, 2014. DOI: 10.1103/PhysRevD.89.074039. arXiv: 1401.0313 [hep-ph].

[120] E. Iancu, J. D. Madrigal, A. H. Mueller, G. Soyez, and D. N. Triantafyllopoulos, "Resumming double logarithms in the QCD evolution of color dipoles," *Phys. Lett. B*, vol. 744, pp. 293–302, 2015. DOI: 10.1016/j.physletb.2015.03.068. arXiv: 1502.05642 [hep-ph].

[121] A. Dumitru and V. Skokov, "$cos(4\phi)$ azimuthal anisotropy in small-x DIS dijet production beyond the leading power TMD limit," *Phys. Rev. D*, vol. 94, no. 1, p. 014 030, 2016. DOI: 10.1103/PhysRevD.94.014030. arXiv: 1605.02739 [hep-ph].

[122] T. Altinoluk, R. Boussarie, and P. Kotko, "Interplay of the CGC and TMD frameworks to all orders in kinematic twist," *JHEP*, vol. 05, p. 156, 2019. DOI: 10.1007/JHEP05(2019)156. arXiv: 1901.01175 [hep-ph].

[123] T. Altinoluk and R. Boussarie, "Low x physics as an infinite twist (G)TMD framework: unravelling the origins of saturation," *JHEP*, vol. 10, p. 208, 2019. DOI: 10.1007/JHEP10(2019)208. arXiv: 1902.07930 [hep-ph].

[124] H. Fujii, C. Marquet, and K. Watanabe, "Comparison of improved TMD and CGC frameworks in forward quark dijet production," *JHEP*, vol. 12, p. 181, 2020. DOI: 10.1007/JHEP12(2020)181. arXiv: 2006.16279 [hep-ph].

[125] G. Beuf, "Dipole factorization for DIS at NLO: Combining the $q\bar{q}$ and $q\bar{q}g$ contributions," *Phys. Rev. D*, vol. 96, no. 7, p. 074 033, 2017. DOI: 10.1103/PhysRevD.96.074033. arXiv: 1708.06557 [hep-ph].

[126] G. Beuf, "NLO corrections for the dipole factorization of DIS structure functions at low x," *Phys. Rev. D*, vol. 85, p. 034 039, 2012. DOI: 10.1103/PhysRevD.85.034039. arXiv: 1112.4501 [hep-ph].

[127] P. J. Mulders and J. Rodrigues, "Transverse momentum dependence in gluon distribution and fragmentation functions," *Phys. Rev. D*, vol. 63, p. 094 021, 2001. DOI: 10.1103/PhysRevD.63.094021. arXiv: hep-ph/0009343.

[128] E. Iancu and D. N. Triantafyllopoulos, "Higher-point correlations from the JIMWLK evolution," *JHEP*, vol. 11, p. 105, 2011. DOI: 10.1007/JHEP11(2011)105. arXiv: 1109.0302 [hep-ph].

[129] E. Iancu and D. N. Triantafyllopoulos, "JIMWLK evolution in the Gaussian approximation," *JHEP*, vol. 04, p. 025, 2012. DOI: 10.1007/JHEP04(2012)025. arXiv: 1112.1104 [hep-ph].

[130] M. Alvioli, G. Soyez, and D. N. Triantafyllopoulos, "Testing the Gaussian Approximation to the JIMWLK Equation," *Phys. Rev. D*, vol. 87, no. 1, p. 014 016, 2013. DOI: 10.1103/PhysRevD.87.014016. arXiv: 1212.1656 [hep-ph].

[131] Y. V. Kovchegov and D. E. Wertepny, "Long-Range Rapidity Correlations in Heavy-Light Ion Collisions," *Nucl. Phys. A*, vol. 906, pp. 50–83, 2013. DOI: 10.1016/j.nuclphysa.2013.03.006. arXiv: 1212.1195 [hep-ph].

[132] E. Iancu, K. Itakura, and D. N. Triantafyllopoulos, "Cronin effect and high p-perpendicular suppression in the nuclear gluon distribution at small x," *Nucl. Phys. A*, vol. 742, pp. 182–252, 2004. DOI: 10.1016/j.nuclphysa.2004.06.033. arXiv: hep-ph/0403103.

List of Figures